Design of an Aerodynamic Attitude Control System for a CubeSat

by

Jacoba Auret

Thesis presented in partial fulfilment of the requirements for the degree of Master of Science in Engineering at Stellenbosch University

Department of Electrical and Electronic Engineering
University of Stellenbosch
Private Bag X1, 7602, Matieland, South Africa.

Supervisor: Prof. W.H. Steyn

March 2012

Declaration

By submitting this thesis electronically, I declare that the entirety of the work contained therein is my own, original work, that I am the sole author thereof (save to the extent explicitly otherwise stated), that reproduction and publication thereof by Stellenbosch University will not infringe any third party rights and that I have not previously in its entirety or in part submitted it for obtaining any qualification.

Date: March 2012

Summary

The Cape Peninsula University of Technology, in collaboration with Stellenbosch University, is developing a 3-unit CubeSat for a low earth polar orbit. The two main payloads are a camera and a radio frequency beacon. This beacon will be used to calibrate the radar antenna patterns of an antenna of the Hermanus Magnetic Observatory at their base in Antarctica. This thesis describes the development of an aerodynamic attitude determination and control system needed to achieve three-axis stabilisation of the satellite and to perform accurate pointing of the camera.

The satellite structure is designed to utilise aerodynamic means of control. It includes four feather antennae for passive pitch-yaw stabilisation and two active aerodynamic roll control paddles. The sensors used are a three-axis magnetometer, fine sun sensor and nadir sensor. Three attitude determination methods are investigated, namely the Triad, Rate Kalman Filter and Extended Kalman Filter algorithm. Apart from the aerodynamic control elements of the satellite, three magnetic torque rods and three nano-reaction wheels are also included in the design. Three control modes for the satellite are identified and various control methods are investigated for these control modes.

The various attitude determination and control methods are evaluated through simulations and the results are compared to determine the final methods to be used by the satellite. The magnetic Rate Kalman Filter is chosen as attitude determination method to be used when the satellite is tumbling and a combination of the sun Rate Kalman Filter and the Triad algorithm is to be used when the satellite experiences low angular rates. The B-dot and Y-spin controller is chosen for the detumbling control mode, the aerodynamic and cross-product control method for the three-axis stabilisation control mode and the quaternion feedback control method for the pointing control mode of the satellite. The combination of magnetic and aerodynamic control proved to be sufficient for the initial stabilisation of the satellite, but the three nano-reaction wheels are required for the pointing control of the imaging process.

Opsomming

Die Kaapse Skiereiland Universiteit van Tegnologie, in samewerking met die Universiteit van Stellenbosch, is tans besig met die ontwikkeling van 'n 3-eenheid *CubeSat* vir 'n polêre, lae aard-wentelbaan. Die twee loonvragte van die satelliet bestaan uit 'n kamera en 'n radiofrekwensie-baken. Die radiofrekwensie-baken sal gebruik word om 'n antenna van die Hermanus Magnetiese Observatorium, by hul basis in Antarktika, se radar antenna patrone te kalibreer. Hierdie tesis beskryf die ontwikkeling van 'n aerodinamiese oriëntasiebepaling en -beheerstelsel wat benodig word om die satelliet in drie asse te stabiliseer en om die kamera noukeurig te rig.

Die satelliet se struktuur word ontwerp vir aerodinamiese beheer. Dit sluit vier veerantennas in vir passiewe duik-gier beheer, asook twee aerodynamiese rolbeheer flappies vir aktiewe beheer. Die sensors wat gebruik word sluit 'n drie-as magnetometer, fyn sonsensor en nadirsensor in. Drie oriëntasiebepalingsmetodes word ondersoek, naamlik die Drietal, Tempo Kalmanfilter en die Uitgebreide Kalmanfilter algoritmes. Buiten die aerodinamiese beheerelemente van die satelliet, word daar ook drie magneetstange en drie nano-reaksiewiele ingesluit in die ontwerp. Daar word onderskeid getref tussen drie beheermodusse en verskeie beheermetodes word ondersoek vir hierdie beheermodusse.

Die verskeie oriëntasiebepalings- en oriëntasiebeheermetodes word geëvalueer deur middel van simulasies en die resultate word vergelyk om die beste metodes vir die satelliet se gebruik te bepaal. Die magnetiese Tempo Kalmanfilter word gekies as oriëntasiebepalingsmetode vir 'n tuimelende satelliet en die kombinasie van die son Tempo Kalmanfilter en Drietal algoritme word gebruik vir 'n satelliet met lae hoektempos. Die B-dot en Y-spin beheerder word gekies vir die tuimelbeheermodus, die aerodinamiese en kruisproduk beheermetode vir die drie-as-stabilisasie-beheermodus en die kwaternioon terugvoer beheermetode vir die rigbeheermodus van die satelliet. Daar word bepaal dat die samespanning van magnetiese en aerodinamiese beheer voldoende is vir die aanvanklike stabilisering van die satelliet, maar dat die drie nano-reaksiewiele benodig word om die kamera te rig tydens die beeldvormingproses.

Acknowledgements

I would like to extend my gratitude to the following persons and institutes:

My supervisor, Prof. W.H. Steyn, for his guidance and for providing me the opportunity of continuing my studies in this exciting field.

The National Research Foundation for providing me with financial support for my second year of study.

The Cape Peninsula University of Technology for including Stellenbosch University in this project and for providing funds for students to work on this project.

My parents and husband for their support, love and encouragement.

My fellow students and engineers in the Electronic Systems Laboratory for two years of friendship, help and encouragement.

The Lord God, for always walking with me, for surrounding me with people that conveys his love to me and providing me with the strength to accomplish this goal.

Contents

List of Figures

List of Tables

Nomenclature

1U	1-Unit
ADCS	Attitude Determination and Control System
AIS	Automatic Identification System
AMR	Anisotropic MagnetoResistive
Cal Poly	California Polytechnic State University
COM	Centre Of Mass
COP	Centre Of Pressure
DCM	Direction Cosine Matrix
ECI	Earth Centred Inertial
EKF	Extended Kalman Filter
ELF	Extremely Low Frequency
FOV	Field Of View
HIL	Hardware-In-the-Loop
HMO	Hermanus Magnetic Observatory
IGRF	International Geomagnetic Reference Field
MOEMS	Micro-Opto-Electro-Mechanical System
MT	Magnetic Torque rod
NORAD	North American Aerospace Defence Command
OBC	On-Board Computer
ORC	Orbit Referenced Coordinate

PAMS	Passive Aerodynamically stabilised Magnetically-damped Satellite
PC	Personal Computer
PD	Proportional-Derivative
PID	Proportional-Integral-Derivative
P-POD	Poly Pico-satellite Orbital Deployer
PSLV	Polar Satellite Launch Vehicle
QF	Quaternion Feedback
QUEST	QUaternion ESTimator
RF	Radio Frequency
RKF	Rate Kalman Filter
RMSE	Root-Mean-Square attitude Error
RMSP	Root-Mean-Square Pointing error
RMS	Root-Mean-Square
RPY	Roll Pitch Yaw
SBC	Satellite Body Coordinate
S/E	Sun/Eclipse
SFL	Space Flight Laboratory
SGP4	Simplified General Perturbations No.4
SSDL	Space Systems Development Laboratory
TLE	Two Line Elements
TRC	Transit Reference Coordinate
UHF	Ultra High Frequency
UTIAS	University of Toronto Institute for Aerospace Studies
XProd	Aerodynamic and Cross-product

Chapter 1

Introduction

1.1 Background

The Hermanus Magnetic Observatory (HMO) was searching for a low cost method to calibrate the radar antenna patterns of an antenna at their base in Antarctica. It was determined that a small satellite in a low earth polar orbit would be sufficient for this assignment and the use of the CubeSat standard can reduce the cost of such a mission. The Cape Peninsula University of Technology in collaboration with Stellenbosch University are in the process of developing the satellite.

The antenna calibration will require only a few satellite passes and the calibration payload will therefore only be used during a short period of the satellite's life time. A camera is included in the design of the satellite as a secondary long term payload for academic purposes. The calibration of the radar antenna patterns by means of the radio frequency (RF) beacon requires that the satellite be three-axis stabilised within a $\pm 5^\circ$ error margin. This initial requirement was supplied by the Cape Peninsula University of Technology. The normal orientation of the satellite will be with the boresight of both the RF beacon and the camera being nadir pointing. The imaging payload requires a pointing accuracy of 1° root-mean-square (RMS).

Stellenbosch University is responsible for the development of the attitude determination and control system (ADCS). The ADCS has a volume restriction of one $10\,\text{cm} \times 10\,\text{cm} \times 10\,\text{cm}$ cube, must weigh less than 1 kg and has an average power constraint of 2 W. It was decided to design the structure of the satellite to suit aerodynamic means of control, therefore utilising the aerodynamic disturbance torque as a control torque.

1.2 Study Objectives

The aim of this project is the design of a suitable aerodynamic attitude control system for this CubeSat, keeping in mind the restrictions in terms of mass, power and volume. The study objectives are presented below:

- Investigate previous CubeSat missions and their attitude determination and control systems.
- Investigate aerodynamic control of satellites.
- Design a suitable aerodynamic structure for satellite.
- Define control modes of satellite.
- Investigate, simulate and evaluate possible determination and control configurations.
- Produce the final ADCS design.
- Comment on possible improvements.

1.3 Literature review

1.3.1 History of CubeSats

In 1999 Prof. Jordi Puig-Suari at California Polytechnic State University (Cal Poly) and Prof. Bob Twiggs at Stanford University's Space Systems Development Laboratory (SSDL) started the CubeSat Program [14]. The CubeSat design consists of a standardised 10 cm×10 cm×10 cm cube, also referred to as 1-unit (1U) CubeSat. It has a mass restriction of 1.33 kg and must contain all the required subsystems for a specific space mission. These 1U CubeSats can be combined to form larger satellites. Some known variations are the 2U and the 3U CubeSat with the dimensions 20 cm×10 cm×10 cm and 30 cm×10 cm×10 cm, respectively.

As part of the CubeSat Program a standard deployment mechanism, the Poly Picosatellite Orbital Deployer (P-POD), was developed [15]. The aim of the P-POD is to protect the primary payload and launch vehicle, to protect the CubeSats and to provide a simple yet reliable deployment system for CubeSats. It consists of a long aluminium box with a spring for ejection, a door that prevents ejection and a mechanism to open the door. Figure 1.1 shows the structure of a P-POD. One P-POD accommodates any configuration of three single CubeSats. It can therefore deploy three 1U CubeSats, a 1U

Figure 1.1: A P-POD designed by Cal Poly and SSDL [1].

and a 2U CubeSat, or one 3U CubeSat [1]. The P-POD also provides a standard interface to launch vehicles.

The main objective of the CubeSat Program was to make space more accessible for small payloads. This goal can be reached due to the advantages that the use of CubeSats present. CubeSats have lower development, testing and construction costs when compared to larger satellites [14]. The use of the CubeSat standard also yields shorter design and development time-lines due to the standardisation of the structure [16]. An advantage of the P-POD is the standard interface it provides to the launch vehicles that simplifies the integration requirements. One P-POD can also accommodate three 1U CubeSats. If these three cubes take the form of multiple satellites, they are combined in the P-POD as a single payload which leads to lower launch costs [1]. All these qualities present smaller companies and academic institutions the opportunity to build and fund their own satellites for business, research or human development purposes.

The CubeSat, however, limits the designer in terms of volume, weight and available power. The power limit is due to the small surface areas available for solar panels. The challenge of CubeSats therefore lie within the design of the payload and other subsystems to meet the requirements of the standard.

In June 2003 the first six CubeSats were launched by means of the Rockot launch vehicle [15]. Since then the interest in CubeSats has grown and a number of launches have taken place. Some of these CubeSats are discussed here with the focus on the mission of each CubeSat and the ADCS designed to comply with the mission objectives.

1.3.1.1 Compass-1

The Compass-1 satellite is a 10 cm×10 cm×11.35 cm CubeSat developed by Aachen University of Applied Science [2]. This 850 g satellite was launched in April 2008 on-board an Indian Polar Satellite Launch Vehicle (PSLV). The aims of the satellite were to take colour images of Earth with a camera payload, to validate a GPS receiver developed by the German Aerospace Centre and to test a three-axis attitude control system. Figure 1.2 shows the flight model of Compass-1.

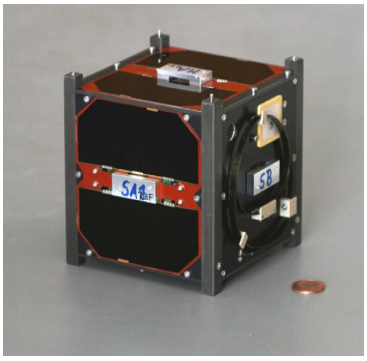

Figure 1.2: Compass-1 satellite [2].

The sensors used by this satellite were a three-axis magnetometer and a set of five micro-opto-electro-mechanical system (MOEMS) sun sensors. The QUEST (QUaternion ESTimator) algorithm was used for attitude determination. Three magnetic coils were used as actuators to achieve the nadir pointing reference orientation. A B-dot controller was used to detumble the satellite and a linear-quadratic regulator constant coefficient controller was used for the pointing of the satellite. The mean nadir pointing error of the controller was determined through simulation as approximately 12° [17].

1.3.1.2 BeeSat-1

The Institute of Aeronautics and Astronautics of the Technical University of Berlin developed the BeeSat-1 satellite that was launched from an Indian PSLV in September 2009 [18]. It was a 1U CubeSat with a mass of 1 kg. The payload of the satellite was a micro-camera that produced images of Earth's surface in the visible range. Another aim of this satellite was to test a micro-wheel system in orbit. In Figure 1.3 the flight configuration of the satellite is shown.

The satellite incorporates six sun sensors, three gyroscopes and two three-axis magnetometers for attitude determination. Three-axis stabilisation is achieved by three micro-wheels and six magnetic coils. The coils are used to desaturate the reaction wheels and for control in periods when the reaction wheels are not active. The four control modes tested

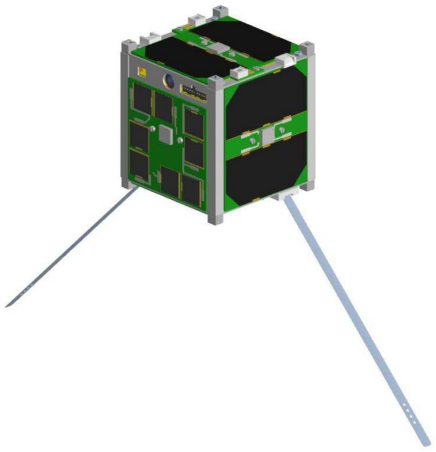

Figure 1.3: BeeSat-1 flight configuration [3].

are inertial pointing, pointing towards the sun for maximum power, nadir pointing and rotation of the satellite.

1.3.1.3 CanX-2

In April 2008, the CanX-2 satellite of the Space Flight Laboratory (SFL) at the University of Toronto Institute for Aerospace Studies (UTIAS) was launched aboard an Indian PSLV [4]. The CanX-2 is a 3U CubeSat with a mass of 3 kg. The satellite was used to test and demonstrate scientific and engineering payloads. The scientific payloads included a miniature atmospheric spectrometer, a GPS atmospheric occultation experiment, a surface material experiment and a dynamic spacecraft networking protocol experiment. Some of the engineering payloads included hardware for accurate GPS determination of relative satellite positions, a nano-propulsion system and an accurate attitude determination system.

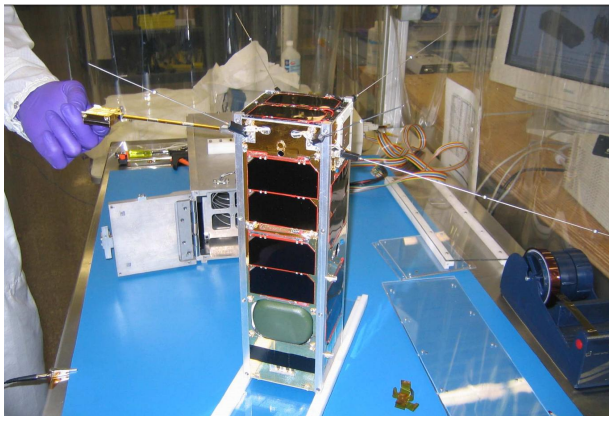

Figure 1.4: The integrated CanX-2 spacecraft [4].

The CanX-2 used six high precision sun sensors, six coarse sun sensors and one three-

axis magnetometer as sensors. The coarse sun sensors were used to determine which of the fine sun sensors must be sampled. An Extended Kalman Filter was used as attitude determination method and an accuracy of $\pm 1^\circ$ was achieved when the satellite was in the sunlit part of its orbit. The actuators of the satellite consisted of one nano-reaction wheel and three magnetic coils. Three-axis stabilisation within an accuracy of $\pm 10^\circ$ was achieved using a Y-Thompson configuration with a momentum bias in a wheel instead of the body of the satellite.

1.3.1.4 QuakeSat

The QuakeSat satellite was a 3U CubeSat launched in June 2003 by means of the Rockot launch vehicle [15]. It was developed by the QuakeFinder Team of Palo Alto and SSDL [19]. Its aim was to detect, record and downlink extremely low frequency (ELF) magnetic signal data that may be used to predict earthquakes. The payload was a 30 cm ELF magnetometer that was extended from the main satellite bus on a deployable boom as shown in Figure 1.5. This boom must be aligned with the magnetic field line of Earth.

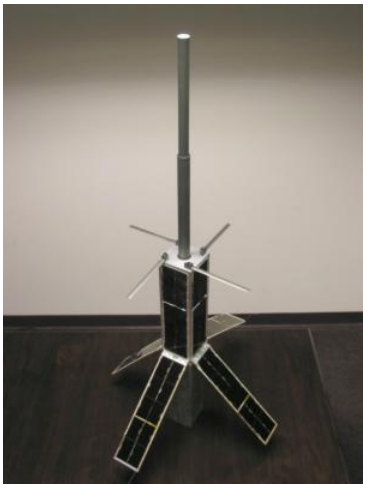

Figure 1.5: Deployed configuration of the QuakeSat satellite [5].

Passive attitude control with four permanent magnets was used to align the magnetometer payload boom with Earth's magnetic field. Libration damping was incorporated by means of two hysteresis rods for when the satellite tumbles over the poles. This control method was, however, not sufficient to overcome the gravity gradient torque on the satellite [5]. It was determined, using the satellite's infra red sensor, that the true attitude profile of the satellite might have been with the payload boom generally pointing towards nadir. The solar panel current measurements were used to form a crude determination of the attitude of the satellite. Unfortunately, these solar panel currents were lost early in the satellite's

lifetime and the other sensor information that was still available were insufficient for the task.

1.3.1.5 NCube-2

The Norwegian University of Science and Technology, Narvik University College, University of Oslo and the Agricultural University of Norway joined forces to produce the NCube-2 [6]. This satellite is a 1U CubeSat that weighs 1 kg and was launched in October 2005 aboard a Cosmos 3M launch vehicle. Its aim was to demonstrate ship tracking from space using the maritime Automatic Identification System (AIS) and to use AIS for the tracking of reindeer herds.

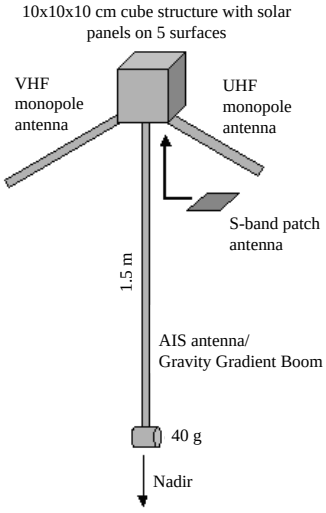

Figure 1.6: Deployed configuration of the NCube-2 satellite [6].

The satellite had a gravity gradient boom and three magnetic coils to achieve three-axis stabilisation with the boom pointing towards nadir, as shown in Figure 1.6. An analysis of solar cell lighting conditions was used to determine the sun's position with respect to the satellite. This position, together with the reading of a three-axis magnetometer, was to be used in an Extended Kalman Filter to determine the satellite's attitude. Unfortunately, this NCube-2 satellite did not respond to communications after deployment and it was assumed that the satellite had malfunctioned.

1.3.2 Aerodynamic Satellites

In 1995 the possibility of using aerodynamic torques to stabilise satellites in low earth orbits was investigated by Renjith Kumar, Daniel Mazanek and Michael Heck [7]. Their goal was to design a totally passive stabilised spacecraft [8]. The satellite used passive

aerodynamic torques for stabilisation and magnetic hysteresis rods for passive means of damping. The satellite was named the Passive Aerodynamically Stabilised Magnetically-damped Satellite (PAMS) [9].

The structure of the satellite resembled that of a long stove pipe as shown in Figure 1.7. It consisted of two shells: a high density shell was located at the front of the satellite with a low density shell at the back of the satellite. This chosen structure shifts the centre of mass (COM) closer to the front of the satellite and causes an offset between the COM and the aerodynamic centre of pressure (COP). During flight, this misalignment of the COM and the COP will result in aerodynamic restoring torques about the pitch and yaw axes of the satellite when its long symmetry axis is not aligned with the local atmospheric vector.

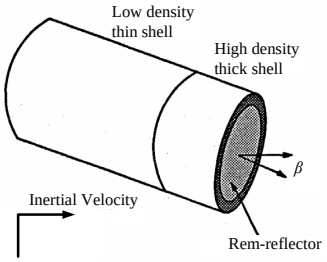

Figure 1.7: Illustration of PAMS [7].

The simulations used for analysis were based on free-molecular-flow aerodynamics [7]. It incorporated variations in the atmospheric density, the effect of horizontal global winds and the effect of solar radiation pressure. An eighth order Earth magnetic field model was used to include the effect of magnetic hysteresis rods. The orbit was assumed to be circular with an altitude between 250 km and 325 km.

The design was tested in May 1996 when the PAMS satellite was deployed from the space shuttle Endeavour at a tumbling rate of more than 2 degrees per second [8]. The performance of the satellite was monitored by means of video recordings. The satellite was stabilised about the pitch and yaw axis after several days of operation.

The design of PAMS resulted in a aerodynamic pitch-yaw stabilised spacecraft, but with no control over the roll axis of the spacecraft. This shortcoming was addressed by Mark Psiaki in 2004 [8]. Psiaki presented a design for a three-axis stabilised, nadir pointing nano-satellite that complies with the constraints of a 1U CubeSat. This design combines the pitch-yaw system of PAMS with active magnetic control from magnetic torque coils.

The design is based on the structure of a badminton shuttlecock and a four feathered version is shown in Figure 1.8. The satellite consists of a 10 cm×10 cm×10 cm cube with

four aerodynamic drag feathers protruding from the back of the main bus. These feathers move the aerodynamic COP behind the COM and relies on the differential drag on the feathers for stabilisation. It therefore results in a similar pitch-yaw stabilisation system to that of PAMS. The difference between the two designs is the damping of the satellite. Psiaki used an active magnetic feedback control system to damp the aerodynamic pitch-yaw system and used it to stabilise the roll of the satellite.

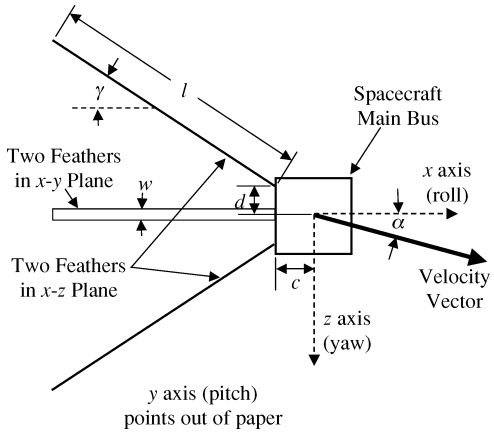

Figure 1.8: Geometric model of the aerodynamic pitch-yaw stabilised spacecraft [8].

The simulations were based on free-molecular aerodynamics. It used Euler's dynamic equation and quaternion kinematics to model the closed-loop dynamics of the spacecraft. The torques included in the dynamic equation were the aerodynamic torque, magnetic control torque, gravity gradient torque, torque due to solar radiation pressure as well as radiation pressure from Earth's albedo. The atmospheric model assumed that the atmosphere rotates with Earth that cause yaw disturbances on satellites in inclined orbits. The model did not model atmospheric winds. The magnetometer errors were included in the simulation for they affect the system through the magnetic feedback law.

Simulation results were supplied for a typical case, as well as a challenging worst-case. For both cases a three, rather than four, feathered system was considered. The typical case included zero collective twist on the feathers and a COM imbalance. The simulation orbit was a 400 km circular equatorial orbit. The satellite had initial roll, pitch and yaw body rates of -3, -2 and 2.5 degrees per second, respectively. After one hour the satellite stopped tumbling and the final pointing accuracy was approximately 2°. The challenging case included collective twist and a COM imbalance. Furthermore, an inclined circular orbit of 87° and an altitude of 457 km was used. The initial tumbling rates were 3, 3.5, -4 degrees per second for the roll, pitch and yaw axes. The tumbling ceased in less than an hour and the steady-state maximum pointing errors were 22° in roll, 13° in pitch and 27° in yaw. The roll errors were mainly due to the aerodynamic twist of the feathers.

Psiaki concluded that three-axis stabilisation can be achieved by the use of the badminton shuttlecock design with active magnetic feedback for orbits up to 500 km. He also noted that the pointing errors will decrease with a decrease in orbital inclination and altitude, mass imbalance, aerodynamic twist of the feathers and magnetometer errors.

In 2007, Gargasz presented three-axis attitude control of the spacecraft design, shown in Figure 1.9, utilising only active aerodynamic control [7]. The main bus of the satellite measured 50 cm×50 cm×50 cm and the mass was assumed to be 10 kg. The satellite had four movable aerodynamic panels at the back of the satellite with the dimensions 25 cm×40 cm and was based on the badminton shuttlecock design of Psiaki. By controlling the panel angles, the desired control torque could be generated by means of aerodynamic torques. Partial accommodation theory was used in the analysis and it was also assumed that the atmosphere rotates with Earth. Gargasz used simulations to evaluate the performance of the controller. The orbital altitude used in these simulations was 300 km. The results showed that the satellite could be three-axis stabilised from a range of initial orientations and angular body rates.

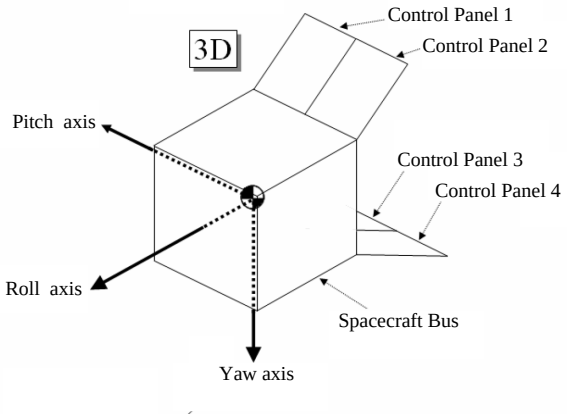

Figure 1.9: Spacecraft model presented by Gargasz [7].

The authors of [9] presented a passive aerodynamic attitude control system for a pico-satellite design concept in 2008. The satellite consisted of a 3U CubeSat with deployable drag fins resembling Psiaki's design and is shown in Figure 1.10. The satellite was designed to stay aligned with the atmospheric velocity vector. The simulations used a Direct Simulation Monte Carlo method to model the atmosphere and its interaction with the satellite, including the effect of shadowing. The simulations concentrated on the control of the pitch angle of the satellite. The damping of the angular rates were assumed and active magnetic torquing or hysteresis dampers were proposed as possible elements to generate this damping. It was determined that a panel deployment angle of approximately 50° to

the roll axis is most efficient. The satellite was stabilised for altitudes below 450 km and worst-case pointing errors of 2.5° were achieved at an altitude of 400 km.

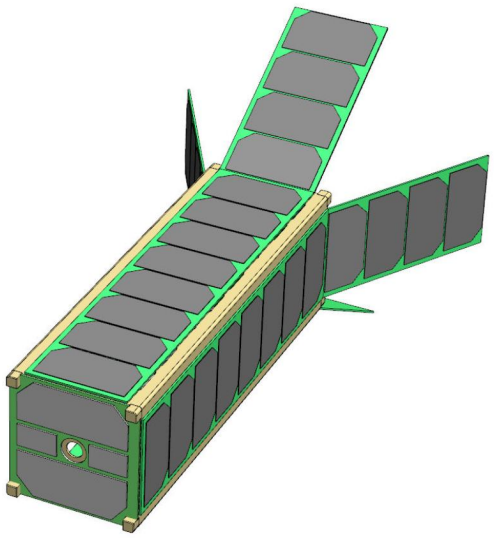

Figure 1.10: Spacecraft design model of [9].

1.4 Thesis Overview

The theoretical background of the project is presented in Chapter 2. The three coordinate frames used to describe the orientation and position of the satellite are defined, as well as the transformation matrices needed for vector transformation between the various coordinate frames. The satellite structure is designed for the use of aerodynamic control and the sensors and actuators for the project are chosen. The orientation of the satellite is defined by the Euler kinematic and dynamic equations and the disturbance torques that affect the orientation of the satellite are discussed.

All the possible determination and control methods are evaluated through simulation. In Chapter 3 the elements of the simulation orbit are described. The simulation environment is set up in *Matlab* and the various subsystems are discussed in terms of their purpose, the required inputs and the resulting outputs.

In Chapter 4 various attitude determination methods are discussed and evaluated. The Triad algorithm determines the orientation of the satellite using two measured and modelled vector pairs. Two variations of the Rate Kalman Filter (RKF) are discussed. The sun RKF is used to produce an estimated inertially referenced body rate vector while the magnetic RKF produces an orbit referenced body rate vector. The Extended Kalman

Filter can be used to determine the full state vector of the satellite, i.e. the inertially referenced body rate vector and the satellite orientation in quaternions. The determination methods are evaluated for a tumbling and stabilised simulation set and compared to one another.

The control methods considered for this project are discussed in Chapter 5. The satellite requires three control modes during the course of its lifetime. For the detumbling mode only a single detumbling controller is considered. Two aerodynamic control methods are considered for the three-axis stabilisation mode of the satellite and three reaction wheel control methods are investigated for the pointing control mode. The methods for each control mode are evaluated and compared in order to determine the best methods to be included in the final design. A hardware-in-the-loop test of the on-board computer designed by Botma [13] for this satellite project is also performed. Chapter 6 concludes this thesis with a summary of the project findings and some recommendations.

Chapter 2

Theoretical Background

Before one starts with the control of a satellite there are certain aspects that need to be considered. These include the coordinate frames in which the position and attitude of the satellite can be described, the structure and content of the satellite, the equations of motion and the various external disturbance torques that influence them.

Three coordinate frames are discussed in this chapter. The satellite body coordinate (SBC) frame is linked to the physical satellite body while the orbit referenced coordinate (ORC) frame relates to the orbital path. The earth centred inertial (ECI) coordinate frame is the third coordinate frame used in this project. The transformation matrices needed to convert a vector from one reference frame to another are also discussed.

The satellite structure is designed to incorporate the two mission payloads that consist of a radio frequency beacon and a camera. A further requirement is that the satellite body must be designed to suit aerodynamic means of control. This design relies greatly upon the aerodynamic pitch-yaw stabilisation system presented by [8] and additional aerodynamic roll control paddles. The description of the satellite's content is limited to the content of the attitude determination and control system.

The rotational motion of the satellite can be described by the Euler kinematic and dynamic equations. The kinematic equation specifies the time-evolution of the attitude parameters of the satellite, while the dynamic equation takes into account the effect of applied torques on the rate of change of the angular velocity vector of the satellite [10]. Some of these applied torques can be controlled torques supplied by the satellite actuators. Others can be disturbance torques produced by aerodynamic drag, the gravity of the Earth or solar radiation. These disturbance torques need to be converted to numerical values in order to include them in the dynamic equation of motion.

2.1 Coordinate Frames and Transformations

The position and attitude of the satellite are described relative to certain reference frames. According to [20] a reference frame is defined by the location of its centre, also referred to as its origin, and the element or direction with respect to which the reference frame is fixed. Three reference frames are used in this project.

The origin of the satellite body coordinate frame is located at the geometrical centre of the main bus of the satellite. This point is also assumed to be the centre of mass of the satellite. The frame is fixed to the satellite body with the X_B-axis defined along the length of the main bus toward the front of the satellite as shown in Figure 2.1. The Z_B-axis is parallel to the rotation axes of the aerodynamic roll paddles and the Y_B-axis completes the orthogonal set. All measurements are made with respect to this coordinate frame.

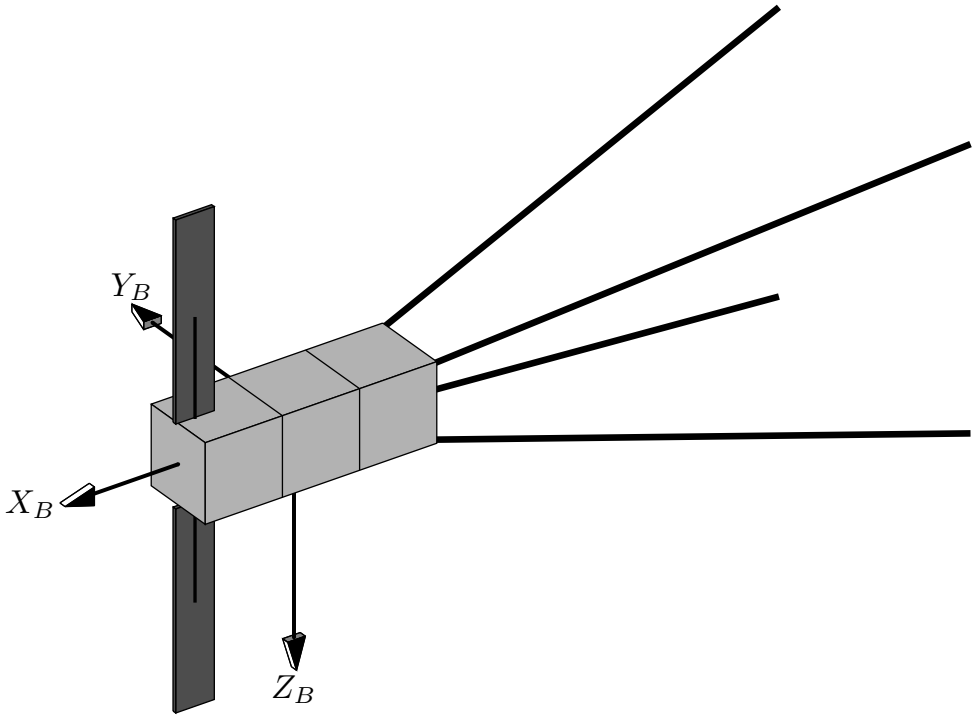

Figure 2.1: Definition of the SBC frame.

The second coordinate frame is the orbit referenced coordinate frame. It is also centred at the COM of the satellite, and therefore moves along the orbit path as the satellite does, but it maintains its orientation with respect to Earth. The Z_O-axis always points towards the centre of Earth, also called the nadir direction. The Y_O-axis points in the orbit anti-normal direction where the orbit normal is defined by the right hand rule. If the thumb of your right hand points in the orbit normal direction, your fingers curl in the direction of travel around the orbit. In Figure 2.2 it is visible that the X_O-axis completes

the orthogonal set. When the satellite is in a circular orbit the X_O-axis always coincides with the velocity vector of the satellite. This, however, is only the case at the apogee and perigee of an elliptical orbit.

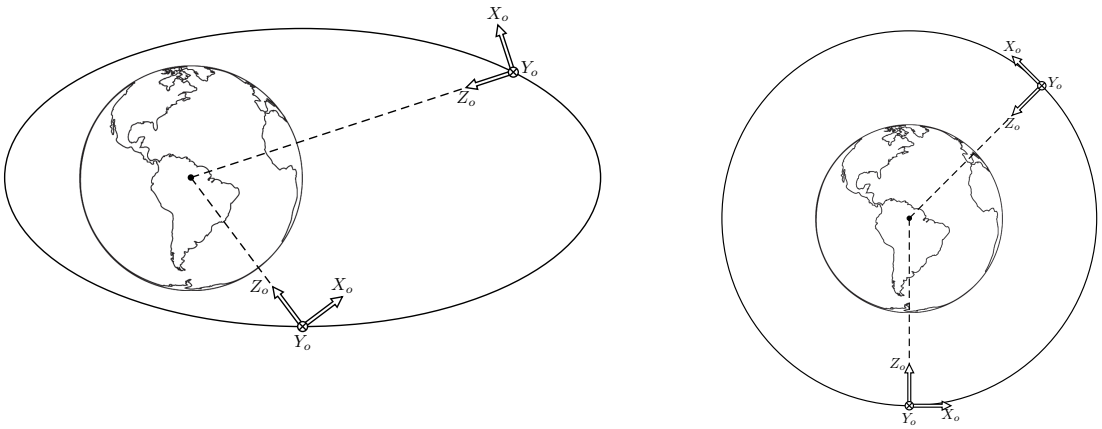

(a) (b)

Figure 2.2: ORC frame illustration with (a) an elliptical and (b) a circular orbit [10].

The attitude of the satellite relative to the ORC frame is described in terms of Euler's three rotation angles, i.e. roll ϕ, pitch θ and yaw ψ. These angles represent three consecutive rotations to change from the ORC frame to the SBC frame. The order in which these angle rotations are performed must be specified. In this project the Euler 213 sequence, illustrated in Figure 2.3, is used. The first rotation is a pitch rotation θ about the Y_O-axis. It is followed by a roll rotation ϕ about the intermediate X'-axis and is concluded with a yaw rotation ψ about the Z_B-axis.

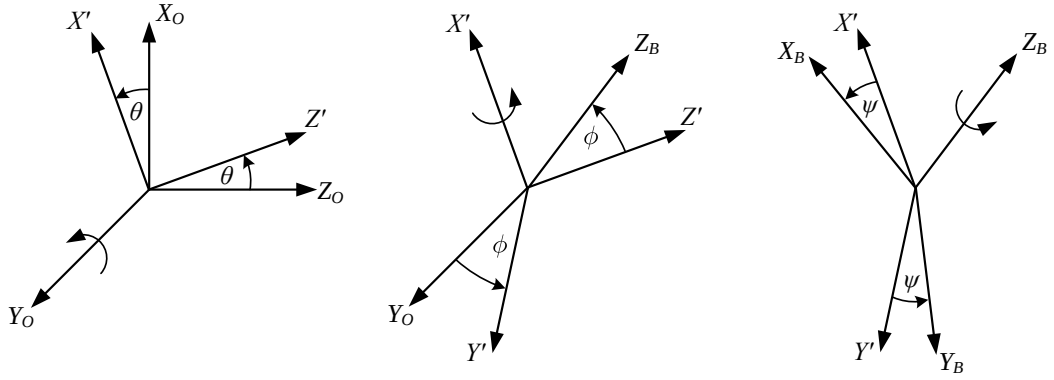

(a) (b) (c)

Figure 2.3: Euler 213 rotation sequence.

The direction cosine matrix $\mathbf{A}$, also referred to as the transformation matrix, can be used to transform a vector in the ORC frame to the SBC frame. For Euler 213 this matrix is given by:

$$\boldsymbol{A}_{O/B} = \begin{bmatrix} (\sin\phi\sin\theta\sin\psi + \cos\theta\cos\psi) & \cos\phi\sin\psi & (\sin\phi\cos\theta\sin\psi - \sin\theta\cos\psi) \\ (\sin\phi\sin\theta\cos\psi - \cos\theta\sin\psi) & \cos\phi\cos\psi & (\sin\phi\cos\theta\cos\psi + \sin\theta\sin\psi) \\ \cos\phi\sin\theta & -\sin\phi & \cos\phi\cos\theta \end{bmatrix} \tag{2.1.1}$$

If the transformation matrix is known, the individual Euler angles can be determined by:

$$\phi = -\arcsin\left(A_{32}\right) \tag{2.1.2}$$

$$\theta = \arctan\left(\frac{A_{31}}{A_{33}}\right) \tag{2.1.3}$$

$$\psi = \arctan\left(\frac{A_{12}}{A_{22}}\right) \tag{2.1.4}$$

where *arctan()* is implemented as a four quadrant function [21].

Interpretation of Euler angles are more intuitive and are therefore used as inputs to simulations and for illustration of simulation outputs. They can, however, cause singularities during numerical computation. The Euler symmetric parameters, also named quaternions, yield no singularities and are therefore used to represent the satellite's attitude during numerical computations [10].

The quaternion consists of four parameters and its definition relies greatly upon Euler's Theorem. This theorem states that the finite rotation of a rigid body with one point fixed can be expressed by a single rotation about some fixed axis [10]. In our application this fixed axis, also named the Euler axis, is represented by a unit vector in the ORC frame. The quaternion can now be defined as:

$$q_1 \triangleq e_1 \sin\left(\frac{\Phi}{2}\right) \tag{2.1.5}$$

$$q_2 \triangleq e_2 \sin\left(\frac{\Phi}{2}\right) \tag{2.1.6}$$

$$q_3 \triangleq e_3 \sin\left(\frac{\Phi}{2}\right) \tag{2.1.7}$$

$$q_4 \triangleq \cos\left(\frac{\Phi}{2}\right) \tag{2.1.8}$$

where e_1, e_2 and e_3 are the X_O-, Y_O- and Z_O-components of the unit Euler axis in the ORC frame and Φ represents the angle that the satellite is rotated about the Euler axis. The quaternion elements are related to one another by the following constraint:

$$q_1^2 + q_2^2 + q_3^2 + q_4^2 = 1 \tag{2.1.9}$$

The quaternion error $\mathbf{q}_e$ is an attitude error value used in the control algorithms of Chapter 5. It is defined by Wie [22] as a function of the commanded quaternion attitude $\mathbf{q}_c$ and the quaternion $\mathbf{q}$ of the current satellite attitude:

$$\begin{bmatrix} q_{1e} \\ q_{2e} \\ q_{3e} \\ q_{4e} \end{bmatrix} = \begin{bmatrix} q_{4c} & q_{3c} & -q_{2c} & -q_{1c} \\ -q_{3c} & q_{4c} & q_{1c} & -q_{2c} \\ q_{2c} & -q_{1c} & q_{4c} & -q_{3c} \\ q_{1c} & q_{2c} & q_{3c} & q_{4c} \end{bmatrix} \begin{bmatrix} q_1 \\ q_2 \\ q_3 \\ q_4 \end{bmatrix} \tag{2.1.10}$$

The transformation matrix $\mathbf{A}_{O/B}$ can be expressed in terms of the quaternion elements and is given by (2.1.11). Comparing this matrix with the Euler angle version in (2.1.4) a relation can be formed between the quaternions and the Euler angles.

$$\mathbf{A}_{O/B} = \begin{bmatrix} q_1^2 - q_2^2 - q_3^2 + q_4^2 & 2\left(q_1 q_2 + q_3 q_4\right) & 2\left(q_1 q_3 - q_2 q_4\right) \\ 2\left(q_1 q_2 - q_3 q_4\right) & -q_1^2 + q_2^2 - q_3^2 + q_4^2 & 2\left(q_2 q_3 + q_1 q_4\right) \\ 2\left(q_1 q_3 + q_2 q_4\right) & 2\left(q_2 q_3 - q_1 q_4\right) & -q_1^2 - q_2^2 + q_3^2 + q_4^2 \end{bmatrix} \tag{2.1.11}$$

The final coordinate frame used in this project is the J2000 earth centred inertial frame. The origin of the ECI frame is at the centre of Earth. The Z_I-axis stretches from the origin to the celestial north pole of Earth while the X_I-axis is aligned with the position of the vernal equinox Υ on 1 January 2000, at noon terrestrial time [23]. The Y_I-axis completes the orthogonal set. The alignment of the axes are shown in Figure 2.4.

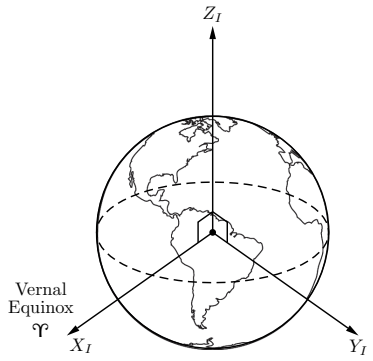

Figure 2.4: Definition of the ECI frame [10].

The models used in this project (see Section 3.2) produce output vectors in the ECI frame. A number of these modelled values are needed as orbit referenced vectors and therefore a transformation matrix from the ECI to ORC frame is needed:

$$\boldsymbol{A}_{I/O} = \begin{bmatrix} \left(\bar{\mathbf{u}}_I \times \left(\bar{\mathbf{v}}_I \times \bar{\mathbf{u}}_I\right)\right)^T \\ \left(\bar{\mathbf{v}}_I \times \bar{\mathbf{u}}_I\right)^T \\ -\bar{\mathbf{u}}_I^T \end{bmatrix} \tag{2.1.12}$$

where $\bar{\mathbf{u}}_I$ is the position unit vector of the satelllite and $\bar{\mathbf{v}}_I$ is the satellite's velocity unit vector, both in ECI coordinates [21].

2.2 Satellite Structure and Content

The satellite is designed to incorporate both the mission payloads while still fitting within the small volume that is inherent to a CubeSat. The external structure of the deployed satellite is mainly influenced by the desire to perform passive and active aerodynamic control on the satellite.

The main bus of the satellite comprises of three 10 cm×10 cm×10 cm cubes, also referred to as a 3U CubeSat. All deployable parts are confined within this 3U before the satellite is ejected from the P-POD. Figure 2.5 shows the model of the deployed satellite and indicates the satellite body coordinate frame. The 1U cube at the front of the satellite is allocated to the satellite's attitude determination and control system and contains the sensors, actuators and the ADCS on-board computer. The various sensors and actuators are discussed in Sections 2.2.2 and 2.2.1. The two 1U cubes at the back of the main bus contain the two payloads and the other subsystems of the satellite.

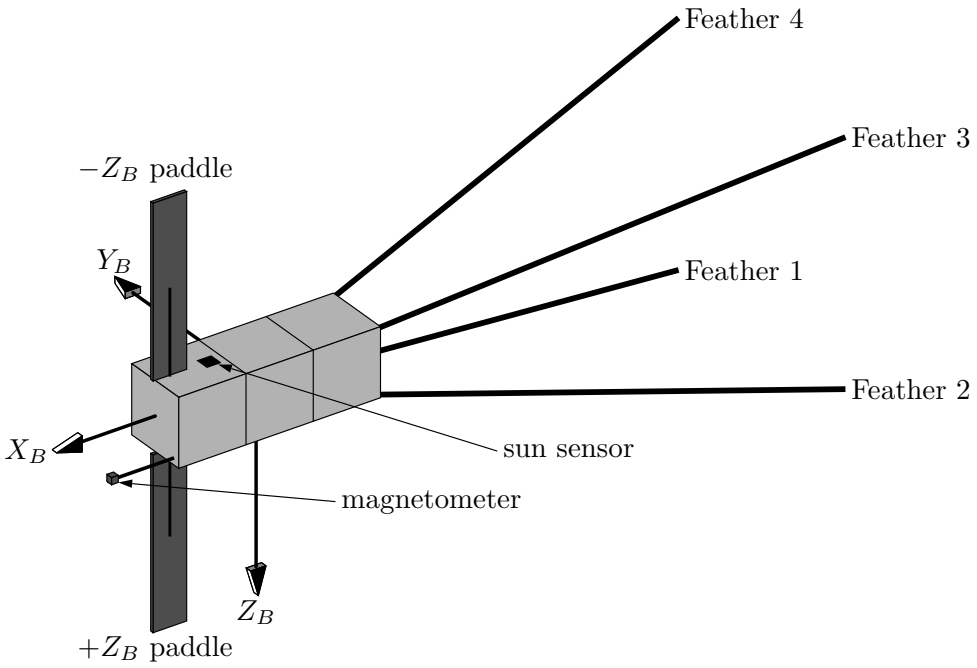

Figure 2.5: Deployed satellite model

The deployable parts of the satellite comprise of four aerodynamic feather antennae, two aerodynamic roll control paddles and the magnetometer on a short arm at the front of the satellite. It is assumed that the centre of mass of the satellite, after all the parts of the satellite has been deployed, coincides with the geometrical centre point of the 3U structure. Since all the final components of the satellite has not yet been determined, it is difficult to determine the true centre of mass. However, it should be possible to locate the centre of mass close to the geometrical centre of the 3U by proper placement of the main

components, like batteries, with large mass and by controlling the layout of the internal cabling harness.

For passive aerodynamic control the simplified pitch-yaw stabilisation system of Psiaki [8] is considered. It consists of four aerodynamic feather antennae, one located on each side of the back panel of the main bus. The design approximates the form of a badminton shuttlecock and aims to locate the centre of drag pressure behind the centre of mass. The design therefore makes use of differential drag on the four feathers to stabilise the pitch and yaw angles of the satellite. If the satellite has a negative pitch angle about the Y_B-axis of the satellite, all the feathers at the back of the satellite will tilt upward. The projected area of the two top feathers (negative z-direction) perpendicular to the airflow will increase. This increase relates to an increase in their drag and the vertical moment arm to the centre of mass. Furthermore, the projected area of the bottom feathers (positive z-direction) perpendicular to the airflow decreases. This reduces their drag and shortens the vertical moment arm. The combination of these effects result in a restoring positive pitch torque. A similar reasoning holds true for rotations about the yaw axis.

This principle of the aerodynamic feathers was included in the satellite model, except that the feathers were moved to the corners of the back panel of the main bus. This design change is made to accommodate larger aerodynamic roll paddles as is explained in Section 2.2.2. The feathers can be made of a thin curved strip of steel or Kevlar, similar to a steel tape measure, as proposed by Psiaki [8]. The aerodynamic feathers also function as ultra high frequency (UHF) and L-band antennae. The design of the feather antennae was done by Lehmensiek [24] and the proposed dimensions are used in this project. The dimensions of each feather is 630 mm$\times$15 mm$\times$1 mm and the angle between each feather and the negative X_B-axis is 17 degrees.

The aerodynamic feather antennas only affect the pitch and yaw angles of the satellite. In order to control the roll angle, two aerodynamic roll control paddles are mounted on the positive and negative Z_B-axis panels of the ADCS 1U. The normal state of the roll paddles is with their largest surface area parallel to the plane in which both the X_B- and Z_B-axis lie. This orientation of the paddles is shown in Figure 2.5. These roll paddles are used as actuators and are further explained in Section 2.2.2.

The total mass of the satellite is 3 kg. For the calculation of the principle moments of inertia a mass of 10 g was allocated to each feather antenna and 20 g to each roll paddle. The mass of the main bus is assumed to be evenly distributed since the final composition, placement and mass of the components are not yet known entities. The mass of the deployed mechanisms are assumed to be point masses at the geometrical centre of the object to simplify the calculations. The approximated moment of inertia tensor, with the

products of inertia assumed to be zero, is given by:

$$\mathbf{I} = \begin{bmatrix} I_{xx} & 0 & 0 \\ 0 & I_{yy} & 0 \\ 0 & 0 & I_{zz} \end{bmatrix} = \begin{bmatrix} 0.0071 & 0 & 0 \\ 0 & 0.035 & 0 \\ 0 & 0 & 0.337 \end{bmatrix} \text{kg.m}^2 \tag{2.2.1}$$

2.2.1 Sensors

In order to determine the attitude and rate of a satellite, sensor measurements are required. In this satellite three sensors are used, namely a three-axis magnetometer, fine sun sensor and a nadir sensor.

The HMC1053 three-axis anisotropic magnetoresistive (AMR) magnetometer from Honeywell is used in this satellite. The magnetometer has a range larger than the required $\pm 60\,\mu$T with a resolution of 12 nT [11]. The magnetometer readings are used during periods when the satellite is tumbling to estimate the angular body rates of the satellite. This determination method is discussed in Section 4.2. To prevent the corruption of the readings by internal magnetic moments of the satellite, the magnetometer is mounted on a short deployable mechanical arm. The arm is located at the front of the satellite and is aligned with the X_B-axis when deployed.

The sun and nadir sensors were developed by Stellenbosch University [12]. These sensors are based on low power CMOS cameras with 190° field of view (FOV). Both the sensors are located in the ADCS cube. The nadir sensor is positioned with its boresight in the positive Z_B-direction while the fine sun sensor is mounted with its boresight in the negative Z_B-direction.

A 0.01% neutral density filter is added to the camera of the sun sensor to prevent it from saturating when determining the sun vector. The nadir sensor does not have a filter, since it only takes images of Earth as it is illuminated by the sun. If the sun is in the nadir sensor's FOV, the camera will saturate and the measurement will be invalid. The boresights of the two sensors are in opposite directions and a rule is therefore formed that prevents the use of nadir measurement if the sun sensor measurement is not valid. This will prevent the use of nadir measurements in eclipse and during periods where the camera is saturated.

The accuracy of the nadir sensor for a full profile of Earth varies between 0.1° and 0.46°. If the boresight of the camera is moved 30° away from the nadir direction, the edge of

Earth moves out of the FOV of the camera and a full profile of Earth is not available any more. The measurement errors increase as the profile of the Earth becomes smaller. To prevent the use of measurements with large errors, a constraint is set to the nadir sensor. If the measured nadir vector falls outside a 120° FOV of the camera, the visible profile of Earth is deemed too small and the measurement is discarded as invalid. The accuracy of the fine sun sensor is better than 0.2° for a FOV of ±30° and less than 2° for a FOV between ±30° and ±90°. Figure 2.6 shows the *CubeSense* module that consists of the sun and nadir sensors.

Figure 2.6: Sun and nadir sensor unit.

2.2.2 Actuators

Once the attitude and rate of the satellite are determined, actuators are needed to control the satellite to the desired orientation. The actuators included in this satellite are two active aerodynamic roll control paddles, three magnetic torque rods and three nano-reaction wheels.

The normal position of the paddles are visible in the deployed satellite model shown in Figure 2.5. During paddle control, the two paddles always turn in opposite directions about the Z_B-axis and thus generate aerodynamic roll torques of the same magnitude and sign. By controlling the angle and the rotation direction of the paddles, the size and the direction of the generated aerodynamic roll torque and consequently the roll angle of the satellite can be controlled.

Figure 2.7 illustrates the functionality of the roll paddles assuming that the atmospheric velocity vector is in the negative X_B-direction, therefore into the page on the figure. When the positive Z_B-axis paddle rotates through a positive 30° angle from its normal position, the airflow causes a reaction force with a positive Y_B-component at the paddle's centre of pressure. The rotated paddle therefore generates a negative torque about the X_B-axis of the satellite. At the same time, the negative Z_B paddle rotates through an angle of -30° from its normal position and experiences a reaction force with a negative Y_B-component

at the paddle's centre of pressure. This also leads to a negative torque about the X_B-axis of the satellite. Both paddles produce a negative roll torque and the satellite starts a negative rotation about its X_B-axis.

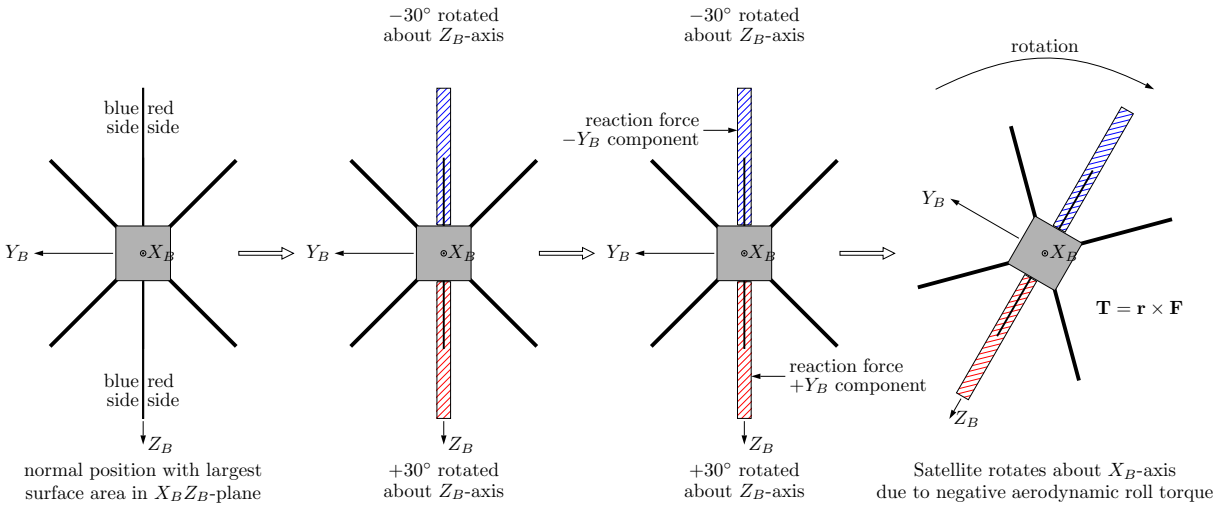

Figure 2.7: The operation of the aerodynamic roll control paddles.

The magnitude of the aerodynamic torque generated by the paddles is related to the surface area perpendicular to the airflow and the length of the moment arm from the COM of the satellite to the COP of the aerodynamic paddle. The calculation of this torque is discussed in more detail in Section 2.4.1. A number of configurations of the control paddles were considered of which only two will be discussed. Simulations were used to compare the various configurations. The total accumulated paddle angle is used as a measure of how active the control paddles are during the simulation. The time it takes the paddles to control the satellite to the desired zero degrees is also considered.

In the first design the aerodynamic feathers are located on the sides of the back panel of the main bus as used by Psiaki [8]. When the paddles are rotated to their maximum angle they are not allowed to shadow the airflow to the feathers. This constraint led to the design of very small paddles (40 mm×2 mm×100 mm), mounted with an offset along the Y_B-axis as shown in Figure 2.8(a). The maximum aerodynamic torque that can be generated by these paddles is approximately 4×10^{-9} Nm, assuming that the X_B-axis is aligned with the X_O-axis of the ORC frame and that the satellite has an altitude of 500 km.

In the second configuration the aerodynamic feathers were moved to the corners of the back panel of the main bus. This move enabled the use of larger paddles without shadowing the feathers. The designed paddle dimensions are 50 mm×2 mm×250 mm and they are mounted in the middle of each side as can be seen in Figure 2.8(b). Using the same as-

sumptions as for the first design, the maximum aerodynamic torque that can be generated by this configuration is approximately 2×10^{-8} Nm.

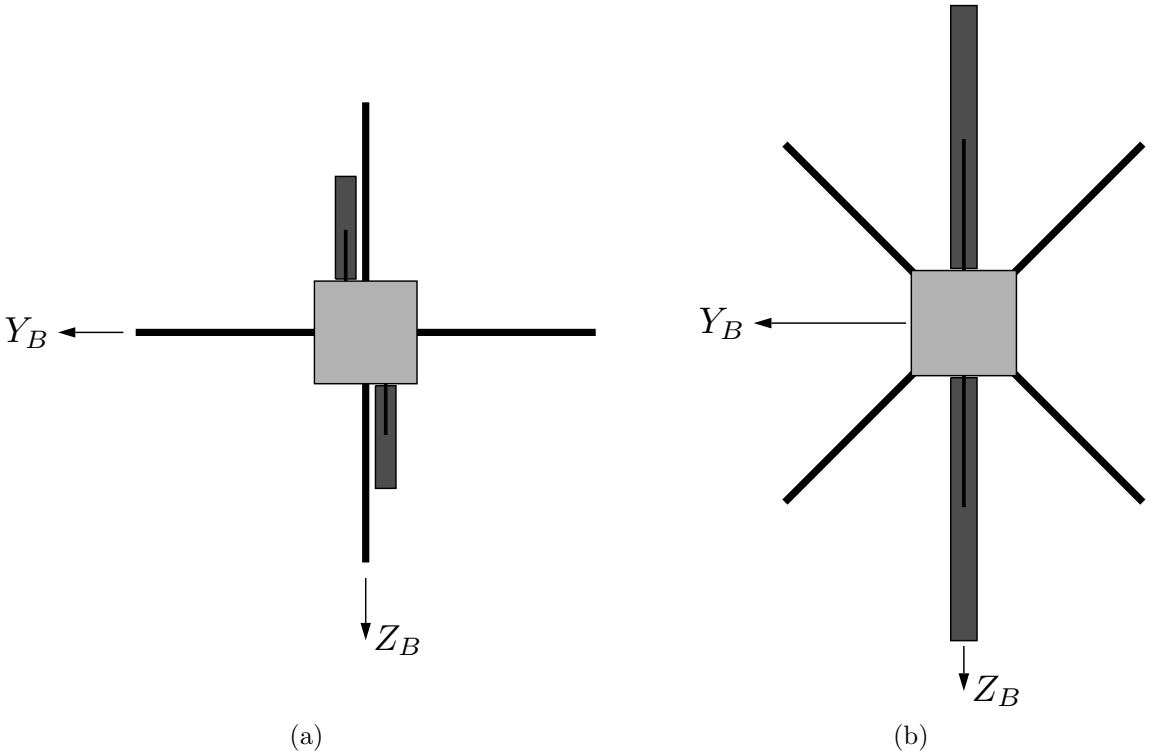

(a) (b)

Figure 2.8: Two paddle configurations: (a) Small paddles at an Y-offset and centred feathers and (b) Large centred paddles with feathers at the corners.

The first configuration required a total accumulated paddle rotation θ_{total} of 602.9 rad to control a roll angle of 20° to the desired zero roll angle within a time of 2 083 seconds. This is 36.7% of an orbit period and thus a shorter settling time is desirable. The larger control paddles of the second configuration resulted in a rise time of 921 seconds using only 238.4 rad of total accumulated paddle rotation. The rise time is 16.2% of the orbit period.

The second configuration resulted in the shortest rise time along with a 60% improvement on the total paddle rotation needed by the first configuration to complete the roll manoeuvre. The decision is made to use the second configuration in this project.

The satellite also makes use of three nano-reaction wheels. These wheels are also located in the ADCS cube and each wheel is aligned with one of the principle body axes. The reaction wheels are mainly used for more accurate control during imaging. The wheel aligned with the Y_B-axis can, however, be used as a momentum wheel to add gyroscopic stiffness against disturbance torques about the X_B- and Z_B-axis of the satellite. The

maximum torque of a reaction wheel is 0.1 mNm and the maximum angular momentum 4 mNms.

The three magnetic torque rods are positioned parallel to the principle body axes in die ADCS cube. The torque rods are used for damping of the passive aerodynamic control torque and momentum management of the reaction wheels. The magnetic moment of each rod is 0.2 Am^2. This magnetic moment $\mathbf{M}$ reacts with the local geomagnetic field $\mathbf{B}_{local}$ to create a control torque $\mathbf{N}_M$. The basic magnetic torque control equation [25] is given by:

$$\mathbf{N}_M = \mathbf{M} \times \mathbf{B}_{local} \tag{2.2.2}$$

A pulse width modulation method is used to control the on-time of the magnetic torque rods [26]. The minimum pulse width that can be used per sample period is 1 milli-second. The maximum pulse width is restricted to 80% of the sampling period of the controller. This restriction guarantees that the generated magnetic moments of the torque rods do not corrupt the magnetometer reading when it is sampled.

2.3 Satellite Attitude Motion

The change in the attitude of the satellite can be mathematically modelled by its kinematic and dynamic equations [10]. The kinematic equation focus on the change in the attitude parameters without including the forces that cause the change. The quaternion representation of the kinematic equation is given by:

$$\begin{bmatrix} \dot{q}_1 \\ \dot{q}_2 \\ \dot{q}_3 \\ \dot{q}_4 \end{bmatrix} = \frac{1}{2} \begin{bmatrix} 0 & \omega_{oz} & -\omega_{oy} & \omega_{ox} \\ -\omega_{oz} & 0 & \omega_{ox} & \omega_{oy} \\ \omega_{oy} & -\omega_{ox} & 0 & \omega_{oz} \\ -\omega_{ox} & -\omega_{oy} & -\omega_{oz} & 0 \end{bmatrix} \begin{bmatrix} q_1 \\ q_2 \\ q_3 \\ q_4 \end{bmatrix} \tag{2.3.1}$$

where ω_{ox}, ω_{oy} and ω_{oz} are the elements of the orbit referenced body rate vector $\boldsymbol{\omega}_B^O$ of the satellite. This body rate vector can be expressed in terms of the ECI body rate vector $\boldsymbol{\omega}_B^I$ as:

$$\boldsymbol{\omega}_B^O = \boldsymbol{\omega}_B^I - \mathbf{A}_{O/B} \begin{bmatrix} 0 & -\omega_o & 0 \end{bmatrix}^T \tag{2.3.2}$$

where ω_o is the magnitude of the orbital rate for a circular orbit and $\mathbf{A}_{O/B}$ is the vector transformation matrix from the ORC to the SBC frame.

The dynamic equation models the effect of applied torques on the rate of change of the angular velocity vector of the satellite.

$$\mathbf{I}\dot{\boldsymbol{\omega}}_B^I = \mathbf{N}_{GG} + \mathbf{N}_M + \mathbf{N}_{Aero} - \boldsymbol{\omega}_B^I \times \left(\mathbf{I}\boldsymbol{\omega}_B^I + \mathbf{h}\right) - \dot{\mathbf{h}} \tag{2.3.3}$$

with $\boldsymbol{\omega}_B^I$ the inertially referenced body rate vector, ω_o the magnitude of the orbit rate, $\mathbf{N}_M$ the magnetic control torque and $\mathbf{h}$ the angular momentum vector of the reaction wheels. It is assumed that the only significant external disturbance torques on the spacecraft are those due to the gravity gradient $\mathbf{N}_{GG}$ and aerodynamic drag $\mathbf{N}_{Aero}$ forces. The modelling of these forces are presented in Section 2.4. The moment of inertia tensor $\mathbf{I}$ was defined in Section 2.2.

2.4 Disturbance Torques

In this project only two environmental disturbance torques are included in the dynamic equation of the satellite model. These are the aerodynamic $\mathbf{N}_{Aero}$ and gravity gradient $\mathbf{N}_{GG}$ torques.

2.4.1 Aerodynamic Torque

Aerodynamic torques are induced on the satellite when gas molecules in the atmosphere of Earth collides with the surface of the satellite and transfer momentum to it. The authors of [27] used partial accommodation theory to describe the force induced by this momentum transfer on a specific surface area of the satellite. With the force known, they derived the aerodynamic torque as the cross-product of the displacement vector from the COM to the COP $\mathbf{r}_{m/p}$ and the induced force vector.

The partial accommodation theory models the momentum transfer as two possible phenomena. The first is specular reflection of the molecules where the angle of reflection is equal to the incidence angle. This results in momentum transfer normal to the surface area. The second form is diffuse reflection where the gas molecules are accommodated to the surface area for some time before leaving it again at different velocities and in various directions [28]. The extent to which these two phenomena influence the satellite is incorporated into the aerodynamic torque model by means of the normal σ_n and tangential σ_t accommodation coefficients.

The values of these coefficients are dependent on various elements like the spacecraft materials used and the surface temperature of the satellite. They can vary between zero and one, zero presenting full specular reflection and one the complete accommodation of particles with diffuse reflection. For this project a value of 0.8 is assumed for both σ_n and σ_t which correlates to the values proposed by Hughes [28] for satellites.

Other elements that are needed for the derivation of the aerodynamic torque are the relative velocity between the spacecraft and the atmosphere, the displacement vectors

$\mathbf{r}_{m/p}$ from the COM to the COP of each affected surface area, the inward-pointing normal vectors to these surfaces and the local atmospheric density.

The relative velocity between the satellite and the atmosphere is dominated by the orbital velocity vector $\mathbf{v}_o$ of the satellite and the rotation of the atmosphere of Earth. Assuming a near circular polar orbit, the angle $x_{o,east}$ between the co-rotating atmosphere and the orbital path can be determined as:

$$x_{o,east} = \begin{cases} \pi - arctan\left(\frac{d\lambda/dt}{d\phi/dt}\right) & \text{for } \frac{d\phi}{dt} < 0 \\ \frac{\pi}{2} & \text{for } \frac{d\phi}{dt} = 0 \\ -arctan\left(\frac{d\lambda/dt}{d\phi/dt}\right) & \text{for } \frac{d\phi}{dt} > 0 \end{cases} \tag{2.4.1}$$

where λ represents the satellite latitude and ϕ the longitude. The local atmospheric velocity vector in the SBC frame is given by:

$$\mathbf{v}_A^B = \mathbf{A}_{O/B} \begin{bmatrix} -\|\mathbf{v}_o\| + \omega_E \|\mathbf{R}\| \cos(\lambda) \cos(x_{o,east}) \\ -\omega_E \|\mathbf{R}\| \cos(\lambda) \sin(x_{o,east}) \\ 0 \end{bmatrix} \tag{2.4.2}$$

where $\|\mathbf{v}_o\|$ is the orbital velocity magnitude, ω_E is the rotation rate of Earth and $\|\mathbf{R}\|$ is the magnitude of the satellite's orbital radius [21].

The COP of a surface is assumed to be at its geometrical centre and the COM is as defined in Section 2.1. The displacement vectors for the two aerodynamic roll paddles and the four feathers are given in Table 2.1.

Table 2.1: Displacement vectors of the aerodynamic surfaces areas.

Element name	Displacement vector $\mathbf{r}_{m/p}$ (m)
$+Z_B$ Paddle	$[0.13, \quad 0, \quad 0.18]^T$
$-Z_B$ Paddle	$[0.13, \quad 0, -0.18]^T$
Feather 1	$[-0.45, \quad 0.11, \quad 0.11]^T$
Feather 2	$[-0.45, -0.11, \quad 0.11]^T$
Feather 3	$[-0.45, -0.11, -0.11]^T$
Feather 4	$[-0.45, \quad 0.11, -0.11]^T$

Each aerodynamic element has two prominent aerodynamic surfaces, with their inward-pointing normal vectors in opposite directions. To determine on which side of the aerodynamic elements the atmospheric molecules collide, the Heaviside function $H\{x\}$ is used. This function is used to evaluate the cosine of the incidence angle α that can be determined as the dot product of the local atmospheric velocity unit vector $\bar{\mathbf{v}}_A^B$ with the

inward-pointing normal unit vector $\bar{\mathbf{n}}$ of the evaluated surface:

$$\cos(\alpha) = \bar{\mathbf{v}}_A^B \cdot \bar{\mathbf{n}} \tag{2.4.3}$$

If $\cos(\alpha) \geq 0$, then the Heaviside function results in a one and if $\cos(\alpha) < 0$ then $H\{\cos(\alpha)\} = 0$.

The atmospheric density ρ needed for the computation of the aerodynamic torque can be calculated using an exponential model [29],

$$\rho = \rho_o \exp\left[-\frac{h - h_o}{H}\right] \tag{2.4.4}$$

where h is the orbit altitude within the range 450 to 500 km, $h_o = 450\,\text{km}$ is the base altitude, $H = 60.828\,\text{km}$ is the scale height and $\rho_o = 1.585 \times 10^{-12}$ is the nominal atmospheric density in the sunlit part of the orbit. During eclipse the nominal atmospheric density is approximated as $\frac{1}{2}\rho_o$ [26].

The final model of the induced aerodynamic torque of a specific surface of the satellite is derived by [27] as:

$$\begin{aligned}\mathbf{N}_{Aero} =& \rho \left\|\mathbf{v}_A^B\right\|^2 A_p \left[\sigma_t(\mathbf{r}_{m/p} \times \bar{\mathbf{v}}_A^B) + (\sigma_n \left(v_b / \left\|\mathbf{v}_A^B\right\|\right)\right. \\ &\left. + (2 - \sigma_n - \sigma_t)\cos(\alpha))(\mathbf{r}_{m/p} \times \bar{\mathbf{n}})\right]\end{aligned} \tag{2.4.5}$$

with

$$A_p = H\{\cos(\alpha)\}\cos(\alpha) A_{surface} \tag{2.4.6}$$

where $A_{surface}$ is the exposed surface area of the aerodynamic element. The factor $v_b / \left\|\mathbf{v}_A^B\right\|$ represents the relation between magnitude of the local atmospheric velocity and the molecular exit velocity v_b when diffuse reflection occurs. It is assumed that v_b equals 5% of the local atmospheric velocity that leads to $v_b / \left\|\mathbf{v}_A^B\right\| = 0.05$. To determine the total induced aerodynamic torque on the satellite (2.4.5) must be evaluated for all the aerodynamic feather and paddle surfaces. It must be noted that the shadowing of elements is not considered in this project.

2.4.2 Gravity Gradient Torque

The gravity gradient disturbance torque on a satellite is caused by the gravitational force of Earth. This force is inversely proportional to the magnitude of the orbital radius $\|\mathbf{R}\|$ cubed. It can be used to stabilise an elongated satellite passively with the longitudinal axis of the satellite aligned with the nadir vector.

The gravity gradient torque [20] can be determined by:

$$\mathbf{N}_{GG} = \frac{3\mu}{\|\mathbf{R}\|^3}\left(\mathbf{u}_e \times \mathbf{I}\mathbf{u}_e\right) \tag{2.4.7}$$

$$= \frac{3\mu}{\|\mathbf{R}\|^3}\begin{bmatrix}\left(I_{zz} - I_{yy}\right)A_{23}A_{33}\\ \left(I_{xx} - I_{zz}\right)A_{13}A_{33}\\ \left(I_{yy} - I_{xx}\right)A_{13}A_{23}\end{bmatrix} \tag{2.4.8}$$

where $\mu = 398600.5\,\mathrm{km}^3/\mathrm{s}^2$ is the gravitational constant of Earth, $\mathbf{u}_e = \mathbf{A}_{O/B}\begin{bmatrix}0 & 0 & 1\end{bmatrix}^T$ is the unit vector towards nadir in satellite body coordinates and $\mathbf{I}$ is the satellite's moment of inertia tensor.

2.5 Summary

In order to describe the position and attitude of the satellite, three coordinate systems are needed. The satellite body coordinate frame is used to describe the position of the sensors and actuators in the satellite. All measurements are made with respect to this reference frame. The orbit reference frame is used to describe the attitude of the satellite. The position of the satellite can be described in terms of the earth centred inertial frame. The modelled vectors are produced with respect to this reference frame. The use of Euler angles and quaternions are discussed, as well as the different transformation matrices needed to convert vectors from one coordinate frame to another.

The satellite's external structure was designed to suit aerodynamic control of the satellite. It consists of a 3U main bus, two aerodynamic roll control paddles and four aerodynamic feather antennae. The paddles are used for active roll control while the feathers form a passive pitch-yaw stabilisation system [8]. The 1U at the front of the main bus is dedicated to the attitude determination and control system. The sensors and actuators used comprise of a magnetometer, fine sun sensor, nadir sensor, three magnetic torque rods, the roll control paddles and three nano-reaction wheels.

The satellite's change in attitude can be modelled by the kinematic and dynamic equations [10]. The kinematic equation illustrates the change in the attitude of the satellite irrespective of the torques that caused the change. The dynamic equation models the effect of these external and control torques on the time-derivative of the angular momentum vector. Only two environmental disturbance torques are included in this project's dynamic equation, namely the gravity gradient torque and the aerodynamic torque. In this project, however, the aerodynamic torque is incorporated as a control torque by choosing an appropriate structure for the satellite.

Chapter 3

Simulation Environment

In order to test the attitude determination methods of Chapter 4 and the control methods discussed in Chapter 5, a simulation environment is required. The final orbit for this project has not yet been decided on and the simulations are based on the orbit parameters of an existing satellite whose orbit corresponds with the orbital needs of this project.

A simulation environment is set up in *Matlab* that consists of three control blocks, a satellite dynamic and kinematic model, an orbit propagator, as well as models of the space environment of the satellite and an attitude determination block. The final *Simulink* model and its various subsystems are discussed in this chapter.

3.1 Orbital Elements

The simulation orbit used in this project is the orbit of the SumbandilaSat microsatellite. The orbit information, shown in Table 3.1, is extracted from a set of two line elements (TLE) provided by the North American Aerospace Defence Command (NORAD) that monitors man-made objects in space [30].

Table 3.1: Simulation orbit information.

Parameter	Value
Eccentricity	0.0002704
Inclination	97.2927°
Semi-major axis	6 879.55 km
Mean motion	15.215 rev/day
Period	5 678.7 seconds

The simulation orbit is a near circular sun-synchronous polar orbit with an eccentricity

of 0.0002704. The orbit is retrograde, meaning that the satellite moves from east to west, with an inclination of 97.29°. The semi-major axis of the orbit is 6 879.55 km and relates to an orbital height of approximately 500 km. The satellite has a mean motion of 15.215 revolutions per day in this orbit with an orbit period of 5 678.7 seconds. For a 9 am/pm sun-synchronous orbit the eclipse time T_E is calculated as 1 829.6 seconds which is 32.2% of the orbit period. In Figure 3.1 the rising edge of the rectangular wave represents the transition from eclipse to the sunlit part of the orbit and the falling edge represents the transition back to eclipse. All simulations will experience the same eclipse and sunlit parts.

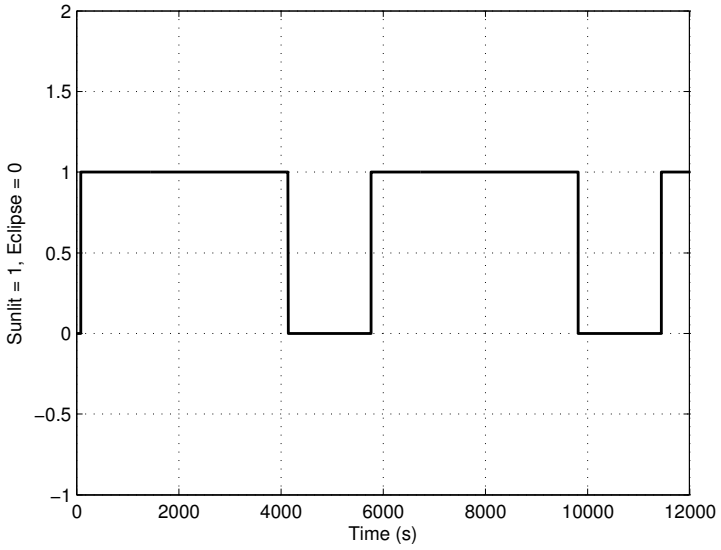

Figure 3.1: Eclipse and sunlit parts of the simulation.

3.2 Simulation Environment

A simplified representation of the simulation environment as a control loop is shown in Figure 3.2. It consists of three control blocks, the satellite model and two blocks representing the sensors and estimation methods of the satellite. The simulation has a fixed time step of 1 second. The simulation time is chosen to best suit the specific control or estimation method being tested. The contents of the simulation blocks, the inputs they require and the outputs they provide are discussed in this section.

3.2.1 Plant

The plant in the control loop is represented by the *satellite model* block shown in Figure 3.3. The *satellite model* is the implementation of the kinematic and dynamic equations of the satellite discussed in Section 2.3. It requires the principle moments of inertia of

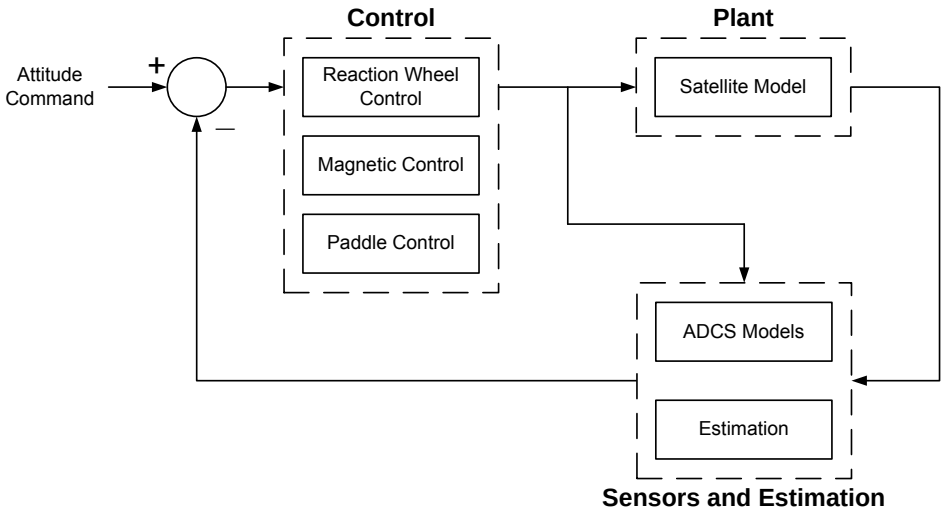

Figure 3.2: Simulation environment as a control loop.

the satellite, the generated aerodynamic, magnetic and wheel control torques, the angular momentum vector of the reaction wheels, the orbital rate and the radius of the satellite. The initial attitude and angular body rate vector of the satellite for the simulation can be set as an input to this block. The outputs of the *satellite model* are the current true attitude of the satellite expressed as the quaternion vector and the direction cosine matrix and the true ORC and ECI angular body rate vectors.

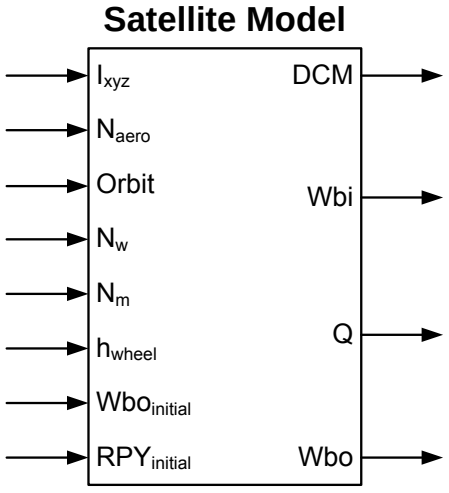

Figure 3.3: Satellite Model.

3.2.2 Sensors and Estimation

The *ADCS models* and the *estimation* blocks shown in Figure 3.4 form part of the sensors and estimation subsystem. The *ADCS models* block consists of mathematical models of the satellite's position and the space environment. The Simplified General Perturbations

No. 4 (SGP4) model [31] is used to propagate the satellite's orbit using the NORAD TLE information set. It provides modelled values for the orbital rate, the mean and true anomaly, the latitude and longitude of the satellite, the orbital radius and the inertial position and velocity unit vectors of the satellite. These two vectors are used as described by (2.1.12) to determine the transformation matrix $\mathbf{A}_{I/O}$ from the ECI to the OBC frame.

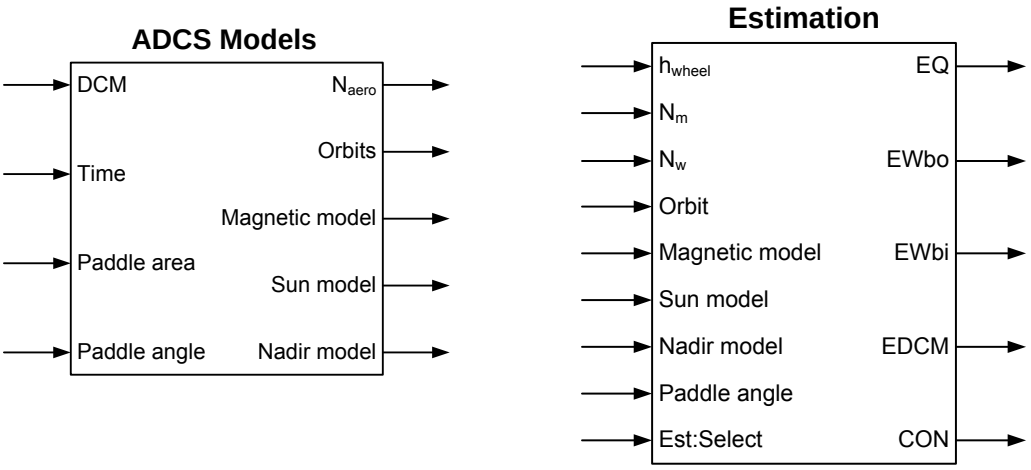

(a) ADCS Models block (b) Estimation block

Figure 3.4: Sensors and estimation subsystem.

A sun orbit propagator is included to determine the ECI position, longitude and latitude of the sun. It requires only the current Julian date of the simulation that can be derived from the TLE information set and the simulation time. The latitude and longitude values of the sun and the satellite are used in the *sun model* to determine the modelled satellite-to-sun unit vector in the ECI frame.

A 10th order International Geomagnetic Reference Field (IGRF) model [32] is used to model the Earth's magnetic field and to determine the local geomagnetic field vector of the satellite relative to the ECI frame [10]. It forms part of the *magnetic model* in the *ADCS Models* block and requires the radius, the latitude and longitude of the satellite and the ECI position unit vector of the satellite. In the *nadir model*, the modelled ORC nadir unit vector is set to $\bar{\mathbf{n}}_O = \begin{bmatrix} 0 & 0 & 1 \end{bmatrix}^T$ due to the definition of Z_O-axis of the ORC frame to be nadir pointing.

The modelled satellite-to-sun unit vector, local geomagnetic field vector and the nadir unit vector are transformed from the ECI frame to the ORC frame using the transformation matrix $\mathbf{A}_{I/O}$. These transformed vectors are used in the control and attitude determination algorithms.

Another model within the *ADCS models* block is the *aerotorq model*. It is used to determine the aerodynamic disturbance torque that affects the satellite. These torques are

induced by gas molecules that collide with the aerodynamic roll paddles and feather antennae, as discussed in Section 2.4.1. The model requires the orbital rate, the latitude, longitude and radius of the satellite, the surface area of the roll control paddles, the paddle rotation angle and the true direction cosine matrix (DCM), also known as the transformation matrix $\mathbf{A}_{O/B}$.

The *ADCS models* block is also used in the simulation environment to generate the three sensor measurement vectors, namely the nadir vector, sun vector and geomagnetic field vector. The true DCM is used to convert the modelled ORC vectors to the SBC frame. Normal distributed noise is added to each vector to produce realistic measurement vectors that are used in attitude determination and control algorithms of the simulation. More detail of the noise characteristics is provided in Section 4.4.

The *estimation* block contains all the attitude determination methods discussed in Chapter 4. It requires the measurement and modelled vector sets of the *sun model*, *nadir model* and *magnetic model*. The paddle rotation angle from the paddle controller, angular momentum vector of the reaction wheels and the generated magnetic and wheel control torques are also needed. From the orbit propagator the orbital rate, the latitude, longitude and radius of the satellite are required. The *Select:Est* input is used to choose the determination method and the various options are shown in Table 3.2. Depending

Table 3.2: Selection of the determination methods.

Determination method	Select
Magnetic Rate Kalman filter	1
Sun Rate Kalman filter and Triad	5
Extended Kalman filter	10

on the determination algorithm used, the *estimation* block can produce the estimated ORC body rate vector $\boldsymbol{\omega}_B^O$, the ECI body rate vector $\boldsymbol{\omega}_B^I$, a control signal that indicates whether it is a valid control period and the estimated attitude of the satellite expressed as quaternions or in the form of the transformation matrix $\mathbf{A}_{O/B}$. The estimated quaternion vector is used to determine the quaternion error vector defined by (2.1.10).

3.2.3 Control

There are three controller blocks in the simulation, namely *magnetic control*, *reaction wheel control* and *paddle control*, that incorporate the control algorithms discussed in Chapter 5.

The *magnetic control* block contains all magnetic controllers of the simulation and is shown in Figure 3.5(a). It requires the estimated ORC body rate vector, the quaternion error vector, the measurement and modelled vector pair of the *magnetic model*, the angular momentum reference value for the reaction wheel aligned with the Y_B-axis, the reference pitch rate of the satellite, the angular momentum vector of the reaction wheels and the valid control period signal. The output is the generated magnetic control torque.

All the reaction wheel controllers are incorporated in the *reaction wheel control* block shown in Figure 3.5(b). These controllers require the angular momentum reference value for the Y_B-axis reaction wheel, the initial angular momentum vector of the reaction wheels, the estimated ORC body rate vector, the quaternion error vector and the valid control period signal. The *reaction wheel control* block outputs consist of the angular momentum vector of the reaction wheels and the generated wheel control torque.

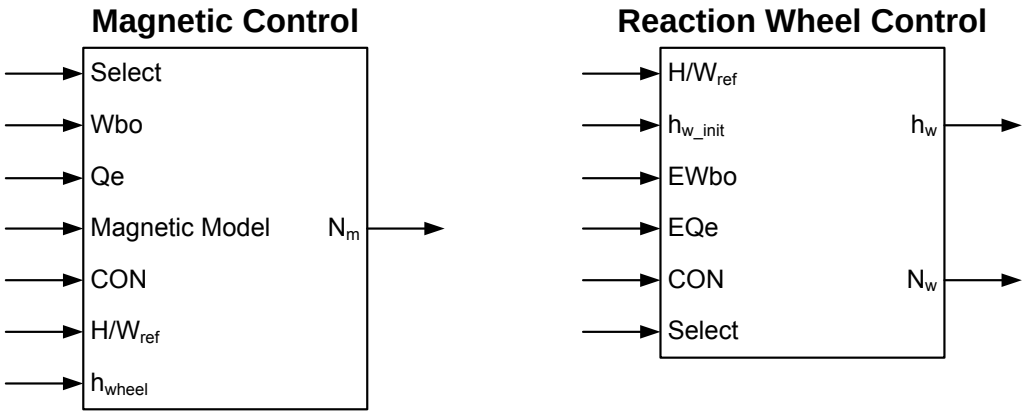

(a) Magnetic control (b) Reaction wheel control

Figure 3.5: Control subsystem: magnetic and reaction wheel control.

The *paddle control* block includes the aerodynamic roll paddle controller of Section 5.2.2. It requires the estimated ORC body rate vector, the quaternion error vector and the valid control period signal. The output of this block, shown in Figure 3.6, is the required paddle rotation angles.

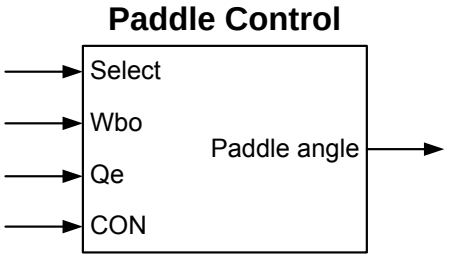

Figure 3.6: Control subsystem: paddle control

The *Select* inputs of the three control blocks are used to choose from the various control algorithms. A summary of the selection options are given in Table 3.3.

Table 3.3: Selection of control methods.

Control method	Select
Magnetic Control	Select:Mag
XProd	1
RW Desaturation	2
B-dot	3
B-dot and Y-spin	4
Compass-like PID	6
Nutation damping	7
Paddle Control	Select:Paddle
Off	0
On	1
Reaction Wheel Control	Select:Wheel
Y-Bias	1
Pitch axis	2
Quaternion feedback	3

3.2.4 Simulink Model

The final Simulink simulation model used in this project is shown in Figure 3.7. It includes all the simulation subsystems discussed above and shows how the simulation blocks are connected to one another.

3.3 Summary

In this chapter the simulation environment used to evaluate the attitude determination and control methods of this project was discussed. The 500 km near circular polar orbit of the SumbandilaSat microsatellite was chosen as the simulation orbit, since the final orbit for this project has not yet been established. The important orbit parameters of this orbit were presented and discussed.

The various subsystems of the simulation environment as a control loop were discussed in terms of their purpose, the required inputs and the produced outputs. The plant consists of the *satellite model* that represents the implementation of the kinematic and dynamic

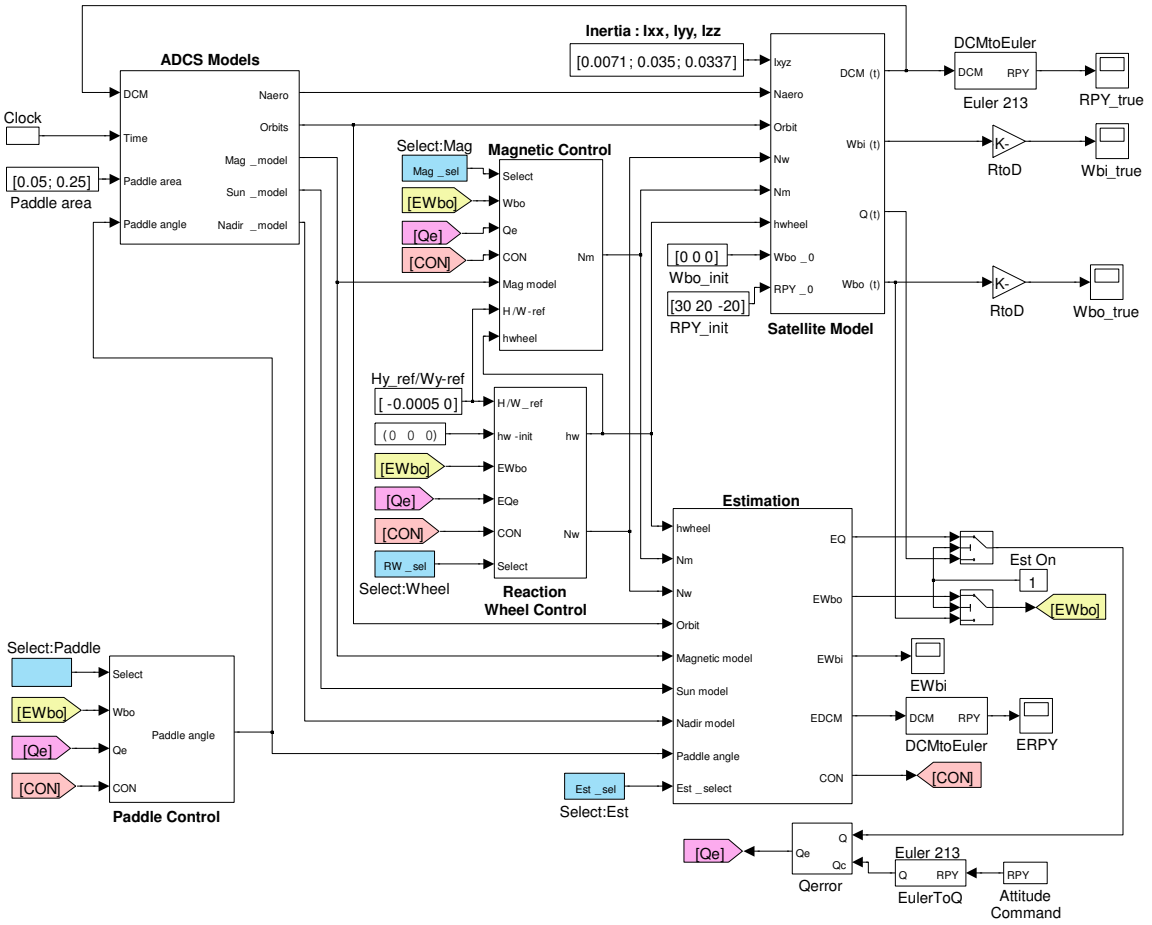

Figure 3.7: Simulink Model.

equations to describe the true attitude of the satellite. The sensors and estimation subsystem consists of two simulation blocks. The *ADCS models* block is used to propagate the orbit of the satellite and to model the space environment. The *estimation* block is used to implement all the attitude determination methods of Chapter 4. The control subsystem consists of three control blocks, namely *magnetic control*, *paddle control* and *reaction wheel control*. These blocks are used to implement the control methods of Chapter 5. The final *Simulink* model shows the connections between the simulation blocks of the subsystems in more detail.

Chapter 4

Attitude Determination

In most cases it is necessary to know the current attitude and motion of the satellite in space. In Section 3.2 the orbit model that provides an estimated satellite position and velocity was briefly discussed. The only other components needed are the satellite orientation and rotational velocity relative to a known reference frame, in this case the orbit reference frame.

The satellite has sensors that produce body referenced vector components. These sensors provide the sun-, nadir- and geomagnetic field vector measurements. The FOV constraints and the placement of the sensors in the ADCS 1U of the satellite are discussed in Section 2.2.1. From the mathematical models in Section 3.2 orbit referenced versions of these vectors can be produced. Incorporating these vector components in different algorithms, the orientation and rotational velocity of the satellite can be estimated. Three attitude determination algorithms are discussed in this chapter. These include the Triad, Rate Kalman Filter and Extended Kalman Filter (EKF) algorithms.

The Triad algorithm only determines the orientation of the satellite. A triad is defined by Halmos [33] as a set of three linear independent unit vectors that can define a coordinate system. Two measurement vectors and their corresponding modelled vectors are used to form two orthonormal triads. These triads can then be used to construct the transformation matrix from the ORC frame to the SBC frame. From this matrix the satellite orientation in quaternions or Euler angles can be calculated [34].

The Rate Kalman Filter estimators as presented by [21, 26] are used to determine the angular rate vector of the satellite from either the magnetometer or the sun sensor measurements. The magnetic RKF estimator can produce an estimated ORC body rate vector during the whole orbit path. Although it has average estimation errors, it is sufficient to use during the tumbling periods of the satellite. The sun RKF estimator is more accurate, but it produces an inertially referenced rate vector. Since an ORC rate vector is

required, this estimator must be used in collaboration with the Triad algorithm in order to transform the estimated rate vector from the ECI frame to the ORC frame.

The Extended Kalman Filter can be used to determine the full satellite state, i.e. the ECI referenced rate vector and satellite's orientation in quaternions. This algorithm uses all valid measurement vectors available, as well as their corresponding ORC modelled vectors [35].

These attitude determination methods are discussed in this chapter and simulation results are shown. Each method has its advantages and disadvantages that influences the choice of estimator used during the different control modes.

4.1 Triad Algorithm

The Triad algorithm is used to determine the transformation matrix $\mathbf{A}_{O/B}$ from the ORC frame to the current SBC frame. This is done by constructing two triads that consist of three base unit vectors each. The one triad is constructed from two measured unit vectors in the SBC frame and the other from the corresponding modelled ORC unit vectors. These triads can represent the transformation matrices from the reference frame of the used vectors to a mutual transit reference coordinate (TRC) frame [34].

Any two vector sets can be used, but in this application the nadir $\bar{\mathbf{n}}$ and satellite-to-sun $\bar{\mathbf{s}}$ unit vectors were chosen for their measurement accuracy.

The transit reference frame is constructed by assuming that one of the SBC/ORC vector pairs is correct, thus assuming there are no measurement or model errors. Since the modelled nadir vector $\bar{\mathbf{n}}_O = \begin{bmatrix} 0 & 0 & 1 \end{bmatrix}^T$ in ORC is definitely correct due to the definition of the Z_O-axis, this pair will form the first base vector of the TRC:

$$\bar{\mathbf{t}}_{1,B} = \bar{\mathbf{n}}_B \tag{4.1.1}$$

$$\bar{\mathbf{t}}_{1,O} = \bar{\mathbf{n}}_O \tag{4.1.2}$$

The second base vector of the triads is in the direction perpendicular to the sun and nadir observations:

$$\bar{\mathbf{t}}_{2,B} = \frac{\bar{\mathbf{n}}_B \times \bar{\mathbf{s}}_B}{|\bar{\mathbf{n}}_B \times \bar{\mathbf{s}}_B|} \tag{4.1.3}$$

$$\bar{\mathbf{t}}_{2,O} = \frac{\bar{\mathbf{n}}_O \times \bar{\mathbf{s}}_O}{|\bar{\mathbf{n}}_O \times \bar{\mathbf{s}}_O|} \tag{4.1.4}$$

The third base vector is chosen to complete the triad sets:

$$\bar{\mathbf{t}}_{3,B} = \bar{\mathbf{t}}_{1,B} \times \bar{\mathbf{t}}_{2,B} \tag{4.1.5}$$

$$\bar{\mathbf{t}}_{3,O} = \bar{\mathbf{t}}_{1,O} \times \bar{\mathbf{t}}_{2,O} \tag{4.1.6}$$

The transformation matrices from the TRC frame to the SBC or ORC frame can now be constructed from these triads:

$$\mathbf{A}_{T/B} = \begin{bmatrix} \bar{\mathbf{t}}_{1,B} & \bar{\mathbf{t}}_{2,B} & \bar{\mathbf{t}}_{3,B} \end{bmatrix} \tag{4.1.7}$$

$$\mathbf{A}_{T/O} = \begin{bmatrix} \bar{\mathbf{t}}_{1,O} & \bar{\mathbf{t}}_{2,O} & \bar{\mathbf{t}}_{3,O} \end{bmatrix} \tag{4.1.8}$$

From these two transformation matrices the vector transformation matrix from the ORC frame to the SBC frame is obtained:

$$\mathbf{A}_{O/B} = \mathbf{A}_{T/B}\mathbf{A}_{O/T} \tag{4.1.9}$$

where $\mathbf{A}_{O/T}$ is the transpose of the transformation matrix $\mathbf{A}_{T/O}$. Comparing the components of the matrix $\mathbf{A}_{O/B}$ with the quaternion version mentioned in Section 2.3 the estimated satellite attitude, in quaternions, can be derived as:

$$\hat{q}_1 = \frac{A_{23} - A_{32}}{4\hat{q}_4} \tag{4.1.10}$$

$$\hat{q}_2 = \frac{A_{31} - A_{13}}{4\hat{q}_4} \tag{4.1.11}$$

$$\hat{q}_3 = \frac{A_{12} - A_{21}}{4\hat{q}_4} \tag{4.1.12}$$

$$\hat{q}_4 = 0.5\sqrt{1 + A_{11} + A_{22} + A_{33}} \tag{4.1.13}$$

where A_{ij} represents the different elements of the transformation matrix $\mathbf{A}_{O/B}$. This estimated quaternion vector can then be used in the control algorithms.

4.2 Rate Kalman Filter Estimator

In order to control the aerodynamic satellite, the ORC body rate vector is required. Since the satellite possesses no sensors to measure the angular rate vector directly, the measurements of the attitude sensors must be used to compute the angular rates by means of a Rate Kalman Filter algorithm.

The Kalman Filter is an optimal recursive data processing algorithm first introduced by R.E. Kalman in 1960 [36]. Since then, it has become a very useful tool in the fields of navigation and aerospace to solve attitude and orbit determination problems. The Kalman Filter makes use of a dynamic system model, consecutive sensor measurements

over time, statistical descriptions of the expected measurement errors and the uncertainty of the dynamic model accuracy, also referred to as system noise, to produce an optimal state estimate.

In this section two, versions of a RKF estimator is presented. The magnetic RKF, as presented by [26], uses the rate of change of the geomagnetic field vector measurement to determine the estimated orbit referenced body rate vector. The magnetic RKF was modified by [21] to produce the sun RKF. This filter uses the fine sun vector measurement as input for the rate estimator and produces an inertially referenced angular body rate vector.

For both these RKF estimators a system and measurement model are constructed from which the different elements will be used in the Rate Kalman Filter algorithm presented in Section 4.2.3.

4.2.1 Magnetic Rate Kalman Filter Estimator

During the initial stages of the satellite's lifetime, after the deployment of all mechanical parts, the satellite might experience high tumbling rates. In order to reduce these rates and to control the satellite to a desired attitude, the angular body rate of the satellite must be determined. The magnetic RKF [26] fulfils this role by using the rate of change of the geomagnetic field vector measurement.

One problem with using this vector is that it is not inertially fixed. In the case of a polar orbit, the geomagnetic field vector rotates twice with respect to the inertial frame and once with respect to the orbital frame per orbit. This rotation is mainly about the orbit normal direction and will cause estimation errors in the corresponding angular rate elements. The smallest estimation error can be expected if the orbit referenced body rate vector is determined.

4.2.1.1 Magnetic RKF System Model

The state vector is defined as the orbit referenced body rate vector:

$$\mathbf{x}_m(t) = \boldsymbol{\omega}_B^O(t) \tag{4.2.1}$$

where the subscript m designates it as the *magnetically* determined state vector. The dynamic equation presented in Section 2.3 can be simplified to:

$$\dot{\boldsymbol{\omega}}_B^I = \mathbf{I}^{-1}\left(\mathbf{N}_M + \mathbf{N}_D\right) \tag{4.2.2}$$

with

$$\mathbf{I}^{-1} = \begin{bmatrix} I_{xx}^{-1} & 0 & 0 \\ 0 & I_{yy}^{-1} & 0 \\ 0 & 0 & I_{zz}^{-1} \end{bmatrix} \tag{4.2.3}$$

where I_{xx}, I_{yy} and I_{zz} are the principle moments of inertia as calculated in Section 2.2. $\mathbf{N}_D$ represents all external disturbance torques on the satellite and the gyroscopic coupling terms, but excludes the magnetic control torque $\mathbf{N}_M$. The dynamic equation can be rewritten in terms of the state vector using the relationship given in (2.3.2):

$$\dot{\mathbf{x}}_m = \dot{\boldsymbol{\omega}}_B^O = \mathbf{I}^{-1}\left(\mathbf{N}_M + \mathbf{N}_D\right) + \dot{\mathbf{A}}_{O/B}\begin{bmatrix} 0 & \omega_o & 0 \end{bmatrix}^T \tag{4.2.4}$$

The last term comprises of the derivative of transformation matrix and the orbital rate vector. This term is usually unknown during the implementation of this filter. It amounts to values in the same order of the disturbance torques and is therefore modelled with the system noise.

From (4.2.4) the continuous time system model can be formed:

$$\dot{\mathbf{x}}_m(t) = \mathbf{G}\mathbf{u}_m(t) + \mathbf{s}_m(t) \tag{4.2.5}$$

where $\mathbf{G} = \mathbf{I}^{-1}$, $\mathbf{u}_m(t) = \mathbf{N}_M(t)$ and $\mathbf{s}_m(t) = \mathbf{I}^{-1}\mathbf{N}_D(t) + \dot{\mathbf{A}}_{O/B}$. This model can be converted to a discrete time version:

$$\mathbf{x}_m(k+1) = \boldsymbol{\Phi}\mathbf{x}_m(k) + \boldsymbol{\Gamma}\mathbf{u}_m(k) + \mathbf{s}_m(k) \tag{4.2.6}$$

$$\mathbf{s}_m(k) = \mathbf{N}\left\{\mathbf{0}, \mathbf{Q}(k)\right\} \tag{4.2.7}$$

where $\boldsymbol{\Phi}$ is a 3×3 identity matrix, $\boldsymbol{\Gamma} = (\mathbf{I}^{-1}T_s)$ with T_s the sampling period of the discrete system and (4.2.7) representing the system noise model with a zero mean and a covariance matrix $\mathbf{Q}(k)$.

4.2.1.2 Magnetic RKF Measurement Model

When determining the measurement model, the assumption is made that if the sample period is short enough, the current measurement will only differ from the previous measurement due to a small rotation of the satellite. The measurement model will therefore make use of a small angle approximation of the transformation matrix given in (2.1.1) that results in:

$$\Delta\mathbf{A}_m \approx \begin{bmatrix} 1 & \psi & -\theta \\ -\psi & 1 & \phi \\ \theta & -\phi & 1 \end{bmatrix} \tag{4.2.8}$$

Assuming that the angular rate stays constant during sample time k, these rotation angles can be approximated as $\phi \approx \omega_{xo}(k)T_s$, $\theta \approx \omega_{yo}(k)T_s$ and $\psi \approx \omega_{zo}(k)T_s$ where $\omega_{xo}(k)$, $\omega_{yo}(k)$ and $\omega_{zo}(k)$ are the vector elements of the ORC body rate vector $\boldsymbol{\omega}_B^O(k)$. From these approximations the transformation matrix now becomes:

$$\begin{aligned}\Delta\mathbf{A}_m &\approx \mathbf{1}_{3\times3} + \Lambda_m\left\{\boldsymbol{\omega}_B^O(k)\right\} \\ &= \mathbf{1}_{3\times3} + \begin{bmatrix} 0 & \omega_{zo}(k)T_s & -\omega_{yo}(k)T_s \\ -\omega_{zo}(k)T_s & 0 & \omega_{xo}(k)T_s \\ \omega_{yo}(k)T_s & -\omega_{xo}(k)T_s & 0 \end{bmatrix}\end{aligned} \tag{4.2.9}$$

where $\mathbf{1}_{3\times3}$ is a 3×3 identity matrix and $\Lambda_m\{\}$ is a matrix function. If the orbit referenced vector measurement of the previous time step $\mathbf{v}(k-1)$ is known, the predicted measurement vector at the current time step can be represented by

$$\mathbf{v}(k) = \Delta\mathbf{A}_m\mathbf{v}(k-1) \tag{4.2.10}$$

The rate of change of the successive orbit referenced measurements is used to determine the following measurement model from (4.2.9) and (4.2.10):

$$\begin{aligned}\mathbf{y}(k) &= \Delta\mathbf{v}(k) \\ &= \mathbf{v}(k) - \mathbf{v}(k-1) \\ &= \Lambda_m\left\{\boldsymbol{\omega}_B^O(k)\right\}\mathbf{v}(k-1) \\ &= \mathbf{H}(k)\mathbf{x}_m(k) + \mathbf{m}_m(k)\end{aligned} \tag{4.2.11}$$

with

$$\mathbf{H}(k) = \begin{bmatrix} 0 & -v_z(k-1)T_s & v_y(k-1)T_s \\ v_z(k-1)T_s & 0 & -v_x(k-1)T_s \\ -v_y(k-1)T_s & v_x(k-1)T_s & 0 \end{bmatrix} \tag{4.2.12}$$

and

$$\mathbf{m}_m(k) = \mathbf{N}\left\{\mathbf{0}, \mathbf{R}(k)\right\} \tag{4.2.13}$$

where $\mathbf{H}(k)$ is the state output matrix and $\mathbf{m}_m(k)$ represents the measurement noise model with a zero mean and a covariance matrix $\mathbf{R}_m(k)$.

4.2.2 Sun Rate Kalman Filter Estimator

This estimator is a modified version of the magnetic RKF rate estimator and was first presented by [21]. The difference is that the sun RKF uses the rate of change of the sun vector measurement to determine the angular body rate of the satellite.

The sun vector is approximated as a fixed vector with respect to the ECI frame and the estimated body rate is therefore also inertially referenced. The expected estimation errors

of this sun RKF are smaller than those of the magnetic RKF. The only drawback of this RKF is the fact that the control methods in Section 5 require orbit referenced body rates. This means that the sun RKF needs to be combined with the Triad algorithm in order to transform angular body rates from the ECI frame to the ORC frame.

4.2.2.1 Sun RKF System Model

The desired state vector is the inertially referenced angular body rate:

$$\mathbf{x}_s = \boldsymbol{\omega}_B^I(t) \tag{4.2.14}$$

where the subscript s designates it as the *sun* determined state vector. The dynamic equation of Section 2.3 can be used directly as the system model:

$$\dot{\mathbf{x}}_s(t) = \dot{\boldsymbol{\omega}}_B^I = \mathbf{I}^{-1}\left(\mathbf{N}_M + \mathbf{N}_{Aero} + \mathbf{N}_{GG} - \mathbf{N}_W - \mathbf{N}_{Gyro}\right) \tag{4.2.15}$$

where $\mathbf{I}^{-1}$ is the inverse moment of inertia matrix as given by (4.2.3).

The continuous time system model can now be presented by:

$$\dot{\mathbf{x}}_s(t) = \mathbf{G}\mathbf{u}_s(t) + \mathbf{s}_s(t) \tag{4.2.16}$$

where $\mathbf{G} = \mathbf{I}^{-1}$, the control torque inputs $\mathbf{u}_s(t) = \mathbf{N}_M(t) + \mathbf{N}_{Aero}(t) - \mathbf{N}_W(t)$ and the disturbance noise $\mathbf{s}_s(t) = \mathbf{I}^{-1}\left(\mathbf{N}_{GG}(t) - \mathbf{N}_{Gyro}(t)\right)$.

The discrete time system model can be presented by:

$$\mathbf{x}_s(k+1) = \boldsymbol{\Phi}\mathbf{x}_s(k) + \boldsymbol{\Gamma}\mathbf{u}_s(k) + \mathbf{s}_s(k) \tag{4.2.17}$$

$$\mathbf{s}_s(k) = \mathbf{N}\left\{\mathbf{0}, \mathbf{Q}(k)\right\} \tag{4.2.18}$$

where $\boldsymbol{\Phi}$ is a 3×3 identity matrix, $\boldsymbol{\Gamma} = (\mathbf{I}^{-1}T_s)$ with T_s defined as the sampling period of the system and $\mathbf{u}_s(k)$ is the discrete time control torque inputs. The system noise model is represented by $\mathbf{s}_s(k)$ and consists of Gaussian noise with a zero mean and a covariance matrix $\mathbf{Q}(k)$.

4.2.2.2 Sun RKF Measurement Model

An assumption is made that the transformation of a measurement vector between time steps can be determined by using a small angle approximation of the transformation matrix given in (2.1.1), if the time step is short enough. This results in a transformation matrix:

$$\Delta\mathbf{A}_s \approx \begin{bmatrix} 1 & \psi & -\theta \\ -\psi & 1 & \phi \\ \theta & -\phi & 1 \end{bmatrix} \tag{4.2.19}$$

Assuming a constant angular rate for the duration of each sample time, the small rotation angles can be estimated as $\phi \approx \omega_{xi}(k)T_s$, $\theta \approx \omega_{yi}(k)T_s$ and $\psi \approx \omega_{zi}(k)T_s$ where $\omega_{xi}(k)$, $\omega_{yi}(k)$ and $\omega_{zi}(k)$ are the vector elements of the ECI body rate vector $\boldsymbol{\omega}_B^I(k)$. From these approximations the transformation matrix now becomes:

$$\begin{aligned}\Delta\mathbf{A}_s &\approx \mathbf{1}_{3\times3} + \Lambda_s\left\{\boldsymbol{\omega}_B^I(k)\right\} \\ &= \mathbf{1}_{3\times3} + \begin{bmatrix} 0 & \omega_{zi}(k)T_s & -\omega_{yi}(k)T_s \\ -\omega_{zi}(k)T_s & 0 & \omega_{xi}(k)T_s \\ \omega_{yi}(k)T_s & -\omega_{xi}(k)T_s & 0 \end{bmatrix}\end{aligned} \tag{4.2.20}$$

where $\mathbf{1}_{3\times3}$ is a 3×3 identity matrix and $\Lambda_s\{\}$ is a matrix function. Using this transformation matrix, the current vector measurement can be predicted from the vector measurement of the previous time step $\mathbf{v}(k-1)$:

$$\mathbf{v}(k) = \Delta\mathbf{A}_s\mathbf{v}(k-1) \tag{4.2.21}$$

The difference between two successive inertially fixed measurements is used to determine the measurement model from (4.2.20) and (4.2.21):

$$\begin{aligned}\mathbf{y}(k) &= \Delta\mathbf{v}(k) \\ &= \mathbf{v}(k) - \mathbf{v}(k-1) \\ &= \Lambda\left\{\boldsymbol{\omega}_B^I(k)\right\}\mathbf{v}(k-1) \\ &= \mathbf{H}(k)\mathbf{x}_s(k) + \mathbf{m}_s(k)\end{aligned} \tag{4.2.22}$$

with

$$\mathbf{H}(k) = \begin{bmatrix} 0 & -v_z(k-1)T_s & v_y(k-1)T_s \\ v_z(k-1)T_s & 0 & -v_x(k-1)T_s \\ -v_y(k-1)T_s & v_x(k-1)T_s & 0 \end{bmatrix} \tag{4.2.23}$$

and

$$\mathbf{m}_s(k) = \mathbf{N}\left\{\mathbf{0}, \mathbf{R}(k)\right\} \tag{4.2.24}$$

where $\mathbf{H}(k)$ is the state output matrix and $\mathbf{m}_s(k)$ is the measurement noise model with a zero mean and a covariance matrix $\mathbf{R}_s(k)$.

4.2.3 Rate Kalman Filter Algorithm

The RKF algorithm consists of five mathematical steps to be implemented at every time interval. The steps are divided into two parts: the time update and the measurement update. During the time update the state vector and the state covariance matrix are propagated to the current time step, based on all previous estimate and measurement information. The subscript $(k+1/k)$ indicates that the variable has been determined

at the current time step $k+1$, but includes only the measurement information up to time step k. During the measurement update the current measurement is incorporated in the estimated state vector and state covariance matrix by means of the RKF gain. The subscript $(k+1/k+1)$ indicates that the current measurement information is also included in the determined variable.

We define the state covariance matrix as:

$$\mathbf{P}_k \triangleq E\left\{\mathbf{x}_k\mathbf{x}_k^T\right\} \tag{4.2.25}$$

where $\mathbf{x}_k$ represents the state vector of the specific RKF being implemented.

4.2.3.1 Time Update

The time update is implemented at every time step, whether measurements are available or not. Steps 1 and 2 describes the propagation of the estimated state vector and the state covariance matrix.

1. Propagation of the state vector using numeric integration of the discrete system model:

$$\hat{\mathbf{x}}_{k+1/k} = \hat{\mathbf{x}}_{k/k} + 0.5T_s\left(3\Delta\mathbf{x}_k - \Delta\mathbf{x}_{k-1}\right) \tag{4.2.26}$$

$$\Delta\mathbf{x}_k = \mathbf{I}^{-1}\left(\mathbf{u}_m(k) - \mathbf{N}_{Gyro}(k)\right) \qquad \text{for Magnetic RKF} \tag{4.2.27}$$

$$\Delta\mathbf{x}_k = \mathbf{I}^{-1}\left(\mathbf{u}_s(k) - \mathbf{N}_{Gyro}(k) + \mathbf{N}_{GG}(k)\right) \qquad \text{for Sun RKF} \tag{4.2.28}$$

2. Propagate the state covariance matrix:

$$\mathbf{P}_{k+1/k} = \mathbf{\Phi}\mathbf{P}_{k/k}\mathbf{\Phi}^T + \mathbf{Q} \tag{4.2.29}$$

where $\mathbf{Q}$ is the system noise covariance matrix and $\mathbf{\Phi}$ is an identity matrix as defined in the discrete system model.

4.2.3.2 Measurement Update

When measurements are available, the time update of the RKF algorithm is followed by these steps:

3. Update the KF gain:

$$\mathbf{K}_{k+1} = \mathbf{P}_{k+1/k}\mathbf{H}_{k+1}^T\left[\mathbf{H}_{k+1}\mathbf{P}_{k+1/k}\mathbf{H}_{k+1}^T + \mathbf{R}\right]^{-1} \tag{4.2.30}$$

where $\mathbf{H}_{k+1}$ can be computed from either (4.2.12) or (4.2.23) depending on whether the magnetic or sun RKF is implemented and $\mathbf{R}$ is the measurement noise covariance matrix.

4. Update the state vector:

$$\hat{\mathbf{x}}_{k+1/k+1} = \hat{\mathbf{x}}_{k+1/k} + \mathbf{K}_{k+1}\left[\mathbf{y}_{k+1} - \mathbf{H}_{k+1}\hat{\mathbf{x}}_{k+1/k}\right] \tag{4.2.31}$$

5. Update the state covariance matrix:

$$\mathbf{P}_{k+1/k+1} = [\mathbf{1}_{3\times3} - \mathbf{K}_{k+1}\mathbf{H}_{k+1}]\,\mathbf{P}_{k+1/k} \tag{4.2.32}$$

where $\mathbf{1}_{3\times3}$ is a 3×3 identity matrix.

4.3 Extended Kalman Filter Estimator

The Extended Kalman Filter is a Kalman Filter that incorporates non-linearities in the system and measurement models by linearising them. The linearisation consists of approximated Taylor expansions (mostly first order) around the point where the desired state vector is equal to the estimated state. The EKF makes use of all available sensor measurements, their corresponding modelled vectors as discussed is Section 3.2 and the statistical description of the measurement and modelling errors to determine the best estimated state vector.

The implemented EKF derives a full state estimate that includes the inertially referenced angular body rate vector and the attitude quaternion vector:

$$\mathbf{x}(t) = \left[\boldsymbol{\omega}_B^{I\,T}(t) \quad \mathbf{q}^T(t)\right]^T \tag{4.3.1}$$

This section describes the system and measurement perturbation models, the computation of the EKF innovation step and the EKF algorithm.

4.3.1 Discrete EKF System Model

The system model can be obtained from the non-linear dynamic and kinematic equations given in (2.3.3) and (2.3.1):

$$\begin{aligned}\dot{\mathbf{x}}(t) &= \mathbf{f}\{\mathbf{x}(t), t\} + \mathbf{s}(t) \\ &= \left[\dot{\boldsymbol{\omega}}_B^{I\,T}(t) \quad \dot{\mathbf{q}}^T(t)\right]^T + \mathbf{s}(t)\end{aligned} \tag{4.3.2}$$

where

$$\mathbf{s}(t) = \mathbf{N}\{\mathbf{0}, \mathbf{Q}(t)\} \tag{4.3.3}$$

is the system noise model consisting of Gaussian noise with a zero mean and a covariance matrix $\mathbf{Q}(t)$.

The EKF also requires a model for the perturbation state vector that is defined as the difference between the true and estimated state:

$$\delta\mathbf{x}(t) \triangleq \mathbf{x}(t) - \hat{\mathbf{x}}(t) \tag{4.3.4}$$

The system model of (4.3.2) can be linearised around the estimated state vector by means of a first order Taylor expansion that results in:

$$\mathbf{f}\left\{\mathbf{x}(t),t\right\} \approx \mathbf{f}\left\{\hat{\mathbf{x}}(t),t\right\} + \left.\frac{\partial \mathbf{f}}{\partial \mathbf{x}}\right|_{\mathbf{x}=\hat{\mathbf{x}}} \delta\mathbf{x}(t) \tag{4.3.5}$$

The linearised perturbation state model can now be obtained from equations (4.3.2) to (4.3.5):

$$\begin{aligned}
\delta\dot{\mathbf{x}}(t) &= \dot{\mathbf{x}}(t) - \dot{\hat{\mathbf{x}}}(t) \\
&= \mathbf{f}\left\{\mathbf{x}(t),t\right\} - \mathbf{f}\left\{\hat{\mathbf{x}}(t),t\right\} \\
&\approx \mathbf{f}\left\{\hat{\mathbf{x}}(t),t\right\} + \left.\frac{\partial \mathbf{f}}{\partial \mathbf{x}}\right|_{\mathbf{x}=\hat{\mathbf{x}}} \delta\mathbf{x}(t) - \mathbf{f}\left\{\hat{\mathbf{x}}(t),t\right\} \\
&= \mathbf{F}\left\{\hat{\mathbf{x}}(t),t\right\}\delta\mathbf{x}(t) + \mathbf{s}(t)
\end{aligned} \tag{4.3.6}$$

where we define

$$\mathbf{F}\left\{\hat{\mathbf{x}}(t),t\right\} \triangleq \left.\frac{\partial \mathbf{f}}{\partial \mathbf{x}}\right|_{\mathbf{x}=\hat{\mathbf{x}}} \tag{4.3.7}$$

as the state perturbation matrix. The derivation of this matrix in terms of the estimated state vector elements is given in Appendix A.1 and makes use of the attitude dynamic and kinematic equations as stated in Section 2.3.

A discrete version of the perturbation state model is required since a discrete EKF will be implemented:

$$\begin{aligned}
\delta\mathbf{x}(k+1) &= e^{\mathbf{F}\{\hat{\mathbf{x}}(t_k),t_k\}T_s}\delta\mathbf{x}(k) \\
&= \mathbf{\Phi}(k)\delta\mathbf{x}(k)
\end{aligned} \tag{4.3.8}$$

where $\mathbf{\Phi}(k)$ is the perturbation state matrix. This matrix can be estimated by a second order Taylor expansion:

$$\mathbf{\Phi}(k) \approx \mathbf{1}_{3\times 3} + \mathbf{F}\left\{\hat{\mathbf{x}}(t_k),t_k\right\}T_s + 0.5\left(\mathbf{F}\left\{\hat{\mathbf{x}}(t_k),t_k\right\}T_s\right)^2 \tag{4.3.9}$$

4.3.2 Discrete EKF Measurement Model

A discrete non-linear measurement model is assumed:

$$\mathbf{y}(k) = \mathbf{h}\left\{\mathbf{x}(t_k),t_k\right\} + \mathbf{m}(k) \tag{4.3.10}$$

$$\mathbf{m}(k) = \mathbf{N}\left\{\mathbf{0},\mathbf{R}(k)\right\} \tag{4.3.11}$$

where $\mathbf{m}(k)$ is the measurement noise model that consists of Gaussian noise with a zero mean and a discrete covariance matrix $\mathbf{R}(k)$.

The measurement model can be linearised around the estimated state vector by means of a first order Taylor expansion:

$$\mathbf{h}\left\{\mathbf{x}(t_k), t_k\right\} \approx \mathbf{h}\left\{\hat{\mathbf{x}}(t_k), t_k\right\} + \left.\frac{\partial \mathbf{h}}{\partial \mathbf{x}}\right|_{\mathbf{x}=\hat{\mathbf{x}}} \delta\mathbf{x}(k) \tag{4.3.12}$$

The EKF requires the linearised perturbation output model, also known as the innovation error model, that can be derived as:

$$\begin{aligned}
\mathbf{e}(k) &= \mathbf{y}(k) - \hat{\mathbf{y}}(k) \\
&= \mathbf{h}\left\{\mathbf{x}(t_k), t_k\right\} - \mathbf{h}\left\{\hat{\mathbf{x}}(t_k), t_k\right\} \\
&\approx \mathbf{h}\left\{\hat{\mathbf{x}}(t_k), t_k\right\} + \left.\frac{\partial \mathbf{h}}{\partial \mathbf{x}}\right|_{\mathbf{x}=\hat{\mathbf{x}}} \delta\mathbf{x}(k) - \mathbf{h}\left\{\hat{\mathbf{x}}(t_k), t_k\right\} \\
&= \mathbf{H}\left\{\hat{\mathbf{x}}(k)\right\} \delta\mathbf{x}(k) + \mathbf{m}(k)
\end{aligned} \tag{4.3.13}$$

where $\mathbf{H}\left\{\hat{\mathbf{x}}(k)\right\}$ is the perturbation output matrix defined as:

$$\mathbf{H}\left\{\hat{\mathbf{x}}(k)\right\} \triangleq \left.\frac{\partial \mathbf{h}}{\partial \mathbf{x}}\right|_{\mathbf{x}=\hat{\mathbf{x}}} \tag{4.3.14}$$

The derivation of the linearised perturbation output matrix $\mathbf{H}\left\{\hat{\mathbf{x}}(k)\right\}$ forms part of the innovation computation of the filter.

4.3.3 Innovation Computation

The innovation is defined as the vector difference between a measured vector $\mathbf{v}_{meas}$ in the SBC frame and its corresponding ORC modelled vector $\mathbf{v}_{model}$ that is transformed to the SBC frame. In the case of an ideal system, no measurement or modelling errors will occur and the normalised measurement vector can be represented in terms of the normalised modelled vector:

$$\bar{\mathbf{v}}_{meas,k}^{ideal} = \mathbf{A}\left\{\mathbf{q}_k\right\} \bar{\mathbf{v}}_{model,k}^{ideal} \tag{4.3.15}$$

where $\mathbf{A}\left\{\mathbf{q}_k\right\}$ is the transformation matrix $\mathbf{A}_{O/B}\left\{\mathbf{q}_k\right\}$ of (2.1.11). The subscript (O/B) is omitted during the rest of this section to simplify the notation.

A more realistic view includes measurement noise $\mathbf{m}_{meas,k}$ and modelling noise $\mathbf{m}_{model,k}$. With the quaternion vector expressed in terms of the estimated quaternion vector $\hat{\mathbf{q}}_k$, (4.3.15) becomes:

$$\bar{\mathbf{v}}_{meas,k} - \mathbf{m}_{meas,k} = \mathbf{A}\left\{\hat{\mathbf{q}}_k + \delta\mathbf{q}\right\}\left(\bar{\mathbf{v}}_{model,k} - \mathbf{m}_{model,k}\right) \tag{4.3.16}$$

where $\delta\mathbf{q} = \mathbf{q}_k - \hat{\mathbf{q}}_k$ represents the perturbation of the quaternion vector. A Taylor expansion is used to linearise the transformation matrix about the point where $\mathbf{q}_k = \hat{\mathbf{q}}_k$ which results in:

$$\mathbf{A}\left\{\mathbf{q}_k\right\} = \mathbf{A}\left\{\hat{\mathbf{q}}_k + \delta\mathbf{q}\right\} \approx \mathbf{A}\left\{\hat{\mathbf{q}}_k\right\} + \sum_{i=1}^{4} \frac{\partial \mathbf{A}\left\{\hat{\mathbf{q}}_k\right\}}{\partial \mathbf{q}_i} \delta\mathbf{q}_{i,k} \tag{4.3.17}$$

The innovation error model of (4.3.13) can now be written as:

$$\begin{aligned}
\mathbf{e}_k &= \bar{\mathbf{v}}_{meas,k} - \mathbf{A}\left\{\hat{\mathbf{q}}_k\right\}\bar{\mathbf{v}}_{model,k} \\
&= \mathbf{A}\left\{\hat{\mathbf{q}}_k + \delta\mathbf{q}\right\}\bar{\mathbf{v}}_{model,k} - \mathbf{A}\left\{\hat{\mathbf{q}}_k\right\}\bar{\mathbf{v}}_{model,k} + \mathbf{m}_k \\
&\approx \left[\mathbf{A}\left\{\hat{\mathbf{q}}_k\right\} + \sum_{i=1}^{4}\frac{\partial\mathbf{A}\left\{\hat{\mathbf{q}}_k\right\}}{\partial\mathbf{q}_i}\delta\mathbf{q}_{i,k}\right]\bar{\mathbf{v}}_{model,k} - \mathbf{A}\left\{\hat{\mathbf{q}}_k\right\}\bar{\mathbf{v}}_{model,k} + \mathbf{m}_k \\
&= \left[\sum_{i=1}^{4}\frac{\partial\mathbf{A}\left\{\hat{\mathbf{q}}_k\right\}}{\partial\mathbf{q}_i}\delta\mathbf{q}_{i,k}\right]\bar{\mathbf{v}}_{model,k} + \mathbf{m}_k \\
&= \begin{bmatrix}\mathbf{h}_1 & \mathbf{h}_2 & \mathbf{h}_3 & \mathbf{h}_4\end{bmatrix}\delta\mathbf{q}_k + \mathbf{m}_k \\
&= \begin{bmatrix}\mathbf{0}_{3\times3} & \mathbf{h}_1 & \mathbf{h}_2 & \mathbf{h}_3 & \mathbf{h}_4\end{bmatrix}\delta\mathbf{x}_k + \mathbf{m}_k \\
&= \mathbf{H}\left\{\hat{\mathbf{q}}_k, \bar{\mathbf{v}}_{model,k}\right\}\delta\mathbf{x}_k + \mathbf{m}_k
\end{aligned} \tag{4.3.18}$$

where

$$\mathbf{h}_i = \frac{\partial\mathbf{A}\left\{\hat{\mathbf{q}}_k\right\}}{\partial\mathbf{q}_i}\bar{\mathbf{v}}_{model,k} \quad \text{for } i = 1,2,3,4 \tag{4.3.19}$$

and the measurement noise can be approximated as

$$\mathbf{m}_k \approx \bar{\mathbf{v}}_{meas,k} - \mathbf{A}\left\{\hat{\mathbf{q}}_k\right\}\mathbf{m}_{model,k} \tag{4.3.20}$$

4.3.4 Extended Kalman Filter Algorithm

The EKF algorithm resembles the KF algorithm to a certain extent, but includes a few changes. The steps are also divided into two parts, namely the time update and the measurement update. The time update propagates the state vector and the perturbation state matrix. During the measurement update the difference between consecutive measurement vectors are not used to update the state vector. The innovation is used instead to determine the vector difference between the measured and modelled vector at the current time step.

The EKF requires the perturbation covariance matrix defined as:

$$\mathbf{P}_k \triangleq E\left\{\delta\mathbf{x}_k\delta\mathbf{x}_k^T\right\} \tag{4.3.21}$$

where $\delta\mathbf{x}_k$ is the perturbation state vector as defined in (4.3.4).

4.3.4.1 Time Update

The time update is implemented at every time step, whether measurements are available or not. The subscript $(k+1/k)$ states that determined variables only used measurement information up to time step k.

1. Propagation of the full state vector using numeric integration of the non-linear dynamic model:

$$\hat{\mathbf{x}}_{k+1/k} = \hat{\mathbf{x}}_{k/k} + \int_{k}^{k+1} \mathbf{f}\left(\hat{\mathbf{x}}_{k/k}, k\right) dt \tag{4.3.22}$$

2. Propagate the state perturbation covariance matrix:

$$\mathbf{P}_{k+1/k} = \mathbf{\Phi}_{k+1/k}\mathbf{P}_{k/k}\mathbf{\Phi}^{T}_{k+1/k} + \mathbf{Q} \tag{4.3.23}$$

where $\mathbf{Q}$ is the system noise covariance matrix and $\mathbf{\Phi}$ is the perturbation state matrix as approximated in (4.3.9).

4.3.4.2 Measurement Update

The time update steps are succeeded by the following steps if valid measurements are available. The measurement update can be executed for each valid measurement and modelled vector pair, usually in the order of least to most accurate measurements. In this way the EKF incorporates all available measurement data. The subscript $(k+1/k+1)$ states that determined variables includes measurement information of time step $k+1$.

3. Update the EKF gain:

$$\mathbf{K}_{k+1} = \mathbf{P}_{k+1/k}\mathbf{H}^{T}_{k+1/k}\left[\mathbf{H}_{k+1/k}\mathbf{P}_{k+1/k}\mathbf{H}^{T}_{k+1/k} + \mathbf{R}\right]^{-1} \tag{4.3.24}$$

where $\mathbf{H}_{k+1/k}$ is the perturbation state output matrix linearised about the propagated state vector and $\mathbf{R}$ is the noise covariance matrix of the used measurement.

4. Determine the innovation:

$$\mathbf{e}_{k+1} = \bar{\mathbf{v}}_{meas,k+1} - \hat{\mathbf{v}}_{body,k+1/k} \tag{4.3.25}$$

$$= \bar{\mathbf{v}}_{meas,k+1} - \hat{\mathbf{A}}_{k+1/k}\hat{\mathbf{v}}_{model,k+1} \tag{4.3.26}$$

where $\hat{\mathbf{A}}_{k+1/k}$ is the transformation matrix $\mathbf{A}_{O/B}$ evaluated at the propagated quaternion vector from (4.3.22).

5. Update the state perturbation vector:

$$\delta\mathbf{x}_{k+1} = \mathbf{K}_{k+1}\mathbf{e}_{k+1} \tag{4.3.27}$$

6. Update the state vector:

$$\hat{\mathbf{x}}_{k+1/k+1} = \hat{\mathbf{x}}_{k+1/k} + \delta\mathbf{x}_{k+1} \tag{4.3.28}$$

In this step the updated quaternion vector is also normalised to ensure that the quaternion constraint stays valid:

$$\hat{\mathbf{q}}_{k+1/k+1} = \hat{\mathbf{q}}_{k+1/k+1} / \left\|\hat{\mathbf{q}}_{k+1/k+1}\right\| \tag{4.3.29}$$

7. Update the state perturbation covariance matrix:

$$\mathbf{P}_{k+1/k+1} = \left[\mathbf{1}_{7\times7} - \mathbf{K}_{k+1}\mathbf{H}_{k+1/k+1}\right]\mathbf{P}_{k+1/k}\left[\mathbf{1}_{7\times7} - \mathbf{K}_{k+1}\mathbf{H}_{k+1/k+1}\right]^T + \mathbf{K}_{k+1}\mathbf{R}\mathbf{K}_{k+1}^T \quad (4.3.30)$$

4.4 Simulation Results

The implementation of all the estimation methods were evaluated in the simulation environment described in Chapter 3. The algorithms were evaluated by means of two simulation sets with different initial conditions. For the first set, a high initial orbit reference angular body rate vector is assumed and the initial attitude angles are zero. The second set assumes a stabilised satellite with zero initial angular body rates, but non-zero initial attitude angles. The information of the different sets are summarised in Table 4.1.

Table 4.1: Initial conditions of simulation sets.

Set name	Angular rate $\boldsymbol{\omega}_B^O$ $(^\circ/s)$	Roll, Pitch, Yaw $(^\circ)$
Tumbling	$[1.4, -5, -1.4]^T$	$[0, 0, 0]$
Stabilised	$[0, 0, 0]^T$	$[30, 20, -20]$

In the simulation the different models discussed in Section 3.2 are used to determine orbit referenced, modelled versions of the expected measurement vectors, namely the sun vector, the nadir vector and the geomagnetic field vector. These modelled vectors are converted to the SBC frame and noise is added to them in order to generate "realistic" measurement vectors with measurement errors. These measurements are then used as real sensor measurements in the estimation algorithms of the simulation.

The noise that is added to the modelled vector is normal distributed noise with a zero mean, constructed from a random number generator. The maximum measurement error of each sensor is listed in Table 4.2. These values were used as the 3σ values of the noise distribution, therefore 99.73% of the errors will fall within the maximum error bound. The maximum effect of the errors on the measurement unit vector components are also shown in Table 4.2.

The results of each described estimation method for the two simulation sets are shown below. In some figures there are shaded areas. These areas represent the intervals when neither of the sun nor nadir measurements are valid. The red rectangular wave on the bottom of these figures is the sun/eclipse (S/E) signal. The rising edge of the signal represents the change of the satellite to the sunlit part of the orbit and the falling edge

Table 4.2: Maximum sensor measurement errors [11, 12].

Sensor	Error (3σ)	Unit vector error
Magnetometer	12 nT	0.00035 units
Sun Sensor	0.4°	0.007 units
Nadir Sensor	0.2°	0.0035 units

the transfer back to eclipse. From these simulation results conclusions are drawn regarding which method is best suited to specific attitude situations.

4.4.1 Triad Algorithm

The Triad algorithm can only be implemented in the sunlit part of the orbit, during periods where both the sun and nadir measurements are valid. The periods of invalid measurements are represented by shaded areas on the simulation figures. An Euler representation of the attitude angles is used delivering roll ϕ, pitch θ and yaw ψ angles.

In Figure 4.1 the estimated attitude angles are compared to the real angles during the tumbling set simulation. Estimated values are unavailable for long periods during the sunlit part of the orbit when both the nadir and sun measurements are not valid simultaneously, but they follow the real values very closely when they are available.

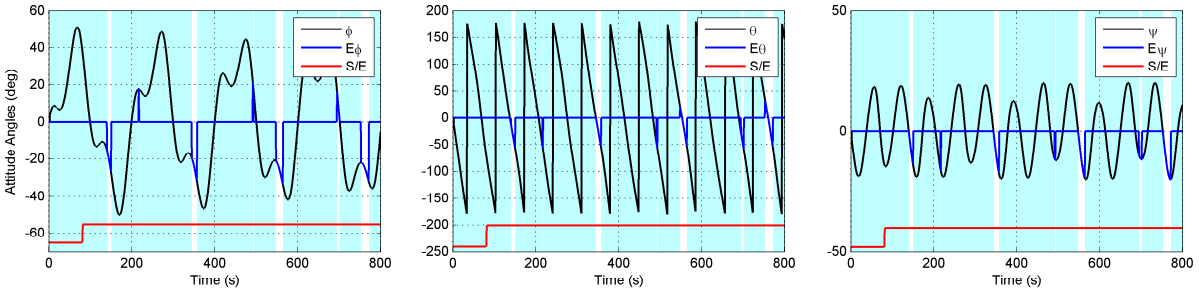

(a) Roll (b) Pitch (c) Yaw

Figure 4.1: Triad estimated attitude angles with tumbling set. The shaded intervals represent invalid nadir and fine sun sensor measurements and the red rectangular wave form S/E is the sun/eclipse signal.

Figure 4.2 shows the estimated attitude angles for the stabilised set simulation. Valid nadir and sun measurements are available for the larger portion of the sunlit part of the orbit and the estimation errors seem to be small.

The estimation errors of the two simulation sets over the first 10 000 seconds are shown in Figure 4.3. It is clear that all errors fall within a margin of ± 0.7 degrees. However,

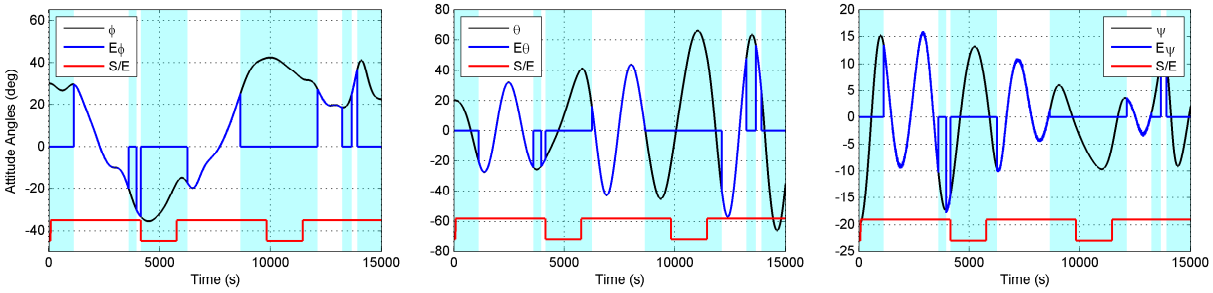

(a) Roll (b) Pitch (c) Yaw

Figure 4.2: Triad estimated attitude angles with stabilised set.

the majority of the error values, for both simulations, fall within the $\pm 0.4^\circ$ bound. This bound relates to the noise added to the sun and nadir measurements as stated in Table 4.2. The Triad algorithm therefore provides accurate attitude estimates within $\pm 0.7^\circ$ whenever valid measurements are available. When the satellite is tumbling, these valid measurement periods are very short and will not be sufficient for control means.

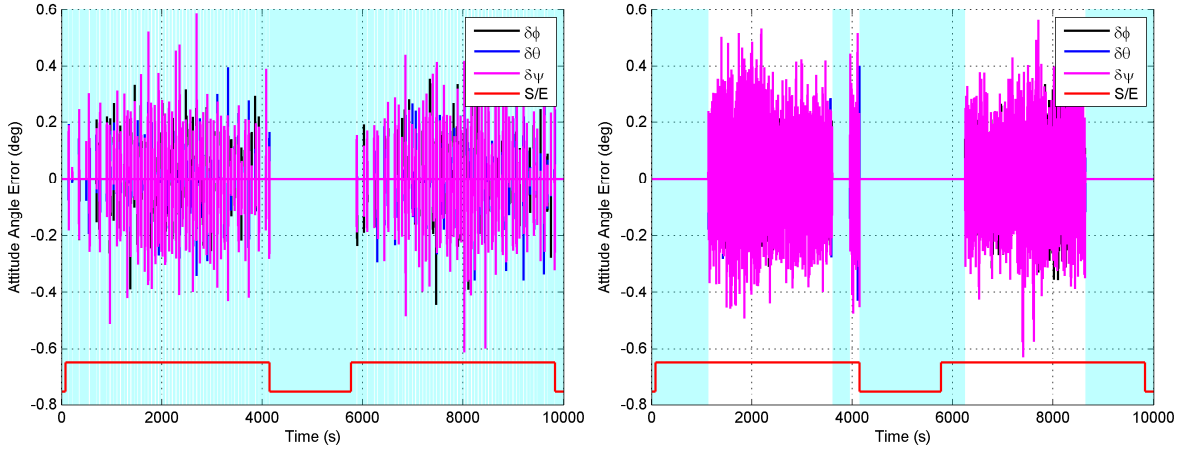

(a) Tumbling set (b) Stabilised set

Figure 4.3: Triad estimated attitude angle error.

4.4.2 Magnetic Rate Kalman Filter

This filter produces orbit referenced angular body rates during the entire orbit. If, for instance, the sampling period of the magnetometer is every ten seconds and the sample period of the magnetic RKF is every second, the RKF will propagate the estimated state until a measurement is available. In these simulations the magnetic RKF is executed every second and measurements are also available at 1 second intervals.

Figure 4.4 shows the results of the magnetic RKF implemented on the tumbling set simulation. The RKF converges within 400 seconds and then follows the trend of the true rates. The results of the stabilised set are shown in Figure 4.5. Since the true angular rates are low, it is easier to see the errors made by the estimator.

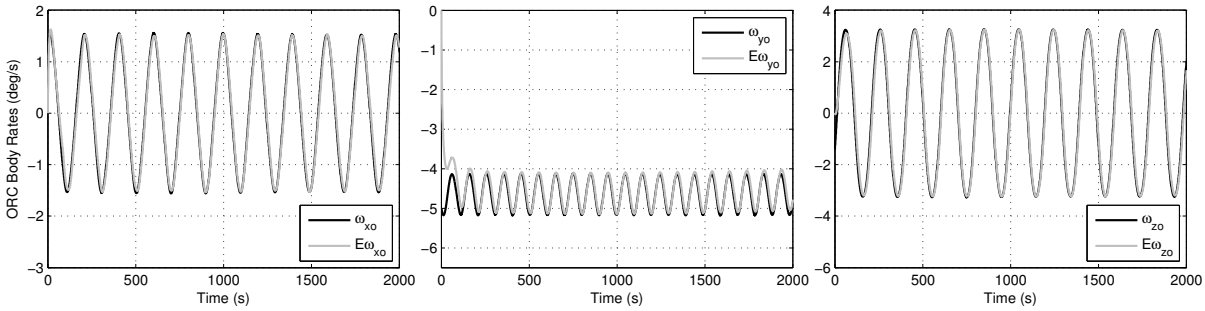

(a) Roll rate (b) Pitch rate (c) Yaw rate

Figure 4.4: Magnetic RKF estimated ORC body rates with tumbling set.

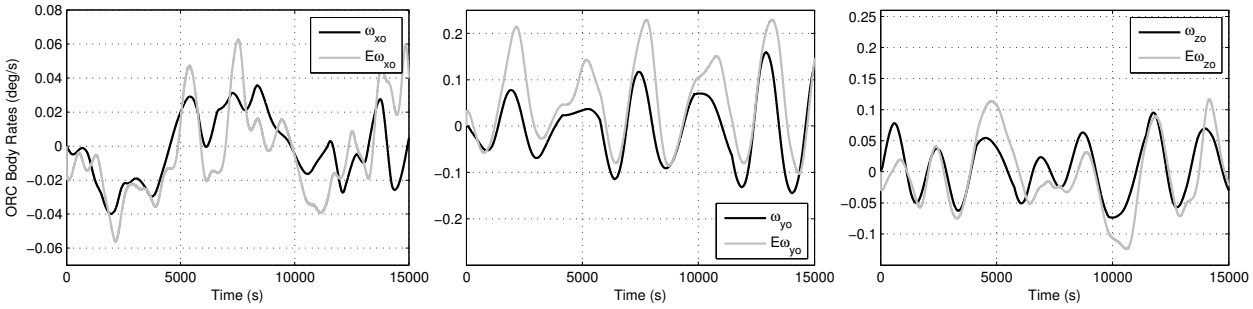

(a) Roll rate (b) Pitch rate (c) Yaw rate

Figure 4.5: Magnetic RKF estimated ORC body rates with stabilised set.

From Figure 4.6 it can be seen that the tumbling set comprise of larger estimation errors than the stabilised set, especially in terms of the yaw rate which fluctuates between ± 0.3 degrees per second. These larger errors can be contributed to the modelling of the aerodynamic disturbance torque with the system noise, instead of using a separate model to characterise it. When the satellite is tumbling, the induced aerodynamic torque can increase and decrease as the surface area of the feathers perpendicular to the velocity vector increases or decreases. This change in disturbance torque can be the cause of the larger estimation errors as shown in Figure 4.6(a). When the satellite is stabilised, the surface area of the feathers perpendicular to the flow stays small and thus the effect of the aerodynamic disturbance torque is small. The estimation errors seen in Figure 4.6(b) is mainly as a result of the expected average error with a magnitude of the orbital rate ω_o, due to the geomagnetic field vector that is not inertially fixed.

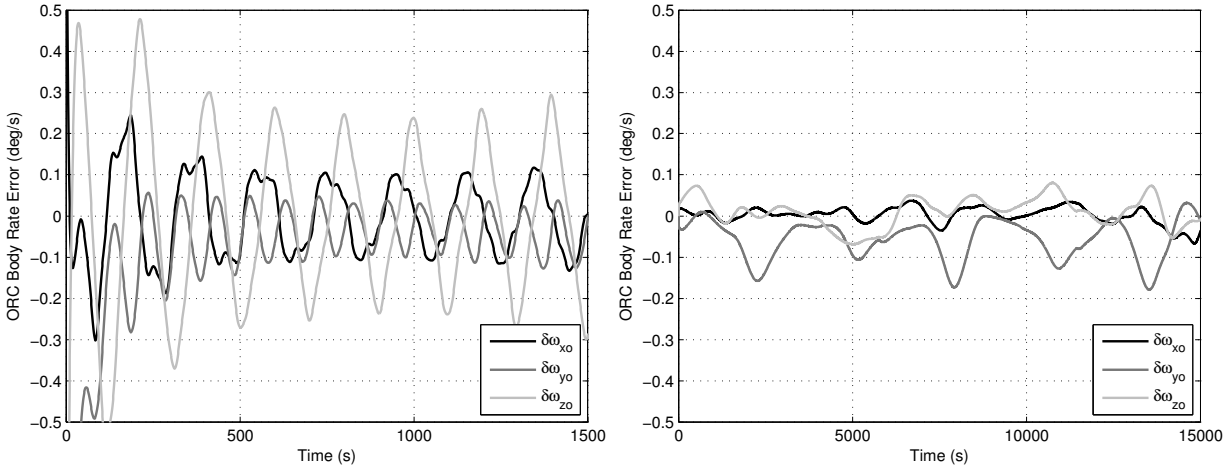

(a) Tumbling set (b) Stabilised set

Figure 4.6: Magnetic RKF estimated ORC body rate error.

4.4.3 Sun Rate Kalman Filter

The sun RKF produces an inertially referenced angular body rate vector during the entire orbit period. The required angular body rate vector for the control methods must however be orbit referenced. The Triad algorithm is combined with the sun RKF to supply an ORC angular body rate vector, but only during the sunlit part of the orbit when valid measurements are available. The invalid measurement periods are represented by the shaded areas in the simulation results.

The sun RKF includes the modelled aerodynamic control and gravity gradient torques which increases the computations needed to perform this algorithm compared to the magnetic KF. The filter is executed every second and measurements are also taken at 1 second intervals. Whether these measurements are valid depends on the satellite attitude and the position of the satellite along the orbital path.

In Figure 4.7 the estimated ECI body rates for the tumbling set are shown. The sun RKF requires more than half an orbit to converge to the true values. Due to the short valid measurement periods, the estimator must propagate only for many time steps and therefore the estimator never follows the true rates completely. The results of the sun RKF when using the stabilised set is shown in Figure 4.8. Here we see that during the shaded invalid measurement periods the estimator makes noticeable errors. When measurements are available for a longer period, the sun RKF follows the true values within a shorter time period of 1 000 seconds or less.

The estimation errors of the sun RKF for both the simulation sets are shown in Figure 4.9. The tumbling set errors are large compared to the errors of the magnetic RKF for the same set. This is largely the result of the very short valid measurement update periods

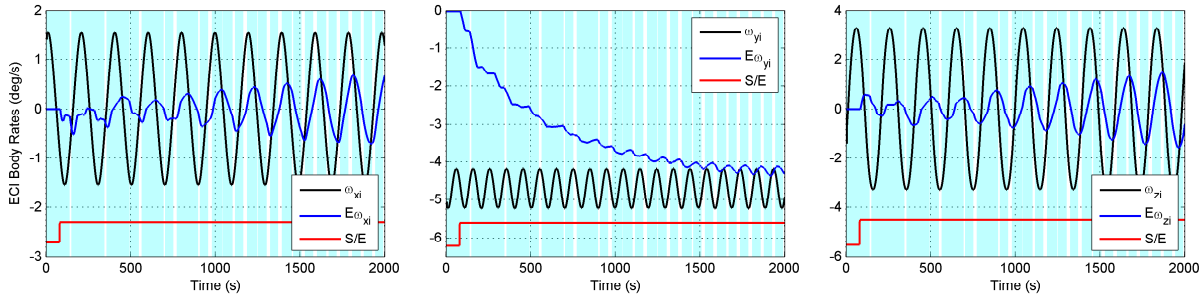

(a) Roll rate (b) Pitch rate (c) Yaw rate

Figure 4.7: Sun RKF estimated ECI body rates with tumbling set.

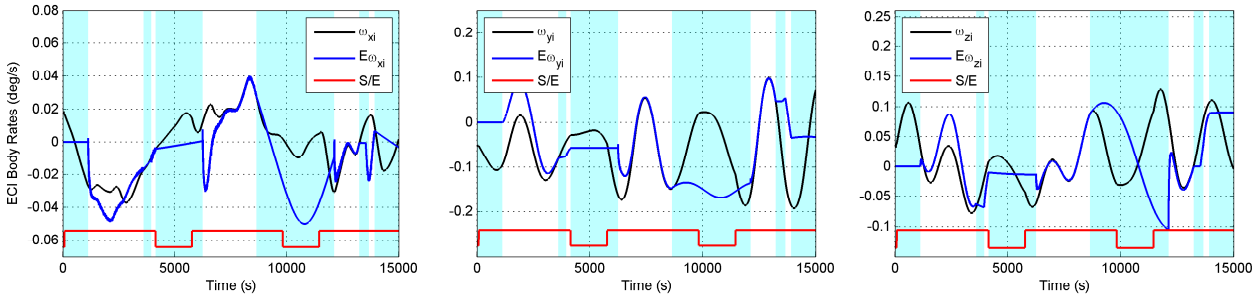

(a) Roll rate (b) Pitch rate (c) Yaw rate

Figure 4.8: Sun RKF estimated ECI body rates with stabilised set.

of the sun RKF. Figure 4.9(a) stretches over more than an orbit period and this error trend is repeated for each orbit with the errors increasing during eclipse. The estimation errors of the stabilised set is shown in Figure 4.9(b). From the second sunlit part of the simulation orbit, within the valid measurements period, the estimation errors are smaller than ±5 milli-degrees per second within 1 000 seconds. The errors increase during eclipse, but this will not be a problem since only the estimated values during the valid measurement periods will be used in collaboration with the Triad algorithm to produce an orbit referenced body rate vector.

The estimation error of the ORC angular body rate vector produced from the combination of the sun RKF and the Triad algorithm is presented in Figure 4.10. A short interval of the tumbling set simulation is shown, but these errors are large during the total duration of the simulation. These large errors are inherited from the large errors of the ECI angular body rate vector of Figure 4.7. The sun RKF and Triad algorithm combination is therefore less sufficient than the magnetic RKF during periods where the satellite experience high tumbling rates. The ORC body rate vector estimation errors mirror the results of the estimated ECI body rate vector for the stabilised set. The errors settle within 1 000 seconds of the valid measurement periods to values below ±5 milli-degrees per

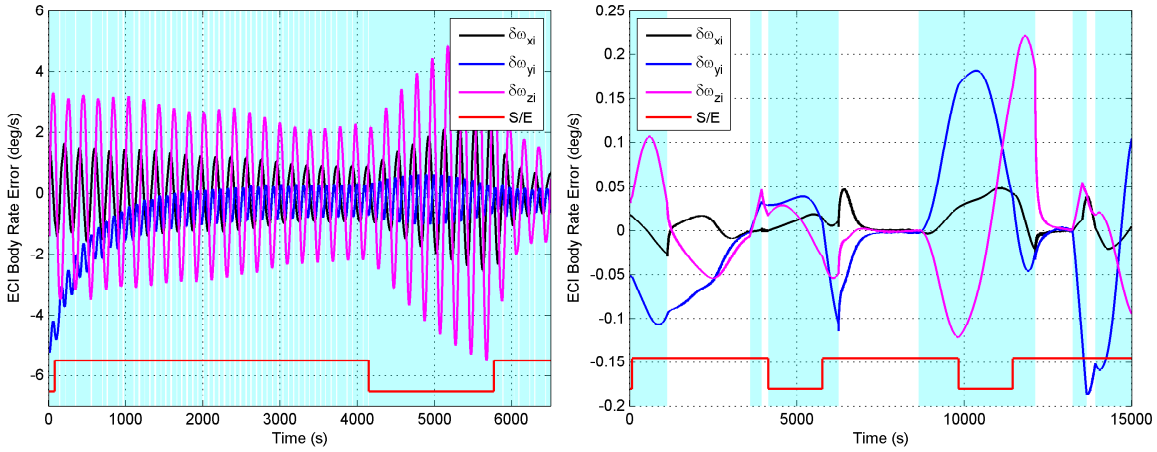

(a) Tumbling set (b) Stabilised set

Figure 4.9: Sun RKF estimated ECI body rate error.

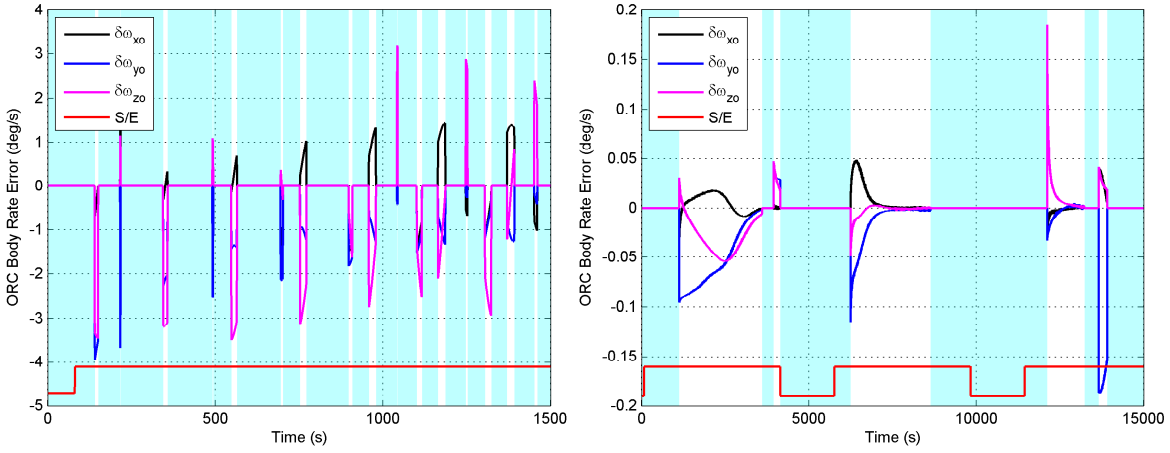

(a) Tumbling set (b) Stabilised set

Figure 4.10: Sun RKF estimated ORC body rate error.

second. This is visible from the second sunlit period that lasts longer than 1 000 seconds. The sun RKF is therefore a better estimator than the magnetic RKF to use when the satellite experiences low angular rates.

4.4.4 Extended Kalman Filter

The EKF produces the estimated ECI angular body rate vector and attitude quaternion vector for the full duration of each orbit period. From these vectors the ORC angular body rate vector is estimated. This filter makes use of all measurements that are available and is executed every second. All measurements are sampled at a frequency of 1 Hz. The computations needed for the execution of the EKF is more than that of the sun or magnetic

RKF due to the linearisation of the system and measurement models and the inclusion of all available measurements. The EKF also includes the modelled aerodynamic control and gravity gradient torques in its system model, like the sun RKF.

Figure 4.11 shows the estimated ORC body rate vector compared to the true vector for the tumbling simulation set. The filter requires less than 500 seconds to lock onto the true vector values. In Figure 4.12 the estimated ORC body rates determined for the stabilised simulation set are shown. During the non-shaded periods the estimated values follow the true values apart from the small amounts of measurement noise especially visible in Figure 4.12(a). The errors during the shaded intervals are larger due to the fact that only the magnetometer measurement is available.

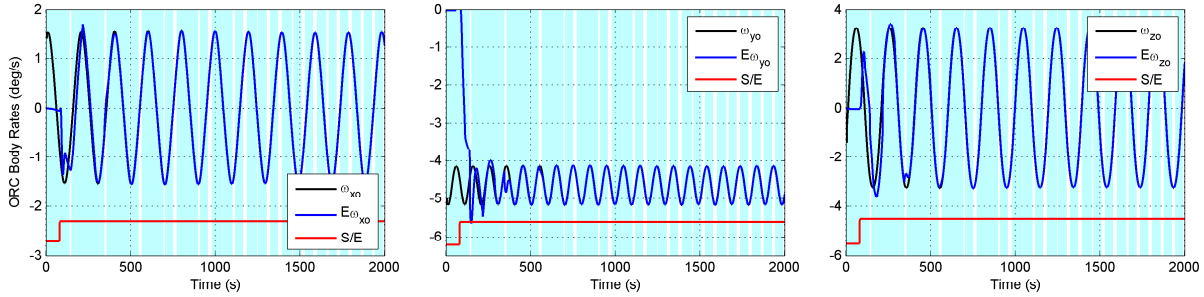

(a) Roll rate (b) Pitch rate (c) Yaw rate

Figure 4.11: EKF estimated ORC body rates with tumbling set.

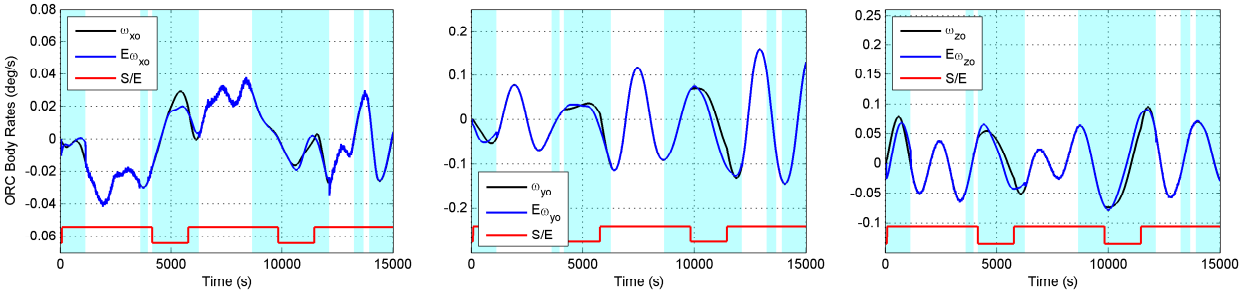

(a) Roll rate (b) Pitch rate (c) Yaw rate

Figure 4.12: EKF estimated ORC body rates with stabilised set.

The estimation errors of the tumbling set shown in Figure 4.13(a) are smaller than the errors of the magnetic RKF for the same set and fluctuates between ± 0.1 degrees per second. This improvement can be attributed to the more accurate system model and the incorporation of the sun and nadir measurements. The estimation errors of the stabilised set are shown in Figure 4.13(b). In the shaded areas only one of the three measurements is available, namely the geomagnetic field vector. The errors are still smaller when compared

to the corresponding magnetic RKF results. The estimation errors are within a ±5 milli-degrees per second bound within 50 seconds after entering the non-shaded intervals. The settling time of the EKF to errors within this bound is therefore faster than the settling time of the sun RKF.

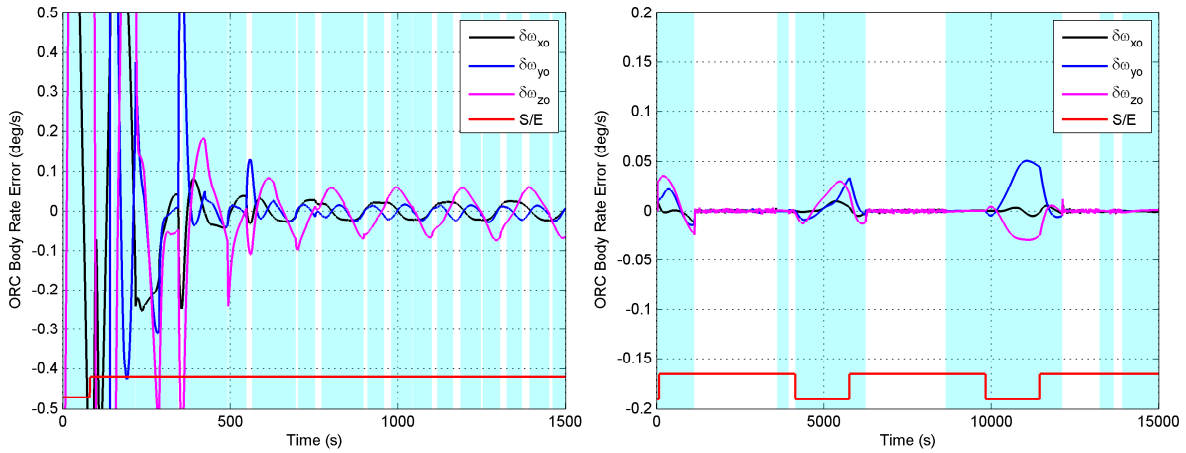

(a) Tumbling set (b) Stabilised set

Figure 4.13: EKF estimated ORC body rate error.

The estimated attitude for the two simulation sets, expressed as Euler roll, pitch and yaw angles, are shown in Figures 4.14 and 4.15. The estimator follows the true attitude closely after 600 seconds in the case of the tumbling set. It can also be seen from the

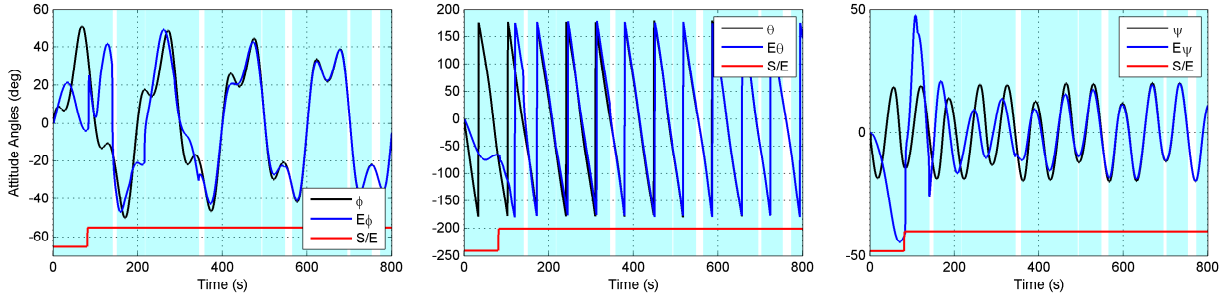

(a) Roll (b) Pitch (c) Yaw

Figure 4.14: EKF estimated attitude angles with tumbling set.

estimated attitude error shown in Figure 4.16(a) that during the intervals where the sun and nadir measurements are available, the errors decrease. The attitude estimation errors of the stabilised set are shown in Figure 4.16(b). The true attitude is followed closely in the non-shaded areas, while errors during the shaded areas can reach values up to 10°.

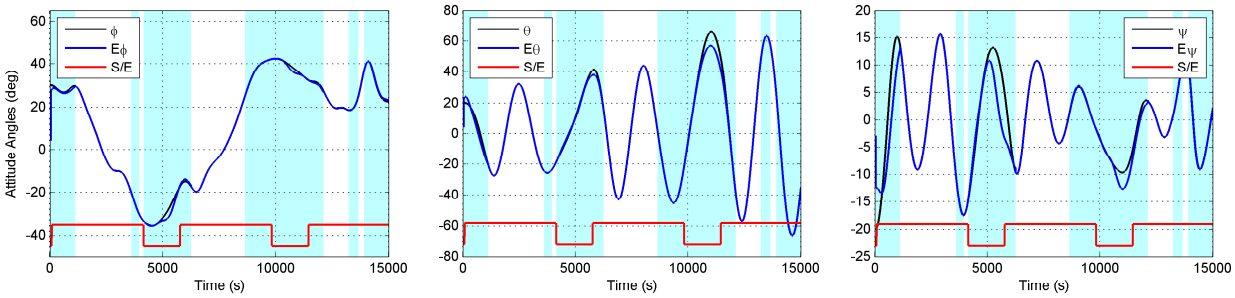

(a) Roll (b) Pitch (c) Yaw

Figure 4.15: EKF estimated attitude angles with stabilised set.

The errors during valid measurement periods fall within a $\pm 0.2^\circ$ bound. It therefore stays within half of the Triad algorithm bound.

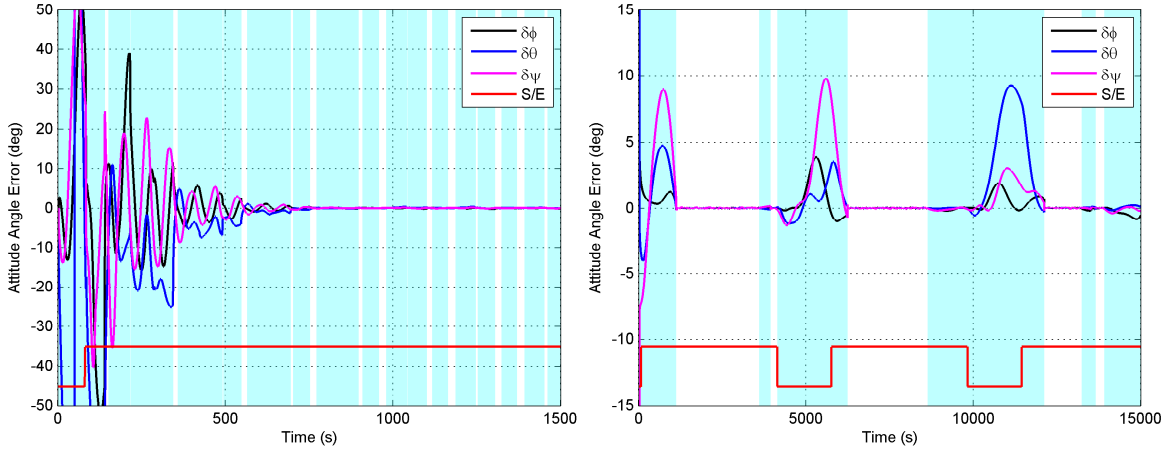

(a) Tumbling set (b) Stabilised set

Figure 4.16: EKF estimated attitude angle error.

4.5 Summary

It is necessary to determine the orientation and rotational velocity of a spacecraft before control can be applied. Using the measurements gathered from the sensors of the satellite, sometimes in combination with the matching modelled measurement vectors, these desired quantities can be calculated.

In this chapter three attitude determination algorithms were discussed and evaluated. These include the Triad, Rate Kalman Filter and Extended Kalman Filter algorithms. The desired vectors are the ORC angular body rate vector and the attitude quaternion vector. The Triad algorithm only determines the attitude vector. Two versions of the

RKF were implemented. The magnetic RKF is used to determine the ORC angular body rate vector. With the sun RKF the ECI angular body rate is computed. The EKF determines both the ECI angular body rate vector and the attitude vector. These two vectors are used to determine the ORC angular body rate vector.

The determination methods were evaluated by means of two simulations with defined initial value sets. The tumbling set was used to represent a tumbling satellite (a satellite with uncontrolled high angular body rates). The stabilised set represented a satellite with low angular body rates and an initial attitude that can be expected of such a satellite.

In terms of the estimated ORC angular body rate vector for the tumbling set, the EKF ensured a 66% improvement with respect to the magnetic RKF results. However, if the satellite is tumbling, the available electrical power will be limited. It is therefore more favourable to use the magnetic RKF because it requires less computations than the EKF. The sun RKF was combined with the Triad algorithm to provide the ORC angular body rate vector. Due to the short periods where both the sun and nadir measurements were valid, the sun RKF and Triad algorithm combination performed poorly with estimation errors up to ± 4 degrees per second. The ORC vector is needed for the detumbling controller discussed in Section 5.1 to lower and control the angular body rates of the satellite.

When the satellite experiences low angular rates, the estimated ORC angular body rate vector and the estimated attitude vector are required for control. The control will mainly be needed to achieve three-axis stabilisation and for imaging during the sunlit part of the orbit. Concentrating on the sunlit part of the orbit that coincides with valid nadir and sun measurement periods, the following conclusions are drawn regarding the estimation methods:

- The sun RKF performs better than the magnetic RKF by stabilising at an ORC angular body rate error within a ± 0.005 degrees per second margin.
- The ORC angular body rate vector of the EKF also settles within a ± 0.005 bound, but within a twenty times shorter settling time than the sun RKF.
- The attitude vector estimation error bound of the Triad algorithm is twice the magnitude of the estimation error bound of the EKF.
- In terms of accuracy, the EKF is the superior determination method.
- The computational simplicity of the Triad algorithm and the sun RKF is a valuable attribute that must be considered. These methods do not necessarily provide poor estimates, but rather estimates that are not as good as the EKF estimates.

The simulation results are used to decide which determination methods to use in this project. During tumbling periods of the satellite, the magnetic RKF will be used to compute the estimated ORC angular body rate of the satellite. When the satellite is stabilised with low angular rates, the Triad algorithm in collaboration with the sun RKF will be used to determine the ORC body angular rate vector and the attitude vector during the valid measurement periods. The satellite will therefore only be controlled during valid measurement periods. The EKF provides more accurate estimates, but it requires much more computational effort from the on-board computer than the other methods. It is therefore decided that this method will not be required for this project.

Chapter 5

Control Methods

The satellite's lifetime may consist of various stages and each of these stages may require different means of control depending on their different specifications. Three control modes are identified for this satellite project, namely detumbling, three-axis stabilisation and pointing control.

The detumbling control mode is needed at the start of the satellite's lifetime. After the satellite is ejected from the P-POD and all mechanical parts have been deployed, the satellite may experience high tumbling rates. These rates need to be lowered and controlled to end the varying tumbling motion of the satellite. The B-dot and Y-spin controller, as presented by [37], is discussed.

The three-axis stabilisation control mode follows the detumbling control mode. After the tumbling rates of the satellite are reduced and under control, the next step is to control the attitude of the satellite as close as possible to a certain desired orientation. The desired orientation for this project is zero roll, pitch and yaw angles. This means that the axes of the SBC frame must align with the axes of the ORC frame. Two possible control methods are discussed. The first is the compass-like proportional-integral-derivative (PID) controller presented by Psiaki [8]. This controller uses magnetic torques to control the roll angle of the satellite and to damp the passive aerodynamic pitch and yaw control torques. The aerodynamic and cross-product control law is the second control method. This method makes use of aerodynamic roll paddles to control the roll angle of the satellite. A magnetic attitude controller, similar to the controller of [21], damps the aerodynamic control torques generated by the satellite's feathers and supports the paddle controller with roll control.

The pointing control mode is needed during imaging intervals. The camera payload must be pointed in a specific direction with a pointing accuracy below 1° RMS. Reaction wheels are added to the ADCS system to reach this specification. Three control methods are

considered, namely the aerodynamic and cross-product control law with a Y-momentum bias, the pitch axis control law and the quaternion feedback control law.

The three control modes, together with their possible control methods, are discussed and evaluated in this chapter. The simulation results of these control methods are shown and are used to identify the best control method for each control mode.

A hardware-in-the-loop simulation is also conducted with the on-board computer (OBC) designed by Botma [13]. The control algorithms of the detumbling control mode are implemented on the OBC, together with the required models and determination method. This test is used to see if the OBC executes these algorithms correctly and to determine the computation time needed per control loop.

5.1 Detumbling Control

The satellite will be ejected from a P-POD and all the mechanical parts deployed. These parts include all four aerodynamic feathers, two aerodynamic roll paddles and the magnetometer. The satellite may experience high tumbling rates due to these mechanical deployments, the ejection from the P-POD and the possibility of unknown disturbances. A controller is needed to lower these rates to manageable values. The detumbling controller as presented by [37] will be the only control method considered. This method consists of a simple B-dot and Y-spin controller.

A B-dot magnetic controller can be used to damp the angular rates about the X_B- and Z_B-axis. Its characteristic equation is shown in (5.1.1). This controller requires no estimated states, but relies greatly on the geomagnetic field vector measurement. The principle of the controller is to minimise the rate of change in the angle β between the positive Y_B-axis and the local geomagnetic field vector.

As the roll and yaw body rates are damped, the satellite's angular rate vector moves closer to the orbit normal direction. The Y-spin controller expressed in (5.1.2) can be used to control the angular spin rate about the Y_B-axis. The controller makes use of the difference between the reference pitch rate $\omega_{y(ref)}$ and the estimated pitch rate $\hat{\omega}_y$ supplied by the magnetic RKF. An optimal approach is applied where only the magnetic torque rod that will result in the largest control torque is used.

These two controllers are described by

$$M_y = -K_d\dot{\beta} \quad \text{where } \beta = \arctan\left(\frac{B_y}{\sqrt{B_x^2 + B_z^2}}\right) \tag{5.1.1}$$

and

$$M_x = K_s(\hat{\omega}_y - \omega_{y(ref)})\text{sgn}(B_z) \text{ for } |B_z| > |B_x|$$
$$M_z = K_s(\omega_{y(ref)} - \hat{\omega}_y)\text{sgn}(B_x) \text{ for } |B_x| > |B_z| \quad (5.1.2)$$

where K_d and K_s are the detumbling and spin controller gains, M_x, M_y and M_z are the required magnetic moments to be generated by the magnetic torque rods and B_x, B_y and B_z are the components of the measured geomagnetic field vector.

5.2 Three-axis Stabilisation

Three-axis stabilisation means controlling the satellite's attitude as close as possible to a certain desired orientation. A zero roll, pitch and yaw attitude is the desired orientation for this project. A further requirement is that the satellite is stabilised within a $\pm 5^\circ$ error margin from this desired orientation.

Two possible aerodynamic control methods are considered in this section, namely the compass-like PID controller and the aerodynamic and cross-product control law. The satellite structure as discussed in Section 2.2 forms a crucial part of the both these control methods.

5.2.1 Compass-like Proportional-Integral-Derivative Control

This control method makes use of the passive pitch-yaw aerodynamic control torque and a magnetic controller, namely the compass-like PID control law. This control law is a modified version of the compass control law [38] and was proposed by Mark L. Psiaki [8] in 2004 for the aerodynamic feather stabilisation design.

The compass control law is shown in (5.2.1). The desired magnetic field unit vector $\bar{\mathbf{B}}_{des}$ is approximated as the modelled ORC geomagnetic field vector and $\bar{\mathbf{B}}$ is the measured geomagnetic field vector. When the SBC frame is aligned with the ORC frame the derivative term will become zero and the required magnetic moment $\mathbf{M}$ will be aligned with the local geomagnetic field, thus resulting in zero torque. The torque rods are therefore wasting energy.

$$\mathbf{M} = K_P \left(\dot{\bar{\mathbf{B}}}_{des} + \tau_1 \left(\dot{\bar{\mathbf{B}}}_{des} - \dot{\bar{\mathbf{B}}} \right) \right) \quad (5.2.1)$$

Psiaki modified the compass control law and produced the final form of (5.2.2). The first modification eliminates the unnecessary generation of a magnetic moment when the satellite is aligned with the ORC frame. A projection matrix $\left(\mathbf{1} - \bar{\mathbf{B}}\bar{\mathbf{B}}^T\right)$ is used to

ensure that the generated magnetic moment will always be perpendicular to the local geomagnetic field vector.

$$\mathbf{M} = \left(\mathbf{A}_{aero}^{T}[i_p, i_y] \left[\left(\mathbf{1} - \bar{\mathbf{B}}\bar{\mathbf{B}}^{T}\right) \left\{ K_P \left(\bar{\mathbf{B}}_{des} + \bar{\mathbf{B}} \times \begin{bmatrix} i_r \\ 0 \\ 0 \end{bmatrix} \right) + K_D \left(\dot{\bar{\mathbf{B}}}_{des} - \dot{\bar{\mathbf{B}}} \right) \right\} \right] \right) \tag{5.2.2}$$

The second modification is to include integral control in the form of error integrals defined as:

$$\begin{bmatrix} i_r\,(t) \\ i_p\,(t) \\ i_y\,(t) \end{bmatrix} = K_I \int^{i} \left(\bar{\mathbf{B}}_{des}(\tau) \times \bar{\mathbf{B}}(\tau) \right) d\tau \tag{5.2.3}$$

where K_I is the integral gain and τ is a dummy integration variable. The roll error integral i_r is incorporated directly in (5.2.2) to counteract steady-state roll disturbance torques. The pitch and yaw error integrals i_p and i_y are used to turn off magnetic feedback about the pitch and yaw axis when the satellite is at a steady-state position. They are incorporated by means of a transformation matrix $\mathbf{A}_{aero}$ defined as:

$$\mathbf{A}_{aero}\left[i_p\,(t)\,, i_y\,(t)\right] = \mathbf{A} \left\{ \frac{1}{\sqrt{1 + \left[i_p^2\,(t) + i_y^2\,(t)\right]/4}} \begin{bmatrix} 0 \\ i_p\,(t)/2 \\ i_y\,(t)/2 \\ 1 \end{bmatrix} \right\} \tag{5.2.4}$$

that transforms vectors from the SBC frame to an aerodynamic coordinate frame. The vector $\bar{\mathbf{B}}$ in (5.2.2) and (5.2.3) represents the SBC measured geomagnetic field vector $\bar{\mathbf{B}}_{meas}$ that is transformed to the aerodynamic coordinate system:

$$\bar{\mathbf{B}} = \mathbf{A}_{aero}\left[i_p, i_y\right] \bar{\mathbf{B}}_{meas} \tag{5.2.5}$$

$$\dot{\bar{\mathbf{B}}} = \mathbf{A}_{aero}\left[i_p, i_y\right] \dot{\bar{\mathbf{B}}}_{meas} \tag{5.2.6}$$

The controller gains are defined as:

$$K_P = \frac{\mathbf{I}_{mavg}}{\tau_1 \tau_2 \left\|\mathbf{B}\right\|} \tag{5.2.7}$$

$$K_I = \frac{1}{\tau_0} \tag{5.2.8}$$

$$K_D = \frac{\mathbf{I}_{mavg}}{\tau_2 \left\|\mathbf{B}\right\|} \tag{5.2.9}$$

where $\mathbf{I}_{mavg}$ is the average of the principle moments of inertia of the satellite, $\|\mathbf{B}\|$ is the norm of the measured geomagnetic field vector and τ_0, τ_1 and τ_2 are the controller tuning parameters.

This control method, when implemented, starts with the computation of (5.2.4) to (5.2.6), followed by (5.2.3) and is concluded by (5.2.2). This control method requires no estimated states and can be implemented during the entire orbit period. It uses magnetic torques to stabilise the roll angle and to damp the passively controlled aerodynamic pitch-yaw system.

5.2.2 Aerodynamic and Cross-product Control Law

The aerodynamic and cross-product control law (from this point onward referred to as the XProd control law) incorporates the passive pitch-yaw aerodynamic control [8], as well as active aerodynamic roll control by means of two aerodynamic roll control paddles. A cross-product magnetic controller is also utilised to support the paddle controller and to damp the aerodynamic pitch-yaw stabilisation system.

The roll paddles are turned in opposite directions to generate the needed roll control torque. The maximum angle that the paddles may turn away from their normal positions is $\pm 30°$. This constraint is added to prevent the roll paddles from blocking too large an area of the FOV of the sun and nadir sensors.

For the relationship between the needed roll control torque N_x and the resulting rotation angle θ_{pad} of the positive Z_B-axis, the paddle is modelled using the aerodynamic torque model of Section 3.2. It is assumed that the atmospheric velocity vector consists only of the negative orbital velocity vector, therefore colliding with the satellite from its front if the satellite is aligned with the orbital path. The possible aerodynamic torque that can be generated by the paddles were calculated for all the rotation angles within the saturation boundaries. Figure 5.1 shows the theoretical relationship between the paddle rotation angle θ_{pad} and the control torque N_x.

The relationship is approximated as three linear equations that can be implemented in the controller:

$$\theta_{pad} = \begin{cases} (-2.5 \times 10^7)N_x + 0.115 & \text{for } N_x < -3 \times 10^{-9} \\ (-6.4 \times 10^7)N_x & \text{for } |N_x| < 3 \times 10^{-9} \\ (-2.5 \times 10^7)N_x - 0.115 & \text{for } N_x > 3 \times 10^{-9} \end{cases} \quad \text{rad} \tag{5.2.10}$$

This estimated rotation angle is low pass filtered with a filtering time constant of 100 seconds to prevent the rotation angle command to the motors of the paddles to change

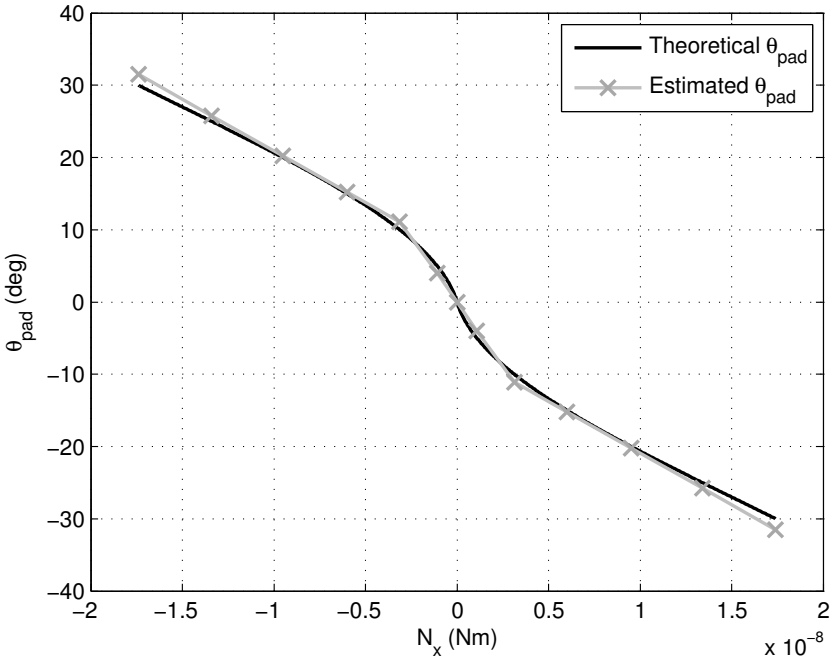

Figure 5.1: Relationship between θ_{pad} and N_x

too abruptly. The needed roll control torque was determined by a proportional-derivative (PD) based attitude controller

$$N_x = -(K_P \hat{q}_{1e} + K_D \hat{\omega}_{xo}) \tag{5.2.11}$$

where K_P and K_D are the controller gains, $\hat{q}_{1e}$ is the estimated quaternion roll error and $\hat{\omega}_{xo}$ is the estimated ORC body roll rate. A number of controller gain sets, all optimally damped, but with different settling times, were evaluated by means of simulation. It resulted in the use of a design that is optimally damped with a 2% settling time of 2000 seconds.

The magnetic attitude controller works similar to the cross product control law given by [21], except that the controller gains of the PD quaternion feedback error vector $\mathbf{e}$ is smaller and only the roll component of the estimated quaternion error vector is included. This is because the magnetic controller is only incorporated to damp the pitch and yaw rates while assisting the paddles with roll control. The control law can be written as:

$$\mathbf{M} = \frac{\mathbf{e} \times \mathbf{B}_{meas}}{\|\mathbf{B}_{meas}\|} \tag{5.2.12}$$

with

$$\mathbf{e} = \begin{bmatrix} 6.5\hat{\omega}_{xo} + 0.06\hat{q}_{1e} \\ 6.5\hat{\omega}_{yo} \\ 6.5\hat{\omega}_{zo} \end{bmatrix} \tag{5.2.13}$$

All the estimated states used in the XProd control method are supplied by the combination of the sun RKF estimator and Triad algorithm. Control therefore only occurs in the sunlit part of the orbit, during periods where valid measurements are available.

5.3 Pointing Control

The satellite must be stabilised with a pointing accuracy of 1° RMS before imaging can take place. Reaction wheels are added to the satellite control system to meet this requirement.

In this section, three reaction wheel control methods are considered, namely the XProd controller with a Y-momentum bias, the pitch axis control and the quaternion feedback controller. The first two control laws require only the addition of one reaction wheel that spins about the Y_B-axis. The third method requires three wheels, one for each body axis of the satellite.

5.3.1 XProd Control Law with Y-momentum bias

This control method uses the XProd control law as defined in Section 5.2.2, but adds a Y-momentum bias to it by spinning up the reaction wheel aligned with the Y_B-axis of the satellite to a reference angular velocity. This momentum bias will ensure gyroscopic stiffness against disturbance torques about the X_B and Z_B-axis. The angular momentum reference magnitude can be defined as

$$\left|h_{\omega y(ref)}\right| >> \omega_o(I_{xx} + I_{zz}) \tag{5.3.1}$$

with I_{xx} and I_{zz} the principle moments of inertia about the X_B and Z_B-axis and ω_o the orbital rate magnitude. The angular momentum reference for this project is defined as $h_{\omega y(ref)} = -0.0005\,\text{Nms}$.

5.3.2 Pitch Axis Control Law

The pitch axis control law [39] uses the reaction wheel aligned with the Y_B-axis, also known as the Y-wheel, to control the pitch angle of the satellite. It also includes a magnetic controller that utilises all three magnetic torque rods to do momentum management of the Y-wheel and to counteract nutation of the roll and yaw axes.

A PD-type controller is used to control the wheel torque. Saturation limits are used to incorporate the maximum reaction wheel torque $N_{w(max)}$ and angular momentum $h_{w(max)}$

values:

$$\begin{aligned} N_{wy} &= K_P\hat{q}_{2e} + K_D\hat{\omega}_{yo} && \text{and } |N_{wy}| \leq \left|N_{wy(max)}\right| \\ h_{wy} &= \int N_{wy}dt && \text{and } |h_{wy}| \leq \left|h_{wy(max)}\right| \end{aligned} \tag{5.3.2}$$

where $\hat{q}_{2e}$ is the estimated quaternion pitch error and $\hat{\omega}_{yo}$ is the estimated ORC body pitch rate. The PD controller gains K_P and K_D are designed for an optimally damped system with a 2% settling time of 130 seconds.

The cross-product control law of (5.2.12) is implemented to maintain the wheel momentum at the value $h_{wy(ref)}$, also used in Section 5.3.1, and to enforce nutation damping in the roll and yaw angles. The specific quaternion feedback error vector $\mathbf{e}$ is given by

$$\mathbf{e} = \begin{bmatrix} 6.5\hat{\omega}_{xo} \\ K_Y\left(h_{wy} - h_{wy(ref)}\right) \\ 6.5\hat{\omega}_{zo} \end{bmatrix} \tag{5.3.3}$$

where K_Y is the derivative gain used to control the wheel momentum. This gain is chosen to result in a Y-axis feedback error e_Y that will be close to the X-axis feedback error e_X [40]. Assuming a roll rate equivalent to the orbital rate, the feedback roll error will be:

$$e_X = 6.5\hat{\omega}_{xo} = 6.5 \times 0.001 = 0.0065 \tag{5.3.4}$$

Allowing a momentum error of 10% for the Y-wheel and replacing e_Y with e_X, the derivative gain K_Y can be calculated as:

$$K_Y = \frac{e_Y}{\left|h_{wy} - h_{wy(ref)}\right|} = \frac{0.0065}{0.1 \times \left|h_{wy(ref)}\right|} = 130 \tag{5.3.5}$$

5.3.3 Quaternion Feedback Control Law

The quaternion feedback control law [22] uses three reaction wheels to control the satellite to a specific orientation and three magnetic torque rods to perform momentum management of the reaction wheels. Unlike the two previous control methods, this control law does not make use of the aerodynamic roll control paddles.

A PD-type controller is used for the reaction wheels. The controller gains k_p and k_d are designed for an optimally damped system with a 2% settling time of 40 seconds. The control law can be expressed as:

$$\mathbf{N}_w = k_p\mathbf{I}\hat{\mathbf{q}}_e + k_d\mathbf{I}\hat{\boldsymbol{\omega}}_B^O \tag{5.3.6}$$

$$= \begin{bmatrix} (0.000284)\hat{q}_{1e} + (0.0014)\hat{\omega}_{xo} \\ (0.0014)\hat{q}_{2e} + (0.007)\hat{\omega}_{yo} \\ (0.0013)\hat{q}_{3e} + (0.0067)\hat{\omega}_{zo} \end{bmatrix} \tag{5.3.7}$$

where $\mathbf{I}$ is the moment of inertia matrix defined in (2.2.1), $\hat{\mathbf{q}}_e$ is the quaternion error vector of (2.1.10) and $\hat{\boldsymbol{\omega}}_B^O$ is the estimated ORC angular body rate vector.

A magnetic controller [25] is used to desaturate the reaction wheels and to control their Y-angular momentum to the reference value $h_{wy(ref)}$. The required magnetic moment is defined as:

$$\mathbf{M} = \frac{130}{\|\mathbf{B}_{meas}\|} \left(\begin{bmatrix} h_{wx} \\ h_{wy} - h_{wy(ref)} \\ h_{wz} \end{bmatrix} \times \mathbf{B}_{meas} \right) \tag{5.3.8}$$

where $\mathbf{h}_w = \begin{bmatrix} h_{wx} & h_{wy} & h_{wz} \end{bmatrix}^T$ is the wheel momentum vector and $\mathbf{B}_{meas}$ is the measured geomagnetic field vector.

The quaternion feedback control law can only be implemented in the sunlit part of the orbit. That is because it uses the estimated angular body rate vector and the attitude quaternion vector supplied by the Triad algorithm and sun RKF estimator.

5.4 Controller Simulation Results

The effectiveness of the various control methods are evaluated through simulations based in the environment described in Chapter 3. The different control methods for each control mode are compared with one another in terms of a few parameters, namely the magnetic torque rod (MT) on-time, paddle rotation, settling time, wheel control torque, attitude error and pointing accuracy.

The MT on-time is the sum of the total on-time in seconds of each MT for the whole duration of the simulation. The paddle rotation θ_{total} is a measure of how active the control paddles are during control presented in radians. The settling time t_s is defined as the simulation time at which all three attitude angles are controlled within $\pm 10^\circ$ of the reference attitude. The wheel control torque $N_{w(total)}$ is defined for the pointing control mode and consists of the total amount of wheel torque that was used during the simulation. The attitude error is defined for the three-axis stabilisation control mode. It is defined as the square root of the mean of the attitude error squared,

$$RMSE = \sqrt{\frac{\sum_{k=n}^{T_R} \left(|\phi_k - \phi_{ref,k}|^2 + |\theta_k - \theta_{ref,k}|^2 + |\psi_k - \psi_{ref,k}|^2 \right)}{T_R + 1 - n}} \tag{5.4.1}$$

where $T_R = T_N/T_s$ is the total number of sample steps T_s present in the total simulation time T_N, n is the starting sample step from where the error is calculated and ϕ_k, θ_k and ψ_k represent the Euler roll, pitch and yaw angles at sampling time k.

The RMS pointing accuracy is defined for the pointing control mode. This parameter is based only on the roll ϕ and pitch θ errors. The yaw error will not affect the pointing

accuracy of the camera payload, because the boresight of the camera payload is aligned with the Z_B-axis. Imaging will only take place during the sunlit part of the orbit when the camera payload is controlled to the right target. Therefore, the pointing accuracy will only include error values during these valid control intervals and can be written as:

$$RMSP = \sqrt{\frac{\sum_{k=n}^{T_R} \left(|\phi_k - \phi_{ref,k}|^2 + |\theta_k - \theta_{ref,k}|^2 \right) C_k}{T_R + 1 - n - T_{invalid}}} \tag{5.4.2}$$

where $C_k = 1$ if the time step k falls within a valid control interval and $C_k = 0$ if not. The variable $T_{invalid}$ represents the amount of invalid time steps between $k = n$ and $k = T_N$.

The sampling time for the simulation and all the controllers is chosen as $T_s = 1$ second. All controllers are enabled at $t = 2\,000$ seconds and the simulation end time T_N is at $t = 40\,000$ seconds. The required estimated states for the detumbling mode is supplied by the magnetic RKF. All other control modes rely on the sun RKF and Triad algorithm for estimated states. The shaded areas in the simulation figures represent the intervals where the sun and nadir measurements are invalid. During these intervals the control methods that use the sun RKF and Triad estimates applies no control to the satellite.

5.4.1 Detumbling Control

The detumbling controller [37] that consists of the B-dot and Y-spin controller is the only considered control method. The initial rates are set to $\boldsymbol{\omega}_B^O = \begin{bmatrix} 1.2 & -5 & -1.5 \end{bmatrix}^T$ degrees per second and the initial orientation is set to zero roll, pitch and yaw angles. The controller is switched on at $t = 2\,000$ seconds. Figure 5.2 shows the ORC body rates over the first 8000 seconds of the simulation.

The rates about the X_B- and Z_B-axis are damped to rates within a ± 0.05 degrees per second margin within a third of an orbit. The reference body rate about the Y_B-axis is defined as -2 degrees per second. This rate is followed within 500 seconds with a maximum error of 0.2 degrees per second. The total MT on-time at $t = 4\,000$ seconds is 463 seconds. This value increases by 116% to a total on-time of 1 000 seconds at $t = 40\,000$ seconds in order to maintain these controlled rates.

A second simulation is executed where the Y_B reference rate is set to zero degrees per second. The results are shown in Figure 5.3.

The body rates are controlled to the zero reference with a ± 0.7 degrees per second error margin within 4 000 seconds after the controller is switched on. This error margin is larger than the error margins of the previous simulation, especially about the roll and yaw axes because the Y_B rate is now too small to cause gyroscopic stiffness against roll and yaw disturbance torques as it did in the previous simulation. This also leads to the use of

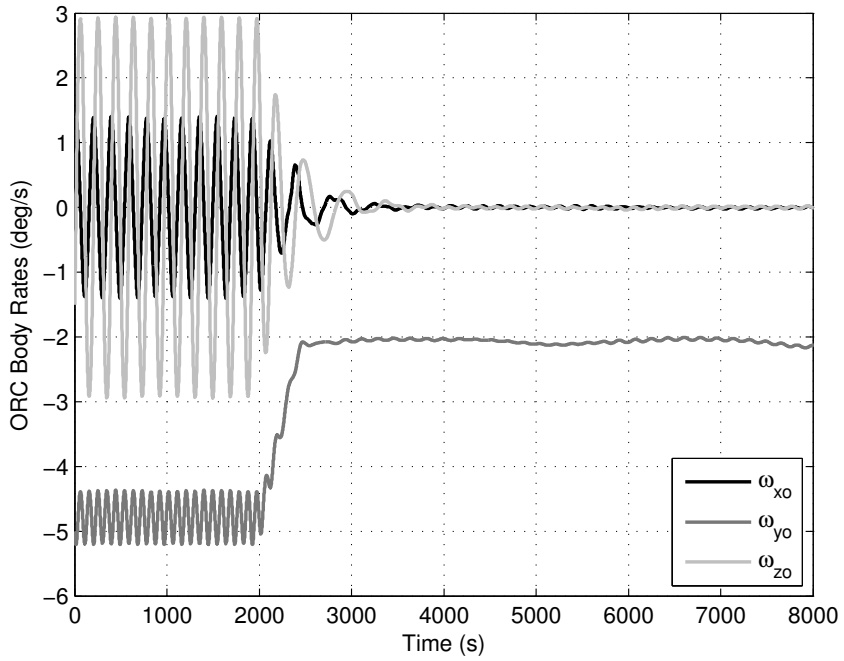

Figure 5.2: Detumbling of ORC angular body rates, $\omega_{y(ref)} = -2\,^\circ/\text{s}$

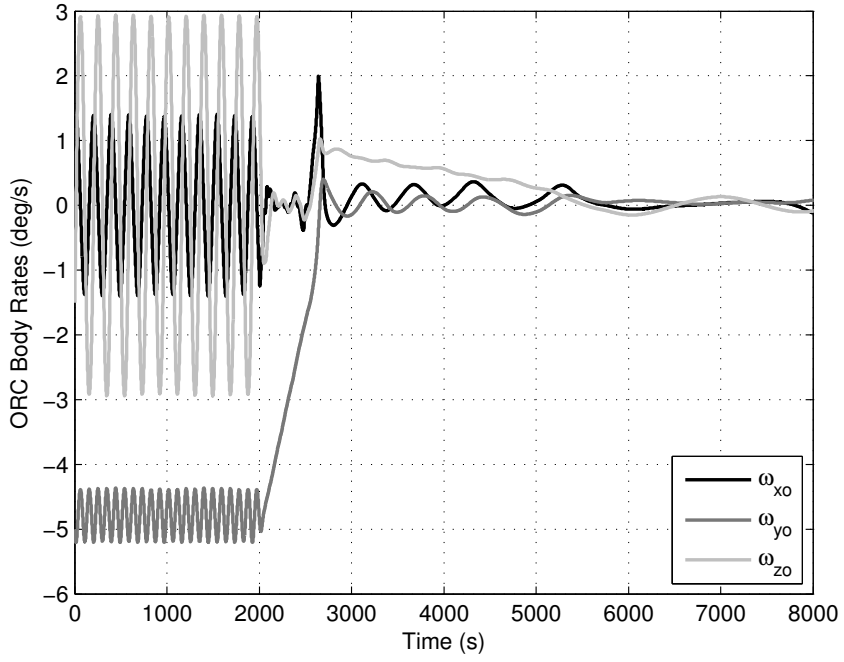

Figure 5.3: Detumbling of ORC angular body rates, $\omega_{y(ref)} = 0\,^\circ/\text{s}$.

more magnetic torque to counter these disturbance torques. A total MT on-time of 1 174 seconds is used to reach the controlled state at $t = 6\,000$ seconds. This value increases to 2 517 seconds for the remainder of the simulation period. This is a 114.5% increase.

The simulations show that the B-dot and Y-spin contoller can detumble the satellite sufficiently for the three-axis stabilisation mode to start.

5.4.2 Three-Axis Stabilisation

The goal of this control mode is to stabilise the satellite to a zero roll, pitch and yaw (RPY) orientation. Two control methods are evaluated, namely the compass-like PID control law and the XProd control law. The initial ORC body rates are set to zero degrees per second, since the preceding detumbling controller ensures low body rates. The initial attitude roll, pitch and yaw angles are set to 30°, 20° and −20° respectively.

The three-axis stabilisation attitude result of the compass-like PID controller is shown by Figure 5.4. The pitch and yaw attitude angles are controlled to within a ±10° bound at $t = 11\,000$ seconds. The roll angle, however, repeatedly ventures just beyond this bound. The MT on-time at $t = 11\,000$ seconds is 39.26 seconds and the total MT on-time at the end of the simulation is 101.8 seconds. The RMSE over the last 12 000 seconds of the simulation is 6.21 degrees.

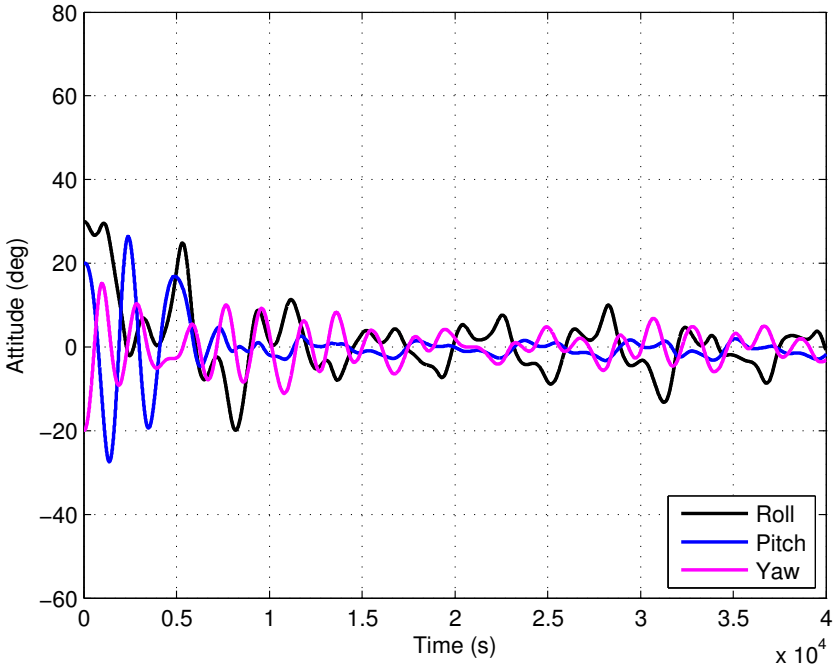

Figure 5.4: Attitude angles during compass-like PID control

The attitude result of XProd control law is shown in Figure 5.5. This control law executes only during the non-shaded areas on the graph when estimated states are available.

The settling time, as defined in Section 5.4, for this control method is about 25 000 seconds, but the RPY angles are controlled to angles smaller than ±5° at $t = 34\,282$ seconds. The RMS attitude error over the last 12 000 seconds of the simulation is 3.23 degrees. At $t = 25\,000$ seconds the MT on-time is 118 seconds and another 14.8 seconds is needed to keep the attitude angles within the ±5° bound for the remainder of the simulation time.

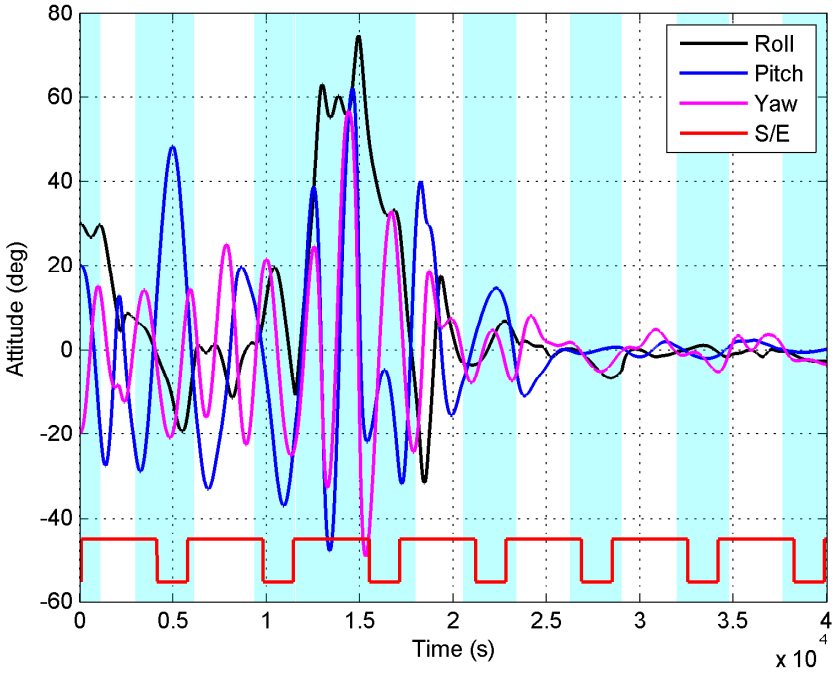

Figure 5.5: Attitude angles with XProd control

The positive Z_B paddle angle θ is shown in Figure 5.6. As the satellite is stabilised the aerodynamic roll paddles become less active.

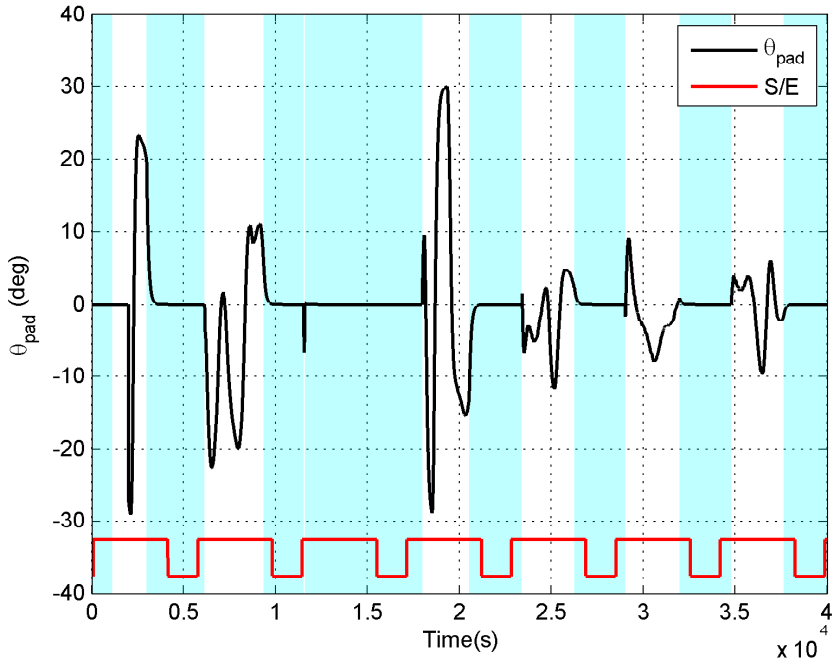

Figure 5.6: The positive Z_B paddle control angle

In Table 5.1 the performance of the two three-axis stabilisation methods are listed. The

compass-like PID control law uses 23.3% less magnetic torque, but has a 31.3% longer settling time than the XProd control law. The XProd control does not only utilise more magnetic torque, but also uses the roll control paddles. It therefore requires more power than the compass-like control law. However, the compass-like control law does not meet the requirement of a $\pm 5^\circ$ error margin while the XProd control law does. The XProd control law is therefore chosen as the better three-axis stabilisation method even if it requires more power.

Table 5.1: Summary of three-axis stabilisation mode.

Controller	t_s (s)	MT (s)	θ_{total} (rad)	RMSE (°)
Compass-like PID	31 600	101.8	-	6.21
XProd	24 070	132.8	2 421	3.23

5.4.3 Pointing Control

The pointing control mode forms a crucial part of the imaging stage. The satellite must be controlled to a target orientation with an accuracy of 1° RMS. Three control methods that make use of reaction wheels are evaluated, namely the XProd control law with a Y-momentum bias, the pitch axis control law and the quaternion feedback (QF) law.

The desired orientation of the simulation is with the Z_B-axis of the satellite pointed to nadir, meaning that zero roll and pitch angles are required. The desired yaw angle is set to zero, but since the Z_B-axis is parallel to the boresight of the camera it will not influence the pointing accuracy.

The results of the XProd control law with a momentum bias is shown in Figure 5.7. The settling time is 6 770 seconds and at $t = 14\,330$ seconds the attitude angles are all controlled within $\pm 2.5^\circ$ of the required attitude. The MT on-time at the end of the simulation is 150.8 seconds and the total paddle angle is 2 204 radians. The momentum bias keeps the attitude drift small during eclipse periods, but the RMSP calculated over the last 12 000 seconds is 1.31 degrees. The total accumulated wheel torque needed to spin up the momentum wheel is 0.0005 Nm.

Figure 5.8 shows the attitude angles of the pitch axis control law simulation. The pitch angle is controlled very close to zero while the roll and yaw angles stay within the $\pm 10^\circ$ bound after $t = 2\,502$ seconds. At the end of the simulation the required MT on-time is 162.7 seconds and the total accumulated paddle angle is 2 980 radians. Although the pitch angle is sufficiently controlled, the roll and yaw angle errors remain large, because the XProd controller struggles to overcome the stiffness of the pitch wheel momentum.

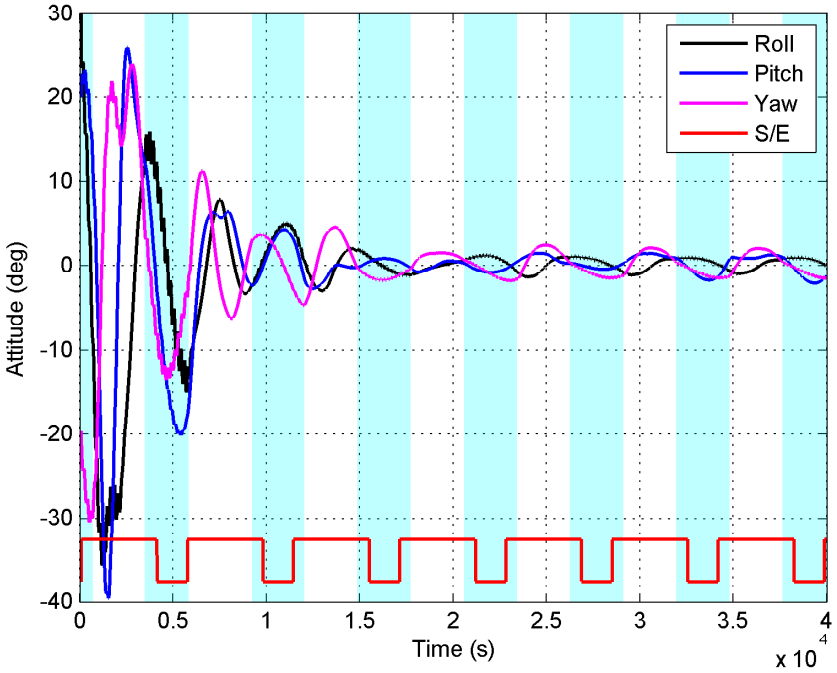

Figure 5.7: Attitude angles with Y-momentum bias control

The pitch axis control law results in a RMSP of 2.14° over the last 12 000 seconds of the simulation. The total wheel torque at $t = 40\,000$ seconds is 2.15 mNm.

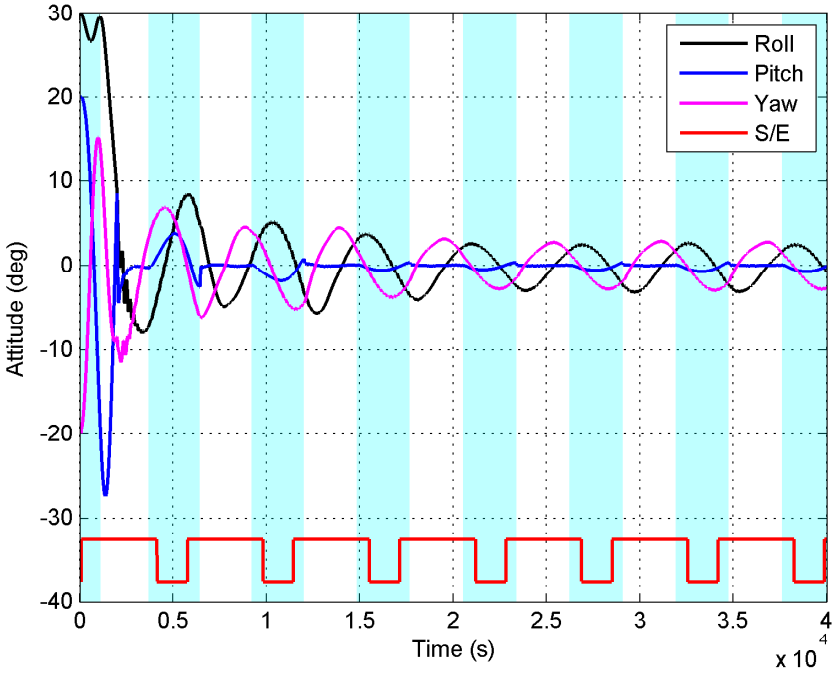

Figure 5.8: Attitude angles with pitch axis control

The final control method implemented was the quaternion feedback (QF) control law. The

attitude of the satellite is shown in Figure 5.9. A short control burst at $t = 6\,330$ seconds disrupted the attitude, but it is corrected in the next control period. This method requires 163.1 seconds of magnetic control to perform momentum management of the reaction wheels for the duration of the simulation. The total wheel torque at $t = 40\,000$ seconds is 51.39 mNm. The pointing accuracy of this controller over the last two valid measurement regions is 0.13 degrees.

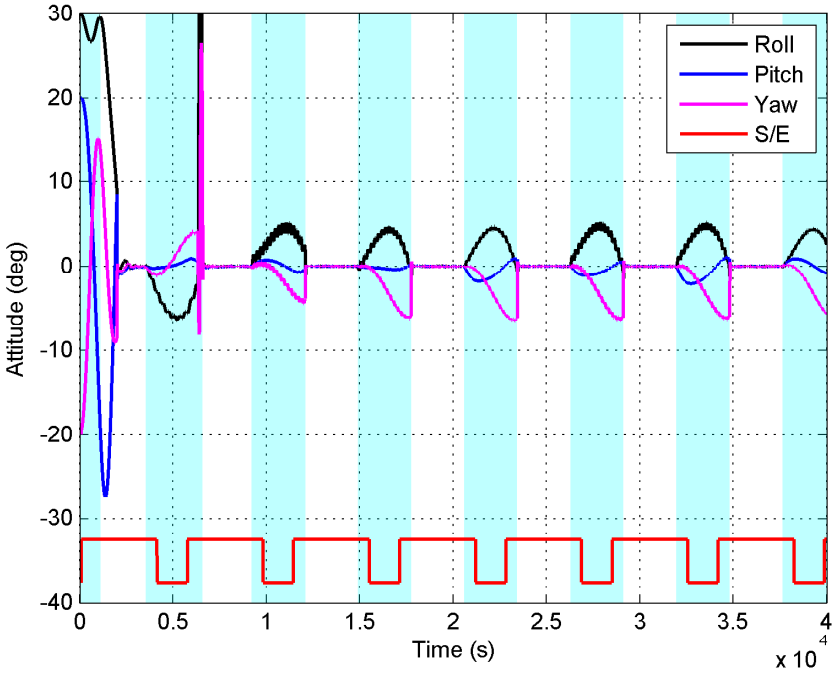

Figure 5.9: Attitude angles with quaternion feedback control

Table 5.2 summarises the performance of the pointing control methods. The pitch axis control law requires more magnetic, paddle and wheel control than the XProd with a Y-momentum bias control law, but achieves a poorer pointing accuracy. The XProd with Y-momentum bias control law has a pointing accuracy of 1.31°. The only control method that fulfils the requirement of 1° RMS pointing accuracy is the quaternion feedback control law. This law does not make use of the aerodynamic roll paddles, but it utilises three reaction wheels. Although the total wheel torque needed by the QF controller is small, the XProd with Y-momentum bias control law requires only 0.1% of the QF torque while the pitch axis control law needs 4.2%. The three control methods utilise the magnetic torque rods to approximately the same extent.

A second simulation was implemented that evaluates the ability of the controllers to perform roll off-pointing of the imaging payload within one sunlit part of an orbit. The control law should point the satellite to the desired orientation of 10° roll and 0° pitch angle, keep the satellite stable at this point with an accuracy of 1° RMS for 1 500 seconds

Table 5.2: Summary of pointing control methods.

Controller	t_s (s)	MT (s)	θ_{total} (rad)	$N_{w(total)}$ (Nm)	RMSP (°)
Y-Bias	6 770	150.8	2 204	0.0005	1.31
Pitch Axis	2 502	162.7	2 980	0.00215	2.14
QF	6 600	163.1	-	0.05139	0.13

and then point the payload back to nadir. The result of the quaternion feedback control law is shown in Figure 5.10. This is the only control method that achieves these simulation requirements.

The manoeuvre has a 2% settling time of 41 seconds and a peak overshoot of 9% that relates to a damping ratio of $\zeta = 0.608$. The design values of the controller has an optimal damping ratio with $\zeta = 0.707$ and a 2% settling time of 40 seconds. The controller needs 13.2 seconds of magnetic control and a total accumulated wheel torque of 4.59 mNm to complete the whole roll off-pointing manoeuvre. The pointing accuracy of the satellite over the time interval $t = 46\,541$ seconds to $t = 48\,000$ seconds is 0.038 degrees. The pointing stability over this interval is within a ± 0.03 degrees per second bound.

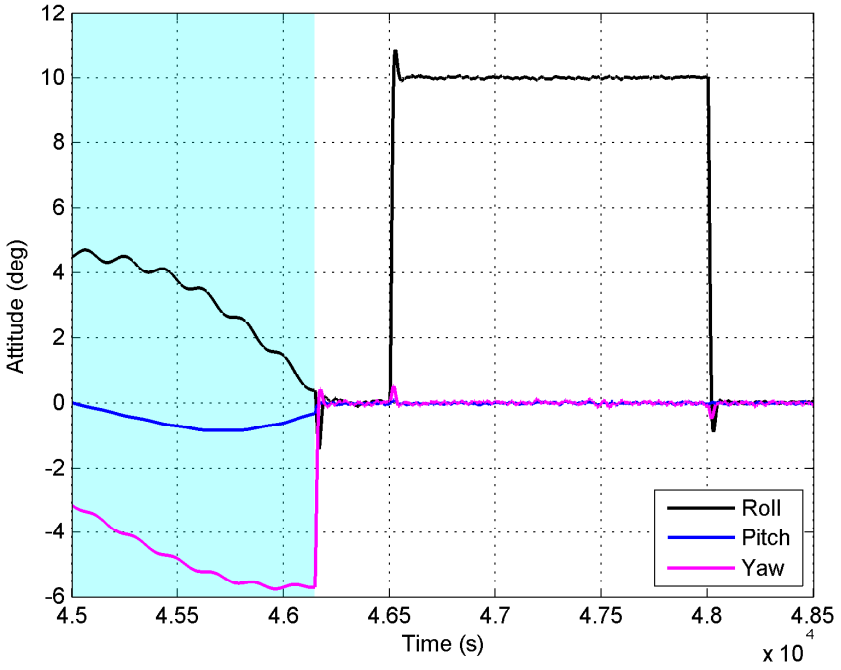

Figure 5.10: Roll off-pointing with quaternion feedback control

5.5 Hardware-in-the-loop Simulation

A hardware-in-the-loop (HIL) simulation is conducted with the ADCS on-board computer designed by Botma [13]. The goals of the simulation are to verify that the ADCS OBC has the ability to evaluate and execute the models, attitude determination and control algorithms correctly with a computation time smaller than the required 1 second time step. For this HIL simulation, only the detumbling controller with the models and attitude determination methods needed for this controller, is implemented.

The simulation requires two main components, namely the personal computer (PC) and ADCS OBC. The PC acts as the main satellite OBC. It is responsible for providing the ADCS OBC with initial simulation variables and simulated measurement values when requested by the ADCS OBC. The PC also executes all the models, attitude determination methods and control methods the ADCS OBC executes, in order to provide a result set to compare the ADCS OBC results with. The PC side of the simulation is implemented by means of a Simulink model. The ADCS OBC must request measurement values from the PC, evaluate the models, determination methods and chosen control algorithm and then supply the PC with the required control action and the estimated states. The sequence of the simulation is explained in the following paragraphs.

At the start of the simulation the desired control method, initial controller time step and reference values are set by the PC and transmitted to ADCS OBC. Table 5.3 shows the communication protocol for transmission from the PC to the ADCS OBC.

Table 5.3: Transmission protocol from PC to ADCS OBC [13].

ID	Data length		Data content	Unit
$	3×(short int)	6 bytes	Magnetometer readings	μTesla
&	1×(char)	1 byte	Controller mode	0-256
#	1×(short int)	2 bytes	Reference Y-spin rate	milli-deg/s
%	1×(char)	1 byte	Controller sample time	0-256 s
@	only identifier	0 bytes	Acknowledgement	

After the ADCS OBC receives the initial values, it evaluates the models, determination method and control algorithm at each time step. If measurement values are needed the ADCS OBC sends a request to the PC. At the end of each time step the ADCS OBC sends the estimated ORC body angular rates, the needed MT on-time and the expected resulting magnetic torque back to the PC using the communication protocol listed in Table 5.4. These values are then compared to the corresponding values generated by the PC to establish whether the ADCS OBC executed the algorithms correctly.

Table 5.4: Transmission protocol from ADCS OBC to PC [13].

ID	Data length		Data content	Unit
R	only identifier	0 bytes	Request sensor measurements	
T	3×(short int)	6 bytes	MT on-time	seconds
W	3×(short int)	3 bytes	Estimated body angular rates	milli-deg/s
N	3×(double)	24 bytes	Magnetic torque	Nm

Figures 5.11 and 5.12 show the comparisons of the estimated ORC body rates and the needed MT on-time calculated by the PC and the ADCS OBC. It can be seen that the ADCS OBC values follow the generated PC values very closely.

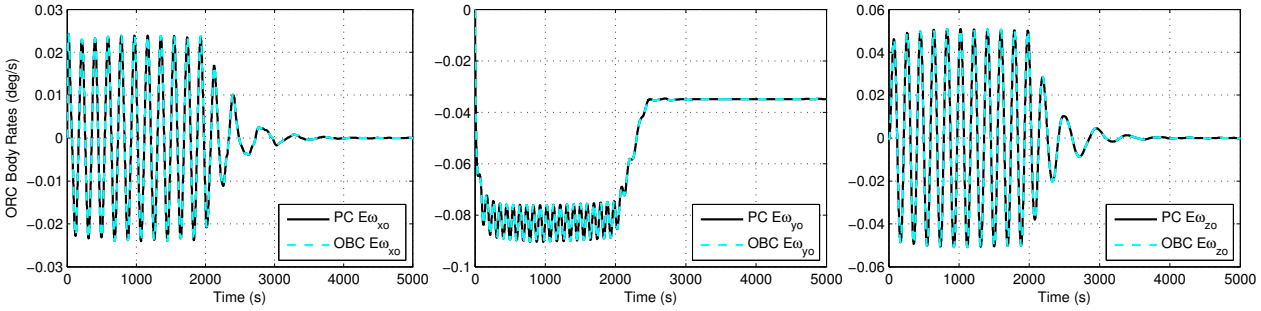

(a) Roll rate (b) Pitch rate (c) Yaw rate

Figure 5.11: Estimated ORC body rates of the PC and the ADCS OBC.

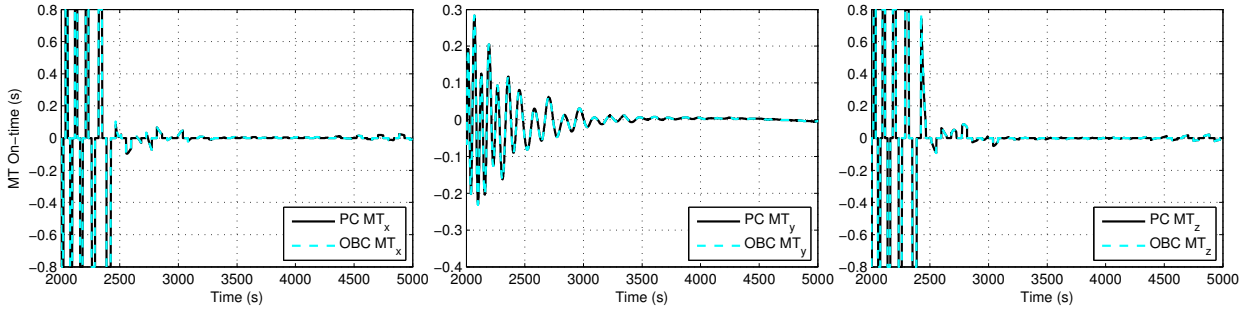

(a) MT_x (b) MT_y (c) MT_z

Figure 5.12: MT On-time computed by the PC and the ADCS OBC.

The ADCS OBC requires a total of 22.1 milli-seconds per time step to execute all the ADCS algorithms in the control loop. Table 5.5 gives a summary of the computation time distribution between the models, determination method and the control algorithm. The computation time is much shorter than the 1 second time step and the ADCS OBC should therefore be capable to execute more models and more complex control algorithms within the desired time step.

Table 5.5: Computation time of the ADCS OBC.

Algorithms	Time (ms)
Models	18.6
Determination	3
Control	0.5

5.6 Summary

The satellite requires three different control modes during its lifetime. The detumbling mode is used shortly after the deployment of all mechanical parts to reduce and control the angular body rates of the satellite. When the body rates are sufficiently controlled, the three-axis stabilisation mode is used to control the attitude of the satellite to a desired orientation within an error bound of ±5 degrees. The third control mode is the pointing control mode used during imaging to point the camera payload in a specific direction with a pointing accuracy below 1° RMS.

For the detumbling mode only a single detumbling controller of [37] was considered. It consists of a B-dot and Y-spin controller that utilises three magnetic torque rods. The B-dot control law is used to damp the roll and yaw rates of the satellite to zero degrees per second. The Y-spin control law is used to control the pitch rate to a specific reference value. In the first simulation the reference pitch rate was −2 degrees per second. The yaw and roll rates were damped sufficiently within an error bound of ±0.05 degrees per second while the pitch rate error was ±0.2 degrees per second. The second simulation had a zero pitch rate reference. All the angular rates were controlled to zero with a ±0.7 degrees per second error. This control method proved to be sufficient to detumble the satellite before the start of the three-axis stabilisation mode.

Two aerodynamic control methods were evaluated for the three-axis stabilisation mode. The compass-like PID control method makes use of the passive aerodynamic pitch-yaw control system and a magnetic controller. The magnetic controller damps the aerodynamic pitch-yaw system and stabilises the roll angle of the satellite. The XProd control method also utilises the passive aerodynamic pitch-yaw control system, but includes active aerodynamic roll control by means of two aerodynamic roll control paddles. A cross-product magnetic controller is used to support the paddle controller and to damp the aerodynamic pitch-yaw system. The performance of both control methods where evaluated through simulation. The compass-like PID control method stabilised the pitch and yaw angles within a ±10° error margin, while the roll angle stayed within ±15° of the reference value. The XProd control method took longer to stabilise, but reached the desired attitude angles within an error margin of ±5 degrees.

Three control methods were evaluated for the pointing control mode. The first consists of the XProd control method with an added Y-momentum bias from a reaction wheel. The pitch axis control method used a reaction wheel in the Y_B-axis to control the pitch angle of the satellite, while the quaternion feedback control method utilises three reaction wheels, one in each body axis. The pointing requirement was an accuracy of 1° RMS and was only met by the quaternion feedback control method.

These simulation results are used to decide upon the best control method to be used for each control mode. The B-dot and Y-spin controller will be used for detumbling since it provides sufficient performance. The three-axis stabilisation mode will make use of the aerodynamic and cross-product control law, because it meets the set requirements. The quaternion feedback control law is chosen for the pointing control mode due to its excellent performance during nadir pointing, as well as during roll off-pointing manoeuvres.

A hardware-in-the-loop simulation was also conducted with the on-board computer designed by Botma [13]. The simulation was used to test whether the ADCS OBC can execute the algorithms needed for the detumbling controller correctly. This test was also used as an indication of the computational time needed per control loop to evaluate some of the models, a determination method and a detumbling control law.

Chapter 6

Conclusion

This chapter summarises the content of this thesis, draws some conclusions from results obtained and provides areas in which future work can be conducted.

6.1 Summary of Study

The Hermanus Magnetic Observatory required a low cost method to calibrate the radar antenna patterns of an antenna at their base in Antarctica. It was determined that a three-axis stabilised 3U CubeSat would be the most effective solution to the problem. A camera was included as a secondary payload that requires a pointing accuracy of 1°. It was decided to design the structure of the satellite to suit the use of aerodynamic control methods.

A 1U CubeSat is a small satellite measuring 10 cm×10 cm×10 cm with a mass constraint of 1.33 kg [14] and a very limited power budget due to the small amount of surface area available for solar panels. Variations of the 1U CubeSat are the 2U and 3U CubesSats measuring 20 cm×10 cm×10 cm and 30 cm×10 cm×10 cm, respectively.

Since the first launch of CubeSats in June 2003 [15] various attitude determination and control strategies have been used. The sensors that were commonly used are three-axis magnetometers, coarse and fine sun sensors and gyroscopes. In some CubeSats the lighting conditions of the solar cells were analysed to determine the satellite-to-sun vector [6]. Some of the determination methods that were implemented on the CubeSats are the Extended Kalman Filter and the QUEST algorithm. One popular control method was passive magnetic control using permanent magnets and hysteresis rods. Other control methods included the use of gravity gradient booms, active magnetic torquing or miniature reaction wheels.

The idea of using aerodynamic disturbance torques as a means of control is quite inviting

for small satellites in low earth orbits. A particular design presented by Psiaki [8] in 2004 was incorporated in the satellite structure design of this project. The final structure of the satellite consisted of a 3U CubeSat as main bus with four aerodynamic feather antennae protruding from the back of the satellite. These feathers provide passive aerodynamic pitch and yaw stability to the satellite. Furthermore, two aerodynamic roll control paddles were mounted on the positive and negative Z_B-facets of the satellite to allow for active aerodynamic roll control. The sensors of the satellite included a three-axis magnetometer, nadir sensor and fine sun sensor. Three magnetic torque rods and three nano-reaction wheels were also included as additional actuators.

The sensor measurements were used to determine the orientation of the satellite. The Triad algorithm, two Rate Kalman Filters and an Extended Kalman filter were implemented as attitude determination methods. These algorithms were evaluated and compared with one another for the scenarios of a tumbling satellite and a stabilised satellite.

The satellite's lifetime was divided into three control modes: detumbling, three-axis stabilisation and pointing control. The only controller evaluated for the detumbling mode was the B-dot and Y-spin detumbling controller [37]. Aerodynamic control methods were evaluated for the three-axis stabilisation mode and reaction wheel control methods for the pointing of the satellite.

6.2 Conclusions

6.2.1 Satellite Structure

The satellite structure deemed to be sufficient to generate aerodynamic control torques. The roll control paddles generated aerodynamic torques of approximately 2×10^{-8} Nm when they were rotated to their maximum angle of 30° and the X_B-axis of the satellite was aligned with the X_O-axis of the ORC frame. The aerodynamic feathers generated aerodynamic torques from zero, when the satellite is perfectly aligned with the ORC frame, to approximately 5×10^{-7} Nm when the X_B-axis of the satellite is normal to the X_O-axis. The magnetic torque rods were used to damp the torques generated by the aerodynamic feathers in order to realise an aerodynamically pitch-yaw stabilised satellite. Unfortunately, when this aerodynamic feather design is used for a satellite in an inclined orbit, the co-rotating atmosphere of Earth causes a periodic disturbance in the yaw angle of the satellite.

6.2.2 Attitude Determination

Attitude determination requires the use of body referenced sensor measurement vectors and in some cases the corresponding orbit referenced modelled vectors. The attitude determination algorithms that were evaluated are the Triad, magnetic Rate Kalman Filter, sun Kalman Filter and Extended Kalman Filter algorithms. The Triad algorithm determines only the attitude vector of the satellite. The magnetic RKF produces the ORC angular body rate vector while the sun RKF produce the ECI angular body rate vector of the satellite. The Extended Kalman Filter produce both the attitude vector and the ECI angular body rate vector. The performance of these algorithms were evaluated for two simulation sets, one where the satellite was tumbling and the other where the satellite was stabilised.

In the case of the tumbling satellite, the ORC angular body rate vector is required by the detumbling controller to stabilise the satellite. The magnetic RKF shows steady-state estimation errors of ± 0.3 degrees per second. The sun RKF was combined with the Triad algorithm to determine the ORC angular body rate vector. Due to the short availability periods of the sun measurement vector, the sun RKF performed poorly and estimation errors up to ± 4 degrees per second were made. The EKF used the determined attitude vector to transform the determined ECI angular body rate vector to the ORC frame. The EKF required 500 seconds to converge to the true vector values and produced a steady-state error of ± 0.1 degrees per second. The EKF performed the best, but required more computational power from the satellite. Since the available power is limited when the satellite is tumbling, it was decided that the magnetic RKF will be used to compute the ORC angular body rate vector when the satellite is tumbling.

In the stabilised scenario the satellite experiences low angular rates. In order to control the satellite, the ORC angular body rate and the attitude vector is required. The following results are confined to the sunlit part of the orbit, in periods where the sun measurement vector is valid: the error of the magnetic RKF is within a 0.2 degrees per second bound. The sun RKF and Triad combination resulted in a steady-state error of ± 0.005 degrees per second. The EKF produced an ORC angular body rate vector within the same error bound, but with a settling time that is twenty times shorter. The attitude vector estimation error of the Triad algorithm is approximately 0.4° which is twice the magnitude of the attitude vector error of the EKF. The computational simplicity of the Triad and sun RKF combination made it the more viable option and it was chosen as the attitude determination method to be used when the satellite is not tumbling.

6.2.3 Control Algorithms

Three control modes were identified for the duration of the satellite's lifetime. For the detumbling mode only a single control method was considered. This detumbling controller [37] required three magnetic torque rods and was evaluated by means of two simulations of a tumbling satellite. In both simulations the roll and yaw rates were sufficiently damped and the pitch rate was controlled to the commanded spin rate.

Two aerodynamic control methods were evaluated for the three-axis stabilisation mode. The desired accuracy was set to ±5 degrees. Both control methods required the use of three magnetic torque rods. The compass-like PID controller [8] achieved three-axis stabilisation within a ±15 degrees error margin which did not satisfy the requirements. The XProd control method also included the use of aerodynamic roll control paddles and achieved an error margin of ±5 degrees.

The third control mode was the pointing control mode that was needed during imaging procedures. An pointing accuracy of 1° RMS was required. The first control method comprised of the XProd controller with an added Y-momentum bias from a reaction wheel. The second method was the pitch axis control method where a reaction wheel in the Y_B-axis was used to control the pitch angle of the satellite. Both these methods also required the use of three magnetic torque rods, but neither one satisfied the pointing requirement. The quaternion feedback control method utilised three reaction wheels and three magnetic torque rods. It achieved a pointing accuracy of 0.13 degrees. It was also evaluated for a roll off-pointing manoeuvre in which it performed extremely well.

The detumbling controller [37] will be utilised in the final design for the detumbling mode. For three-axis stabilisation the aerodynamic XProd control method will be used and the quaternion feedback control method will satisfy the pointing control mode requirements.

6.3 Further Work and Recommendations

The preferred attitude determination and control methods must be implemented on the ADCS on-board computer in order to determine the maximum computation time needed and to verify that the OBC has the ability to execute these methods correctly. If one of the determination or control methods prove to be too complex, a simpler method must be obtained, evaluated and implemented again.

In Section 2.2.1 a constraint is set to the nadir sensor to prevent the use of measurements with large errors. It was specified that if the nadir vector falls outside a 120° FOV of the camera, the measurement must be discarded as invalid, because the visible profile of Earth is too small. However, this constraint may be too loose. If the boresight of the

camera is moved 30° away from the nadir direction, the edge of Earth moves out of the FOV of the camera. If the satellite continues to move away, the measurement errors will increase as the Earth's profile decreases. The accuracy of the nadir sensor for a full profile of Earth varies between 0.1° and 0.46° [12]. For the simulations, realistic measurements were generated by adding noise to the modelled vectors. In Table 4.2 the maximum error value for the nadir sensor measurement was assumed as 0.2° which is a value between 0.1° and 0.46°. If the nadir vector falls outside a 60° FOV of the camera, the measurement error will be more than 0.46°.

A more reliable constraint would therefore be: if the nadir vector falls outside a 60° FOV, the measurement should be discarded. Another approach would be to increase the maximum measurement error value, used to generate realistic simulation measurements, to a value that corresponds to the allowed valid measurement FOV angle.

The simulation orbit is defined as a 9 am/pm sun-synchronous orbit which relates to an approximately constant angle of 45° between the sun vector and the orbital plane. If the satellite body frame is aligned with the orbit reference frame then one of the Y_B-facets of the satellite will experience an approximately constant incidence angle with the sun vector whenever the satellite is in the sunlit part of the orbit. By placing the fine sun sensor with its boresight aligned with the outward normal vector of this sunlit Y_B-facet, it can be ensured that the sun sensor measurement is valid for the whole sunlit part of the orbit, if the satellite stays stabilised.

For the simulation orbit used, the negative Y_B-facet will be the sun-facing Y_B-facet. The sun sensor is relocated to point its boresight in the negative Y_B-direction. The effect of this sensor movement was verified by means of a simulation. The sun RKF was used for attitude determination, as well as the Triad algorithm. It must be noted that the nadir sensor will still only produce valid measurements for half the orbital period if the satellite is stabilised. For the other half of the orbital period the satellite will either be in eclipse or the sun will fall directly onto the nadir sensor and saturate it. The Triad algorithm therefore uses the sun and nadir vector measurement if the nadir measurement is valid. If the nadir measurement is invalid the Triad algorithm uses the sun and geomagnetic field vector measurement. The quaternion feedback control method was implemented on the satellite with the same conditions as was used in Section 5.4.3. The initial roll, pitch and yaw were respectively 30°, 20° and -20° and the initial orbital rates were zero degrees per second. Figure 6.1 shows the attitude result of the simulation.

The red signal S/E represents the change between the sunlit part of the orbit and eclipse. The rising edges of the signal represents the cross-over into sunlight and the falling edges the change back to eclipse. The shaded areas represent the periods of invalid sun vector

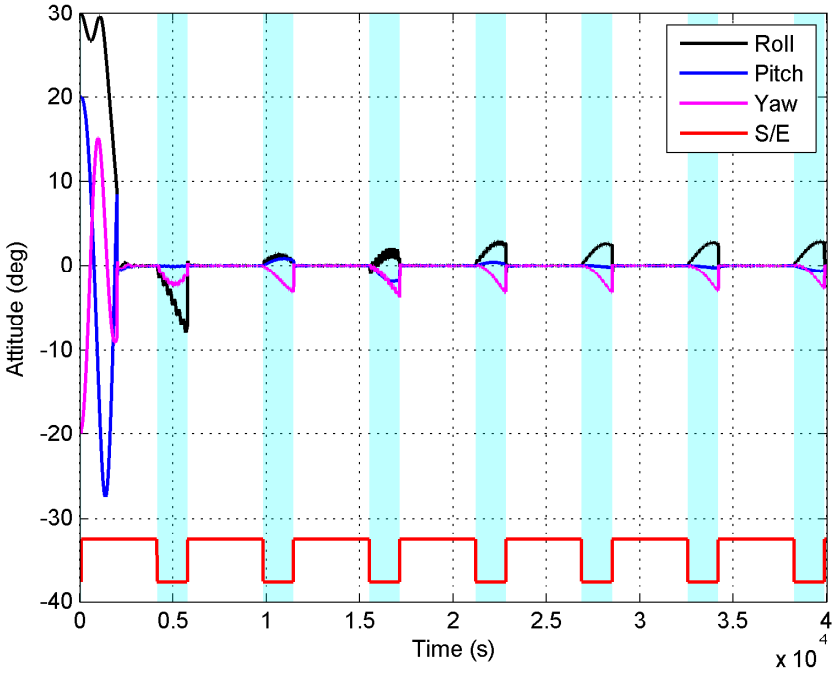

Figure 6.1: Quaternion Feedback controller with improved valid control periods. These valid periods are represented by the non-shaded columns.

measurements and it is clear that these periods fall within the eclipse period. The sun vector measurement from this relocated sun sensor is therefore valid for the entire sunlit part of the orbit. The result is a 32% improvement from the valid period achieved when the boresight of the sun sensor was aligned with the negative Z_B-axis.

Bibliography

[1] R. Nugent, R. Munakata, A. Chin, R. Coelho, and D. J. Puig-Suari, "The CubeSat: The picosatellite standard for research," in *AIAA(American Institute of Aeronautics and Astronautics) Space 2008 Conference and Exhibition*, 2008.

[2] A. Scholz, W. Ley, B. Dachwald, and J. Juang, "Flight results of the compass-1 picosatellite mission," *Acta Astronautica*, vol. 67, no. 9-10, Nov. 2010.

[3] F. Baumann, K. Briess, and H. Kayal, "Beesat - a fault-tolerant picosatellite approach," in *7th IAA Symposium on Small Satellites for Earth Observation*, May 4–8, 2009, paper AIAA-RS3 2005-3001.

[4] K. Sarda, C. Grant, S. Eagleson, D. D. Kekez, and R. E. Zee, "Canadian advanced nanospace experiment 2: On-orbit experiences with a three-kilogram satellite," in *22nd Annual Small Satellite Conference*, Aug. 11–14, 2008, paper SSC08-II-5.

[5] (2011, Nov.) QuakeSat Lessons Learned: Notes from the Development of a Triple CubeSat. QuakeFinder. [Online]. Available: http://www.quakefinder.com/services/spaceproducts.php

[6] H. J. Kramer. (2011, Nov.) CubeSat - Launch 2 . eoPortal. [Online]. Available: http://events.eoportal.org

[7] M. L. Gargasz, "Optimal Spacecraft Attitude Control Using Aerodynamics Torques," Master's thesis, Air Force Institute of Technology, 2007.

[8] M. L. Psiaki, "Nanosatellite attitude stabilization using passive aerodynamic and active magnetic torquing," *Journal of Guidance, Control and Dynamics*, vol. 27, no. 3, Jun. 2004.

[9] S. Rawashdeh, D. Jones, D. Erb, A. Karam, and J. James E. Lumpp, "Spacecraft attitude control using aerodynamic torques," in *32nd AAS Guidance and Control Conference*, Jan. 2009, paper AAS 09-084.

[10] J. R. Wertz, Ed., *Spacecraft Attitude Determination and Control*, 1st ed. Dordrecht, The Netherlands: Kluwer Academic Publishers, Reprint 1991.

[11] Honeywell. (2011, Sep.) 1, 2 and 3 Axis Magnetic Sensors HMC1053. [Online]. Available: http://www.magneticsensors.com/literature.php

[12] H. E. Loubser, "The development of sun and nadir sensors for a solar sail CubeSat," Master's thesis, Stellenbosch University, 2011.

[13] P. J. Botma, "The Design and Development of an ADCS OBC for a CubeSat," Master's thesis, Stellenbosch University, 2011.

[14] S. Lee, A. Hutputanasin, A. Toorian, W. Lan, and R. Munakata. (2011, Sep.) CubeSat design specification. [Online]. Available: http://www.cubesat.org/images/developers/cds_rev12.pdf

[15] A. Toorian, E. Blundell, D. J. P. Suari, and R. Twiggs, "CubeSats as responsive satellites," in *AIAA (American Institute of Aeronautics and Astronautics) 3rd Responsive Space Conference*, Apr. 25–28, 2005, paper AIAA-RS3 2005-3001.

[16] A. C. DeJesus, "Integration and environmental qualification testing of spacecraft structures in support of the naval postgraduate school CubeSat launcher program," Master's thesis, Naval Postgraduate School, 2009.

[17] J. Giesselmann, "Development of an Active Magnetic Attitude Determination and Control System for Picosatellites on highly inclined circular Low Earth Orbits," Master's thesis, RMIT University, 2006.

[18] H. J. Kramer. (2011, Nov.) BeeSat-1 (Berlin Experimental Educational Satellite-1) . eoPortal. [Online]. Available: http://events.eoportal.org

[19] M. Long, A. Lorenz, G. Rodgers, E. Tapio, G. Tran, K. Jackson, and R. Twiggs, "A CubeSat derived design for a unique academic research mission in earthquake signature detection," in *16th Annual Small Satellite Conference*, Aug. 12–15, 2002, paper SSC02-IX-6.

[20] J. R. Wertz and W. J. Larson, Eds., *Space mission analysis and design*, 3rd ed. El Segundo, CA: Microcosm Press, 1999.

[21] W. H. Steyn and V. Lappas, "CubeSat solar sail 3-axis stabilization using panel translation and magnetic torquing," *Aerospace Science and Technology*, vol. 15, no. 6, Sep. 2011.

[22] B. Wie, H. Weiss, and A. Arapostathis, "Quaternion feedback regulator for spacecraft eigenaxis rotations," *Journal of Guidance, Control and Dynamics*, vol. 12, no. 3, Jun. 1989.

[23] B. D. Tapley, B. E. Schutz, and G. H. Born, *Statistical Orbit Determination*, 1st ed. New York: Elsevier Academic Press, 2004.

[24] R. Lehmensiek, "Using the physical structure of a passive aerodynamic attitude stabilisation system as a multi-frequency antenna on small satellites," Cape Peninsula University of Technology, 2010, internal communication.

[25] M. J. Sidi, *Spacecraft dynamics and Control: A practical engineering approach*, 1st ed. Cambridge: Cambridge University Press, 1997.

[26] W. H. Steyn, "A multi-mode attitude determination and control system for small satellites," Ph.D. dissertation, Stellenbosch University, 1995.

[27] M. L. Gargasz and N. A. Titus, "Spacecraft attitude control using aerodynamic torques," in *17th AAS/AIAA Space Flight Mechanics Meeting*, Feb. 2007, paper AAS 07-178.

[28] P. C. Hughes, *Spacecraft Attitude Dynamics*, 1st ed. New York: Dover Publications, Reprint 2004.

[29] D. A. Vallado, *Fundamentals of Astrodynamics and Applications*. El Segundo, CA: Microcosm Press, 2001.

[30] T. Kelso. (2011, Nov.) NORAD Two-Line Element Sets, Current Data. [Online]. Available: http://celestrak.com/NORAD/elements/

[31] F. R. Hoots and R. L. Roehrich. (2011, Nov.) Spacetrack Report No. 3, Models for Propagation of NORAD Element Sets. [Online]. Available: http://www.celestrak.com/NORAD/documentation/spacetrk.pdf

[32] C. Finlay. (2011, Nov.) International Geomagnetic Reference Field. International Association of Geomagnetism and Aeronomy. [Online]. Available: http://www.ngdc.noaa.gov/IAGA/vmod/igrf.html

[33] P. R. Halmos, *Finite-Dimensional Vector Spaces*, 4th ed. New York: Springer-Verlag, 1987.

[34] C. Hall, "Lecture notes: Attitude determination," 2003. [Online]. Available: http://www.dept.aoe.vt.edu/~cdhall/courses/aoe4140/

[35] W. H. Steyn, "Lecture notes: Ekf estimation," 2004.

[36] P. S. Maybeck, *Stochastic models, estimation and control*, 4th ed. New York: Academic Press, 1979, vol. 1.

[37] W. H. Steyn, "An attitude control system for SumbandilaSat - An Earth Observation Satellite," in *ESA 4S Symposium*, May 26–30, 2008, paper 4 in Session 16.

[38] M. Guelman, I. Flohr, F. Ortenberg, M. Shachar, A. Shiryaev, A. Volfovsky, and R. Waler, "The Israeli microsatellite TechSat for scientific and technological research: Development and in-orbit testing," *Acta Astronautica*, vol. 46, no. 2-6, Jun. 2000.

[39] W. H. Steyn and Y. Hashida, "An attitude control system for a low-cost Earth Observation Satellite with orbit maintenance capability," in *13th Annual Small Satellite Conference*, Aug. 1999, paper SSC99-XI-4.

[40] P. H. Mey, "Development of Attitude Controllers and Actuators for a Solar Sail CubeSat," Master's thesis, Stellenbosch University, 2011.

Appendices

Appendix A

Extended Kalman Filter State Perturbation Matrix

This chapter contains the mathematical derivation of the state perturbation matrix $\mathbf{F}\{\mathbf{x}(t), t\}$ of the extended Kalman filter described in Section 4.3.

A.1 State Perturbation Matrix

The state vector consists of the inertial referenced angular body rate vector and the attitude quaternion vector:

$$\mathbf{x}(t) = \begin{bmatrix} {\boldsymbol{\omega}_B^I}^T(t) & \mathbf{q}^T(t) \end{bmatrix}^T \tag{A.1.1}$$

$$= \begin{bmatrix} \omega_{xi} & \omega_{yi} & \omega_{zi} & q_1 & q_2 & q_3 & q_4 \end{bmatrix}^T \tag{A.1.2}$$

The state perturbation matrix is defined as:

$$\mathbf{F}\{\hat{\mathbf{x}}(t), t\} \triangleq \left.\frac{\partial \mathbf{f}}{\partial \mathbf{x}}\right|_{\mathbf{x}=\hat{\mathbf{x}}} \tag{A.1.3}$$

where

$$\mathbf{f}\{\mathbf{x}(t), t\} \approx \dot{\mathbf{x}}(t) \tag{A.1.4}$$

$$= \begin{bmatrix} {\dot{\boldsymbol{\omega}}_B^I}^T(t) & \dot{\mathbf{q}}^T(t) \end{bmatrix}^T \tag{A.1.5}$$

The Euler dynamic equation is given by:

$$\dot{\boldsymbol{\omega}}_B^I = \mathbf{I}^{-1}\left(\mathbf{N}_M + \mathbf{N}_{Aero} + \mathbf{N}_{GG} - \mathbf{N}_W - \boldsymbol{\omega}_B^I \times (\mathbf{I}\boldsymbol{\omega}_B^I + \mathbf{h}_W)\right) \tag{A.1.6}$$

and can be expanded to

$$\dot{\omega}_{xi} = I_{xx}^{-1}\left(N_x + GG(I_{zz} - I_{yy})A_{33}A_{23} + (I_{yy} - I_{zz})\omega_{yi}\omega_{zi} - \omega_{yi}h_{wz} + \omega_{zi}h_{wy}\right) \quad \text{(A.1.7)}$$

$$\dot{\omega}_{yi} = I_{yy}^{-1}\left(N_y + GG(I_{xx} - I_{zz})A_{33}A_{13} + (I_{zz} - I_{xx})\omega_{xi}\omega_{zi} - \omega_{zi}h_{wx} + \omega_{xi}h_{wz}\right) \quad \text{(A.1.8)}$$

$$\dot{\omega}_{zi} = I_{zz}^{-1}\left(N_z + GG(I_{yy} - I_{xx})A_{13}A_{23} + (I_{xx} - I_{yy})\omega_{xi}\omega_{yi} - \omega_{xi}h_{wy} + \omega_{yi}h_{wx}\right) \quad \text{(A.1.9)}$$

where $GG = 3\mu/\left\|\mathbf{R}\right\|^3$ is the constant of the gravity gradient torque which includes the gravitational constant of the Earth $\mu = 398600.5\,\mathrm{km}^3/\mathrm{s}^2$ and the magnitude of the orbital radius $\left\|\mathbf{R}\right\|$. The torque elements N_x, N_y and N_z represents all control and disturbance torques except the gravity gradient torque which is expressed in terms of the components of transformation matrix $\mathbf{A}_{O/B}\left\{q(t)\right\}$.

From the kinematic equation we find:

$$\dot{\mathbf{q}} = 0.5\begin{bmatrix} q_4 & -q_3 & q_2 \\ q_3 & q_4 & -q_1 \\ -q_2 & q_1 & q_4 \\ -q_1 & -q_2 & -q_3 \end{bmatrix}\boldsymbol{\omega}_B^O$$

$$\begin{bmatrix} \dot{q}_1 \\ \dot{q}_2 \\ \dot{q}_3 \\ \dot{q}_4 \end{bmatrix} = 0.5\begin{bmatrix} q_4 & -q_3 & q_2 \\ q_3 & q_4 & -q_1 \\ -q_2 & q_1 & q_4 \\ -q_1 & -q_2 & -q_3 \end{bmatrix}\begin{bmatrix} \omega_{xi} + A_{12}\omega_o \\ \omega_{yi} + A_{22}\omega_o \\ \omega_{zi} + A_{32}\omega_o \end{bmatrix} \quad \text{(A.1.10)}$$

by substituting $\boldsymbol{\omega}_B^O = \boldsymbol{\omega}_B^I + \mathbf{A}_{O/B}\begin{bmatrix} 0 & \omega_o & 0 \end{bmatrix}^T$.

The state perturbation matrix can now be derived as the partial derivative of the state matrix with respect to the state vector:

$$\begin{aligned} \mathbf{F}\left\{\hat{\mathbf{x}}(t), t\right\} &= \left.\frac{\partial \mathbf{f}}{\partial \mathbf{x}}\right|_{\mathbf{x}=\hat{\mathbf{x}}} \\ &= \begin{bmatrix} \mathbf{F}_{11} & \mathbf{F}_{12} \\ \mathbf{F}_{21} & \mathbf{F}_{22} \end{bmatrix} \end{aligned} \quad \text{(A.1.11)}$$

with

$$\begin{aligned} \mathbf{F}_{11} &= \left.\frac{\partial \dot{\boldsymbol{\omega}}_B^I}{\partial \boldsymbol{\omega}_B^I}\right|_{\mathbf{x}=\hat{\mathbf{x}}} \\ &= \begin{bmatrix} 0 & \frac{\left((I_{yy}-I_{zz})\hat{\omega}_{zi}-h_{wz}\right)}{I_{xx}} & \frac{\left((I_{yy}-I_{zz})\hat{\omega}_{yi}+h_{wy}\right)}{I_{xx}} \\ \frac{\left((I_{zz}-I_{xx})\hat{\omega}_{zi}+h_{wz}\right)}{I_{yy}} & 0 & \frac{\left((I_{zz}-I_{xx})\hat{\omega}_{xi}-h_{wx}\right)}{I_{yy}} \\ \frac{\left((I_{xx}-I_{yy})\hat{\omega}_{yi}-h_{wy}\right)}{I_{zz}} & \frac{\left((I_{xx}-I_{yy})\hat{\omega}_{xi}+h_{wx}\right)}{I_{zz}} & 0 \end{bmatrix} \end{aligned} \quad \text{(A.1.12)}$$

and

$$\mathbf{F}_{21} = \left.\frac{\partial \dot{\mathbf{q}}}{\partial \boldsymbol{\omega}_B^I}\right|_{\mathbf{x}=\hat{\mathbf{x}}} = 0.5 \begin{bmatrix} \hat{q}_4 & -\hat{q}_3 & \hat{q}_2 \\ \hat{q}_3 & \hat{q}_4 & -\hat{q}_1 \\ -\hat{q}_2 & \hat{q}_1 & \hat{q}_4 \\ -\hat{q}_1 & -\hat{q}_2 & -\hat{q}_3 \end{bmatrix} \tag{A.1.13}$$

and

$$\mathbf{F}_{12} = \left.\frac{\partial \dot{\boldsymbol{\omega}}_B^I}{\partial \mathbf{q}}\right|_{\mathbf{x}=\hat{\mathbf{x}}} = \begin{bmatrix} \mathbf{F}_{12(A)} & \mathbf{F}_{12(B)} \end{bmatrix} \tag{A.1.14}$$

with

$$\mathbf{F}_{12(A)} = 2GG \begin{bmatrix} \frac{(I_{yy}-I_{zz})}{I_{xx}}(\hat{q}_1 A_{23} - \hat{q}_4 A_{33}) & \frac{(I_{yy}-I_{zz})}{I_{xx}}(\hat{q}_2 A_{23} - \hat{q}_3 A_{33}) \\ \frac{(I_{zz}-I_{xx})}{I_{yy}}(\hat{q}_1 A_{13} - \hat{q}_3 A_{33}) & \frac{(I_{zz}-I_{xx})}{I_{yy}}(\hat{q}_2 A_{13} + \hat{q}_4 A_{33}) \\ \frac{(I_{yy}-I_{xx})}{I_{zz}}(\hat{q}_3 A_{23} + \hat{q}_4 A_{13}) & \frac{(I_{yy}-I_{xx})}{I_{zz}}(\hat{q}_3 A_{13} - \hat{q}_4 A_{23}) \end{bmatrix} \tag{A.1.15}$$

$$\mathbf{F}_{12(B)} = 2GG \begin{bmatrix} \frac{(I_{zz}-I_{yy})}{I_{xx}}(\hat{q}_3 A_{23} + \hat{q}_2 A_{33}) & \frac{(I_{zz}-I_{yy})}{I_{xx}}(\hat{q}_4 A_{23} + \hat{q}_1 A_{33}) \\ \frac{(I_{xx}-I_{zz})}{I_{yy}}(\hat{q}_3 A_{13} + \hat{q}_1 A_{33}) & \frac{(I_{xx}-I_{zz})}{I_{yy}}(\hat{q}_4 A_{13} - \hat{q}_2 A_{33}) \\ \frac{(I_{yy}-I_{xx})}{I_{zz}}(\hat{q}_1 A_{23} + \hat{q}_2 A_{13}) & \frac{(I_{yy}-I_{xx})}{I_{zz}}(\hat{q}_1 A_{13} - \hat{q}_2 A_{23}) \end{bmatrix} \tag{A.1.16}$$

and

$$\mathbf{F}_{22} = \left.\frac{\partial \dot{\mathbf{q}}}{\partial \mathbf{q}}\right|_{\mathbf{x}=\hat{\mathbf{x}}} = 0.5 \begin{bmatrix} 0 & \hat{\omega}_{zo} & -\hat{\omega}_{yo} & \hat{\omega}_{xo} \\ -\hat{\omega}_{zo} & 0 & \hat{\omega}_{xo} & \hat{\omega}_{yo} \\ \hat{\omega}_{yo} & -\hat{\omega}_{xo} & 0 & \hat{\omega}_{zo} \\ -\hat{\omega}_{xo} & -\hat{\omega}_{yo} & -\hat{\omega}_{zo} & 0 \end{bmatrix} + \omega_o \begin{bmatrix} \hat{q}_1\hat{q}_3 & \hat{q}_1\hat{q}_4 & (1-\hat{q}_1^2) & -\hat{q}_1\hat{q}_2 \\ \hat{q}_2\hat{q}_3 & \hat{q}_2\hat{q}_4 & -\hat{q}_1\hat{q}_2 & (1-\hat{q}_2^2) \\ (\hat{q}_3^2-1) & \hat{q}_3\hat{q}_4 & -\hat{q}_1\hat{q}_3 & -\hat{q}_2\hat{q}_3 \\ \hat{q}_3\hat{q}_4 & (\hat{q}_4^2-1) & -\hat{q}_1\hat{q}_4 & -\hat{q}_2\hat{q}_4 \end{bmatrix} \tag{A.1.17}$$

This concludes the computation of the state perturbation matrix.